



Design and analysis of a hybrid composite  
material blade for a hydrokinetic turbine

Thesis

Submitted to the Faculty of Fachhochschule Aachen and Centro de Ingenieria  
y Desarrollo Industrial

BY

M.E. Gilberto de Jesús León-Muñoz

PRIMARY ADVISOR:

Dr. Eng. Carlos Rubio González

In Partial Fulfillment of the requirements for the degree of  
Master of Science in Mechatronics

Santiago de Querétaro, Qro., México, September 2018









---

# Declaration of Authorship

Hereby, I, Gilberto de Jesús León-Muñoz, declare that this thesis "Design and analysis of a hybrid composite material blade for hydrokinetic turbine" is the result of my own work. Any part of this dissertation has not been previously submitted, in part or whole, to any university or institution for a degree or other qualification.

I confirm that all consulted work from others is attributed and the source is always given. Furthermore, the data and the software employed have all been utilized in complete agreement to the copyright rules of concerned establishments.

Signed: \_\_\_\_\_

Santiago de Querétaro, México, September 2018



---

# Acknowledgments

All the experiences I lived in Mexico as well as in Germany wouldn't have been possible without the support of CONACyT. There is no way I can thank enough to this entity.

Really special thanks to Dr. Carlos Rubio González for being my advisor and letting me work on this project in the first place, helped me when necessary and also provided me with the essential tools for completing this project. Also I would like to thank Jaime Espinoza for all the advises he gave me.

For all the support given during our studies in FH Aachen, all the doubts and troubles he helped us with, I am really thankful to Prof. Dr. Kämper.

Prof. Dr. Wollert for his assistance on doubts and be there for all of us during our stay in FH Aachen.

To Dr. Salvador Acuña for the guidance and interest for us during this program.

I really want to thank all my friends, the ones I coursed the master with and also those who are far away and gave their support. Each of them changed my mind for good.

Last but not least, my family: my mother, my father and my brothers. They were with me all the time despite the distance and they all let me do this at my own timing and way.



---

# Abstract

In this work, a hybrid composite material is implemented on a hydrokinetic turbine blade and the blade's structural behavior is analyzed. The Energy Department of Centro de Ingeniería y Desarrollo Industrial (CIDESI) worked on the characterization of an hybrid material composed carbon and glass fiber plies for its application on spar caps of wind turbine blades.

Composite lay-up in the hydrokinetic turbine blade of both glass fiber and hybrid material is presented as well as their respective named selections. Then, a static structural simulation is made emulating operational conditions of the blade's worst case scenario. Subsequently, eigenvalue buckling analysis is carried out as a verification whether buckling is presented and, if so, verify if the blade is being threaten. Afterwards, a modal analysis is implemented in order to look for coincidence between the first modes and blade's working conditions.

The implementation of the hybrid material showed a great improvement in the structural behavior of the hydrokinetic blade compared with previous versions made of glass fibers as well as a mass reduction of around 22.82 %. After implementing a material optimization method, mass was able to be lowered further by 25.27 %, and also failure criterion indexes were reduced.



---

# Kurzfassung

Die vorliegende Arbeit zeigt die Implementierung eines Hybridkomposits in eine hydrokinetische Turbinenschaufel sowie die Analyse des Strukturverhaltens dieser Schaufel. Die Energieabteilung des Center for Engineering and Industrial Development (CIDESI) arbeitet an der Charakterisierung eines Hybridmaterials bestehend aus Karbon- und Glasfaser-schichten für Gehäuse von Windkraftanlagen.

Zunächst werden die Kohlenfaserverbundstoffe der hydrokinetischen Schaufel in Bezug auf Glasfasern und dem hybriden Material präsentiert sowie jeweils deren Auswahl dargestellt. Anschließend erfolgt eine statische Simulation, welche auf einem Worst-Case Szenario in den auftretenden Betriebszuständen der Turbinenschaufel basiert. Im Rahmen einer Eigenwert-Knickanalyse wird ermittelt, ob es zu einem Knicken der Schaufeln kommt, welches zu Schäden führen kann. Abschließend wird durch eine Modalanalyse überprüft, ob ein Zusammenhang zwischen den ersten Schwingungsmoden und den Arbeitsbedingungen der Turbinenschaufel besteht.

Insgesamt zeigt die Implementierung des hybriden Materials eine starke Verbesserung des Strukturverhaltens der hydrokinetischen Schaufel im Vergleich zu vorhergehenden Versionen aus Glasfasern. Zudem entsteht eine Gewichtsreduktion von ca. 22,82 %. Durch die Durchführung einer Materialoptimierungsmethode kann das Gewicht insgesamt um 25,27 % reduziert werden. Des Weiteren können die Werte der Ausfallkriterien reduziert werden.





---

# Resumen

En este trabajo, un material compuesto híbrido es implementado en un aspa de turbina hidrocínética y su comportamiento estructural es analizado. El departamento de Energía del Centro de Ingeniería y Desarrollo Industrial (CIDESI) trabajó en la caracterización de un material híbrido compuesto por capas de fibras de carbono y fibras de vidrio para su aplicación en spar caps de turbinas eólicas.

Se presenta la composición de fibras de vidrio y material híbrido en el aspa para turbina hidrocínética así como sus respectivas selecciones nombradas. Después, se realiza una simulación estructural estática emulando las condiciones de trabajo del aspa en el peor de los casos. Subsecuentemente, se lleva a cabo un análisis de pandeo usando valores propios para verificar si este fenómeno se presenta y, de ser así, determinar si el aspa se ve amenazada. Posteriormente, se implementa un análisis modal para revisar si existe coincidencia entre los primeros modos y las condiciones de trabajo del aspa.

La implementación del material compuesto híbrido comparada con versiones anteriores, diseñadas completamente de fibras de vidrio, mostró una gran mejora en el comportamiento estructural del aspa así como una reducción de su masa alrededor de 22.82 %. Después de ejecutar un método para la optimización de material, fue posible reducir la masa hasta un 25.27 % y los índices de fallo también se vieron reducidos.



# Contents

Declaration of authorship . . . . .	i
Acknowledgments . . . . .	iii
Abstract . . . . .	v
Kurzfassung . . . . .	vii
Resumen . . . . .	ix
List of figures . . . . .	xvii
List of tables . . . . .	xx
Acronyms . . . . .	xxi
<b>1 Introduction</b>	<b>1</b>
1.1 Statement of the problem . . . . .	3
1.2 Justification . . . . .	6
1.3 Objectives . . . . .	7
1.3.1 General objective . . . . .	7
1.3.2 Specific objectives . . . . .	7
1.4 Hypothesis . . . . .	7
1.5 Methodology . . . . .	8
<b>2 State of the art</b>	<b>11</b>
2.1 Hybrid composite material . . . . .	11
2.2 Aero- and hydrodynamic blade research . . . . .	12
2.2.1 Aerodynamics of wind turbines . . . . .	13
2.2.2 Sandwich Materials for Wind Turbine Blades . . . . .	13
2.2.3 Design of composite tidal turbine blades . . . . .	15
2.2.4 Structural optimization study of composite wind turbine blade . . . . .	17
2.2.5 Structural investigation of composite wind turbine blade considering structural collapse in full-scale static tests . . . . .	17

<b>3</b>	<b>Theoretical background</b>	<b>19</b>
3.1	Composite materials . . . . .	19
3.1.1	Lamina stress-strain relationships . . . . .	19
3.1.2	Strength of a continuous fiber-reinforced lamina . . . . .	22
3.1.3	Maximum Stress Criterion . . . . .	24
3.1.4	Maximum Strain Criterion . . . . .	25
3.1.5	Quadratic Interaction Criteria (Tsai-Hill Criterion) . . . . .	25
3.1.6	Laminates . . . . .	26
3.1.7	Theory of laminated beams . . . . .	27
3.1.7.1	Flexural Stresses and Deflections . . . . .	27
3.1.8	Selection of laminate designs . . . . .	29
3.2	Loads and structural components of wind and hydrokinetic turbine blades	31
3.2.1	Aerodynamic loads . . . . .	31
3.2.2	Gravitational and centrifugal loads . . . . .	32
3.2.3	Flapwise bending . . . . .	32
3.2.4	Edgewise bending . . . . .	33
3.3	ANSYS Composite PrepPost (ACP) . . . . .	34
3.3.1	ANSYS Workbench and ACP . . . . .	34
3.3.2	Failure criterion nomenclature . . . . .	35
<b>4</b>	<b>Simulation process</b>	<b>37</b>
4.1	Definition of hybrid material in ANSYS . . . . .	37
4.2	Model configuration description . . . . .	38
4.2.1	Meshing . . . . .	39
4.2.2	Named selections . . . . .	40
4.2.3	Model lay-up in ACP . . . . .	41
4.2.4	Boundary conditions . . . . .	42
4.2.5	Static structural analysis . . . . .	43
4.2.6	Eigenvalue buckling analysis . . . . .	43
4.2.7	Modal analysis . . . . .	44
4.2.8	Fabrication validation . . . . .	44
4.2.9	Optimization process . . . . .	44
<b>5</b>	<b>Results and discussions</b>	<b>45</b>
5.1	Blade model “version 2.0” . . . . .	45
5.1.1	Blade’s composite lay-up and Static Structural simulation . . . . .	45
5.1.1.1	Hydrofoil . . . . .	45

5.1.1.2	Spar caps . . . . .	48
5.1.1.3	Shear Web . . . . .	50
5.2	Blade “version 2.1” . . . . .	52
5.2.1	Meshing . . . . .	52
5.2.2	Named selections . . . . .	53
5.2.3	Static Structural results and conclusions . . . . .	54
5.3	Blade model “version 3.0” . . . . .	55
5.3.1	Blade’s lay-up and named selections . . . . .	55
5.3.1.1	Spar caps . . . . .	55
5.3.1.2	Root reinforcements . . . . .	57
5.3.1.3	Shear web . . . . .	58
5.3.1.4	Blade’s “version 3.0” lay-up . . . . .	58
5.3.2	Static Structural simulation results . . . . .	59
5.3.3	Eigenvalue buckling analysis . . . . .	61
5.3.4	Modal analysis simulation . . . . .	62
5.3.5	Mass optimization . . . . .	63
5.3.5.1	Design of experiments . . . . .	63
5.3.5.2	Response surface regression: Displacement versus length, width . . . . .	64
5.3.5.3	Response surface regression: Mass versus length, width . . . . .	65
5.3.5.4	Response surface regression: Failure versus length, width . . . . .	66
5.3.5.5	Response optimizer . . . . .	67
5.4	Blade model “version 3.1” . . . . .	68
5.4.1	Static Structural simulation . . . . .	68
5.4.2	Eigenvalue buckling simulation . . . . .	71
5.4.3	Modal analysis simulation . . . . .	72
5.5	Comparison of blade models . . . . .	73
<b>6</b>	<b>Conclusions and further work</b>	<b>75</b>
	Bibliography . . . . .	78
	<b>Appendices</b>	<b>79</b>
<b>A</b>	<b>Hybrid material properties</b>	<b>81</b>
<b>B</b>	<b>Chronogram of activities</b>	<b>83</b>
<b>C</b>	<b>Computational fluid dynamics forces</b>	<b>85</b>



# List of Figures

1.1	Horizontal axis hydrokinetic turbine . . . . .	2
1.2	Preliminary blade design “version 0” . . . . .	4
1.3	Blade geometry design “vesion 1.0” . . . . .	5
1.4	Thickness distribution of “version 1.0” of the blade . . . . .	5
1.5	Thesis methodolody diagram . . . . .	9
1.6	Flowchart of simulation process methodology . . . . .	10
2.1	Cross-section scheme of the hybrid material laminate . . . . .	11
2.2	Diagram of power generation by wind/hydrokinetic turbine . . . . .	12
2.3	Lift and drag force forces in an aerodynamic profile . . . . .	13
2.4	Traditional spar caps and shear webs configuration in aerofoils . . . . .	14
2.5	Blade design concepts . . . . .	14
2.6	Flowchart of structural modelling process . . . . .	16
3.1	Types of fiber-reinforced composites . . . . .	20
3.2	Orthotropic lamina coordenate systems . . . . .	20
3.3	States of stress for engineering constanst . . . . .	21
3.4	Stress-strain curves in lamina in-plane strengths and ultimate strains . . . . .	23
3.5	Fiber discontinuties in the matrix . . . . .	24
3.6	Maximum Stress Criterion in $\sigma_1, \sigma_2$ space . . . . .	24
3.7	Examples of laminate stacking sequences . . . . .	27
3.8	Laminated beam deflection . . . . .	28
3.9	Cantilever beam under concentrated tip load . . . . .	29
3.10	Stress distribution comparison between isotropic and laminated beam . . . . .	29
3.11	Flow chart for laminate analysis . . . . .	30
3.12	Forces interacting with an aero- or hydrofoil . . . . .	31
3.13	Blade modeled as a cantilever beam with uniformly distributed aerodynamic load . . . . .	32

3.14	Spar cap region in blade cross section . . . . .	32
3.15	Gravitational load modeled as a cantilever beam . . . . .	33
3.16	Edgewise bending around $yy$ . . . . .	34
3.17	Block diagrams example of ANSYS ACP on Workbench . . . . .	35
3.18	Failure criterion and color code example on ACP Post . . . . .	35
4.1	Shell blade model divided in 28 sections along its lenght . . . . .	39
4.2	Edge meshing applied on the blade's leading edge . . . . .	39
4.3	Blade model meshing . . . . .	40
4.4	Spar cap's named selection example . . . . .	40
4.5	ACP Pre tools . . . . .	41
4.6	Model's lay-up configuration example in ACP . . . . .	42
4.7	Blade's model boundary conditions . . . . .	42
4.8	Eigenvalue block configuration in ANSYS Workbench . . . . .	44
5.1	Hydrofoil named selection for blade "version 2.0" . . . . .	46
5.2	Total tip displacement result using only hydrofoil for blade "version 2.0" . . . . .	46
5.3	Stresses and strains on the 2 direction results using only hydrofoil for blade "version 2.0" . . . . .	47
5.4	Failure criterion results for hydrofoil blade "version 2.0" . . . . .	48
5.5	Spar caps along the whole length of the blade with a width of 20 mm in both pressure and suction sides . . . . .	49
5.6	Failure criterion results for blade "version 2.0" using spar caps . . . . .	49
5.7	Shear web named selection . . . . .	50
5.8	Failure criterion simulation results for blade "version 2.0" . . . . .	51
5.9	Failure on the 2 direction of the fiber located in the shear web . . . . .	52
5.10	Refined blade's meshing . . . . .	52
5.11	Spar caps reinforcement for blade "version 2.0" . . . . .	53
5.12	Root named selection reinforcement zone . . . . .	54
5.13	Shear web lay-up sketch . . . . .	54
5.14	Blade lay-up "version 2.1" . . . . .	55
5.15	Hybrid material spar caps along the blade's length and 30 mm and 20 mm width reduction at the tip . . . . .	56
5.16	Hybrid material reinforcements in pressure and suction side of the blade . . . . .	56
5.17	Glass fiber side root reinforcement named selections . . . . .	57
5.18	Additional hybrid material root support on each side of the blade with 72 mm length . . . . .	58



---

5.19	Shear web's named selection for blade "version 3.0" . . . . .	58
5.20	Blade "version 3.0" composite lay-up setup . . . . .	59
5.21	Displacement results of blade "version 3.0" . . . . .	60
5.22	Stress distribution results in the 2 direction in both sides of the blade "version 3.0" . . . . .	60
5.23	Strain distribution results in the 2 direction in both sides of the blade "version 3.0" . . . . .	61
5.24	Maximum Strain Criteria value distribution on pressure side of the blade .	61
5.25	Eigenvalue buckling analysis results for mode 3 . . . . .	62
5.26	First mode of blade "version 3.0" with a frequency of 53.384 Hz . . . . .	63
5.27	Spar cap of 185.55 mm length and 40 mm width . . . . .	64
5.28	Minitab's contour plot of displacement versus length, width . . . . .	65
5.29	Minitab's contour plot of mass versus length, width . . . . .	66
5.30	Minitab's contour plot of failure versus length, width . . . . .	67
5.31	Spar cap with 432 mm length and 40 mm width for blade "version 3.1" . .	68
5.32	Displacement simulation results for blade "version 3.1" . . . . .	69
5.33	Stress distribution results in the 2 direction in both sides of the blade "version 3.1" . . . . .	70
5.34	Strain distribution results in the 2 direction in both sides of the blade "version 3.1" . . . . .	70
5.35	Maximum Strain Criteria value distribution on pressure side of the blade .	71
5.36	Eigenvalue buckling analysis results for mode 3 of blade "version 3.1" . . .	72
5.37	First mode of blade "version 3.1" with a frequency of 53.384 Hz . . . . .	73
5.38	Blade "version 3.1" composite lay-up setup . . . . .	74
B.1	Chronogram of activities . . . . .	84



# List of Tables

- 1.1 Sources of renewable energy . . . . . 1
- 1.2 Composite lay-up for blade “version 1.0” . . . . . 5
- 1.3 Results blade “version 1.0” . . . . . 6
  
- 2.1 Mechanical properties of hybrid composite laminates at 0° . . . . . 12
- 2.2 Mechanical properties of hybrid composite laminates at 90° . . . . . 12
  
- 3.1 Design criteria for composite laminates and associated failure modes . . . . . 30
- 3.2 Failure criterion terms . . . . . 36
  
- 4.1 Blade model dimensions . . . . . 38
  
- 5.1 Results of the Static Structural simulation using only hydrofoil . . . . . 46
- 5.2 Results of the Static Structural simulation using Spar Caps . . . . . 50
- 5.3 Results of the Static Structural simulation using Shear Web . . . . . 51
- 5.4 Static Structural simulation results for blade “version 2.1” . . . . . 55
- 5.5 Static Structural simulation results for blade “version 3.0” . . . . . 59
- 5.6 Eigenvalue buckling simulation results for blade “version 3.0” . . . . . 62
- 5.7 Modal simulation results for blade “version 3.0” . . . . . 63
- 5.8 Experiment with dimensions of spar caps . . . . . 64
- 5.9 Simulation results input for the design of experiments . . . . . 64
- 5.10 Response optimizer inputs . . . . . 67
- 5.11 Optimizer results with 95 % accuracy expected . . . . . 68
- 5.12 Static Structural simulation results for blade “version 3.1” . . . . . 69
- 5.13 Comparison between response optimizer and Static Structural simulation  
results . . . . . 71
- 5.14 Eigenvalue buckling simulation results for blade “version 3.1” . . . . . 72
- 5.15 Modal simulation results for blade “version 3.1” . . . . . 72
- 5.16 Structural behavior comparison between different blade versions, part 1 of 2 74

5.17	Structural behavior comparison between different blade versions, part 2 of 2	74
A.1	Hybrid composite material density and orthotropic elasticity properties . .	81
A.2	Hybrid composite material orthotropic stress limits properties . . . . .	82
A.3	Hybrid composite material orthotropic strain limits properties . . . . .	82
C.1	Forces interacting with the hydrokinetic turbine blade . . . . .	86

---

# Acronyms

<b>ACP</b>	ANSYS Composite PrepPost
<b>BEM</b>	Blade Element Momentum
<b>CEMIE-Oceano</b>	Centro Mexicano de Innovacion en Energia-Oceano
<b>CF</b>	Carbon Fiber
<b>CFD</b>	Computational Fluid Dynamics
<b>CFRP</b>	Carbon Fiber Reinforced Polymer
<b>CIDESI</b>	Centro de Ingenieria y desarrollo industrial
<b>DOE</b>	Design of Experiments
<b>FEA</b>	Finite Element Analysis
<b>GF</b>	Glass Fiber
<b>GFRP</b>	Glass Fiber Reinforced Polymer
<b>PVC</b>	Polyvinyl Chloride
<b>UD</b>	Unidirectional
<b>WECs</b>	Wave Energy Converters



# Chapter 1

## Introduction

Earth's energy fossil resources are limited, the difficulty to extract them from soils or oceans becomes harder every year, and thus, their prices will continue to rise more and more often. Moreover, it is widely accepted that the use of fossil energy is the main cause of global warming. Many countries have already taken actions against all these problems by the use of renewable energies [1].

The major source of renewable energy is the sun and derivations of it, and due to the interaction with the earth and moon, they transform into wind and tidal energy. As Table 1.1 depicts, water, wind and solar energy outstand because of their contributions to the current energy demand [2].

Table 1.1: Sources of renewable energy. Taken from [2]

Primary source	Medium	Natural conversion	Technical conversion
Sun	Water	Evaporation, precipitation, melting	Water pump plants
	Wind	Atmospheric windflow	Wind energy conversion
		Wave movement	Wave power plant
	Solar energy	Ocean current	Ocean power plant
		Heating earth surface and atmosphere	Thermal power units, heat pumps
	Solar radiation	Heliothermal conversion, Photovoltaic conversion	
	Biomass	Biomass production	Co-generation plants
Earth	Isotop decay	Geothermal heat	Co-generation plants
Moon	Gravitation	Tides	Tide power plants

The use of water power dates back thousands of years to the water wheels of Ancient Greece, which used the energy in falling water to generate power to grind wheat. Using

this same principle, hydrokinetic technologies produce renewable electricity by harnessing the kinetic energy of a body water mass, the energy results in form of motion. Since water is around 832 times denser than air, tides, waves, ocean currents, and free-flowing rivers represent an untapped, powerful, concentrated and clean energy resource [3].

Technologies developed to generate energy from waves and currents, called hydrokinetic energy devices, are categorized as either Wave Energy Converters (WECs) or rotating devices.

Rotating devices capture the kinetic energy of a flow of water, such as tidal stream, ocean current or a river, as it passes across a rotor. The rotor turns with the current, creating rotatory energy that is converted into electricity by a generator. Rotational devices used in water currents are conceptually akin to, and some designs look very similar to, the wind turbines. This similarity helped to speed up the technological development of water-based turbines.

Some rotational devices designs, like most wind turbines, rotate around the horizontal axis (Figure 1.1), while other, more theoretical concepts are oriented around a vertical axis, with some designs resembling egg beaters.

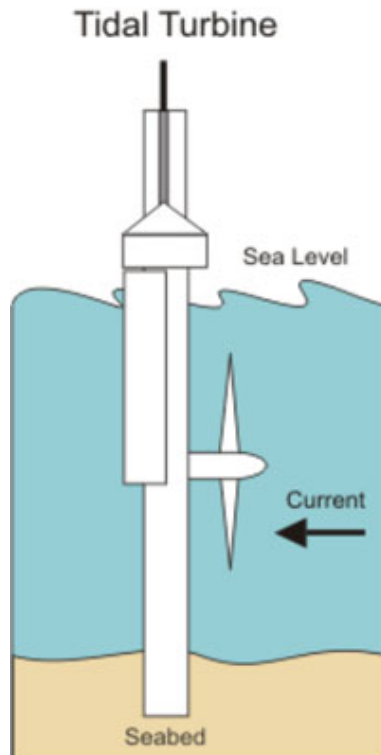


Figure 1.1: Horizontal axis hydrokinetic turbine. Taken from [3]



## 1.1 Statement of the problem

Mexico has a vast marine region where oceanographic conditions are appropriated for the existence of intense marine currents as well as an important range of variate marine currents that could be harnessed as alternate renewable source of energy [4].

Centro Mexicano de Innovacion en Energia-Oceano (CEMIE-Oceano) (Mexican Innovation Center of Energy-Ocean) is an investigation center working on generating products, techniques and technologies for harnessing the variety of available ocean energy resources due to the increasing energy demand in the Mexican Republic.

Currently, two main sites have been identified for implementing this sort of projects: Caribbean Sea and the Gulf of California. However, the project development is not limited to such sites.

As part of their developments, there is an agreement between the Energy Department of Centro de Ingenieria y desarrollo industrial (CIDESI) and CEMIE-Oceano. The project “Diseño de un prototipo de hélice de hasta 70 cm de longitud de material compuesto” (Design of a composite material prototype blade up to 70-cm-length) is derived from the investigation line “Desarrollo de materiales compuestos para aplicaciones marinas en dispositivos de conversión de energía hidrocínética” (Development of composite materials for marine applications in hydrokinetic energy conversion devices) proposed by CEMIE-Oceano [5].

As its name specifies, the project asks for the design of an hydrokinetic turbine blade of 70 cm length maximum. The working conditions establish a nominal current velocity of 1.5 m/s with gust up to of 4 m/s.

Ledesma, S. [5] explains the methodology followed for developing the hydrodynamic blade profile as well as the material selection, ply orientations and preliminary structural design carried out in ANSYS. The preliminary blade design can be seen in Figure 1.2 and the setup can be summarized as follows:

- The hydrodynamic profiles EPPLER e-817 and e-818 were selected as the best option because they work in a relative low Reynold’s number (between 200,000 and 500,000). Furthermore, these profiles can guarantee that there will no be cavitation problems at the tip of the blade.

- The use of spar caps and shear webs is not needed due to the geometry of the preliminary blade geometry.
- Glass fiber was chosen using a sequence of  $[0/45/-45]$  for the hydrofoil.

For a nominal current velocity of 1.5 m/s, the tip deflection is around 1 % of the total length of the blade. Also, by using Tsai-Wu failure theory, a maximum of 28 % of the fiber capacity is used. Moreover, a modal analysis shows that the lowest natural frequency is 86 Hz, beyond from working conditions.

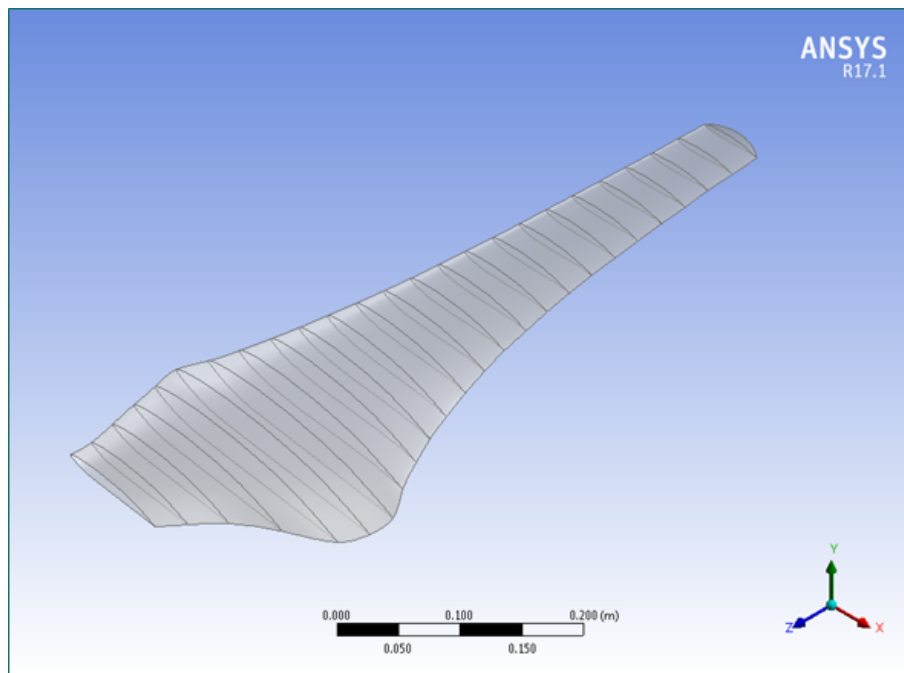


Figure 1.2: Preliminary blade design “version 0”. Taken from [5]

Nonetheless, due to possible manufacturing process complications and in search for improvements in the hydrodynamics, the blade geometry was changed to the one shown in Figure 1.3.

From now on, evaluations under worst case conditions are considered, i.e., under a current gust of 4 m/s.

The major difference between the prior version, “version 0”, and latest one, “version 1.0”, is the implementation of spar caps and a shear web along the whole blade. This, in order for the blade to withstand the higher hydrodynamic load forces caused by the worst case scenario.

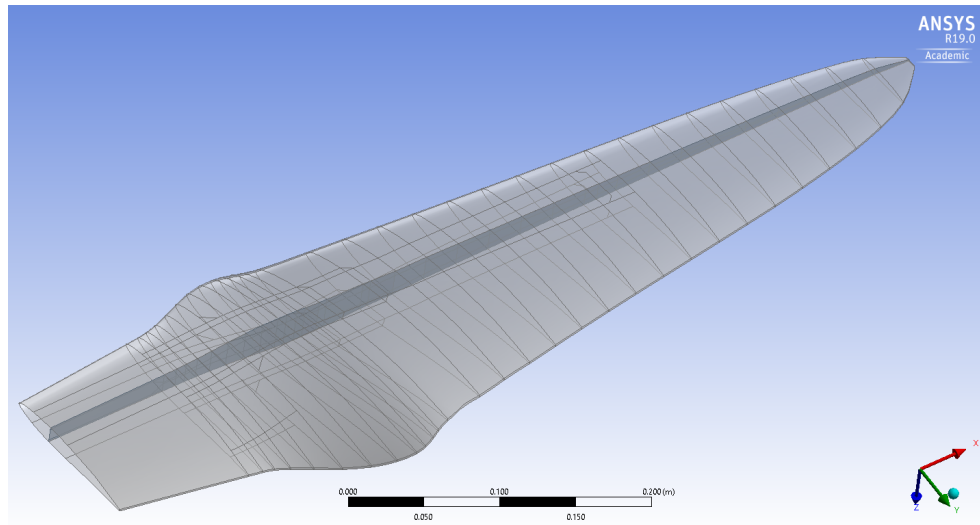


Figure 1.3: Blade geometry design “version 1.0”. Taken from [6]

Espinoza, J. [6] worked on blade’s “version 1.0” and employed the lay-up shown in Table 1.2. The chosen material was Glass Fiber (GF) because it facilitates the manufacture and it is cheaper compared to Carbon Fiber (CF). In the end, the blade thickness distribution resulted by the lay-up is shown in Figure 1.4.

Table 1.2: Composite lay-up for blade “vesion 1.0”. Adapted from [6]

Material	Lay-up	Component
TRIAx	[0/45/-45]	Hydrofoil
Unidirectional (UD)	[0]	Spar caps
TRAX/PVC foam/TRIAx		Shear web

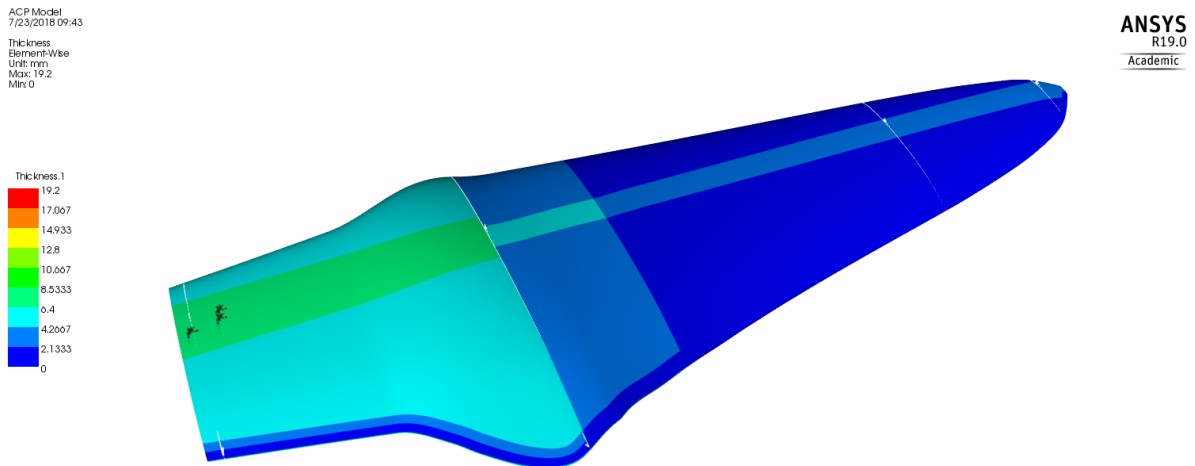


Figure 1.4: Thickness distribution in the blade “version 1.0”. Taken from [6]

Static structural simulation results of this configuration are summarized in Table 1.3. It is important to mention that for Maximum Strain Criterion, a failure index value higher or equal to 1 means failure in the composite material, and as it can be seen, a value of 0.974 is too close to failure. However, it is not possible to add more material in order to lower this value because there is no more space due to the shape of the blade.

Table 1.3: Results blade “version 1.0”. Adapted from [6]

Property	Value	Units
Total tip displacement	21.469	mm
Max strain	0.0036073	mm/mm
Max stress	44.55	MPa
Max Strain Failure Criterion	0.974	
Mass	1.45	kg

## 1.2 Justification

Ideally, the blade lay-up configuration used in [6] works well. However, it is too risky to be fabricated and to be tested in real world conditions. Then, a change of materials have to be made if the blade geometry is not to be changed.

While this problem might be easily solved by changing the blade materials from glass to carbon fiber because of its greater mechanical properties, some complications show up by using this material, rejecting carbon fibers as main material from this application.

First of all, carbon fiber is more expensive than glass fiber in most of the cases. Taking into consideration that each tidal turbine will have three blades, in large scale production, at some point using the same budget, at least, the double of turbines could be fabricated if the blade were made of glass fibers than carbon fibers. If low cost renewable energy is to be produced, this could become an obstacle.

Moreover, fabrication process using carbon fiber also complicates [7]. To mention some examples, carbon has a relatively low damage tolerance and also, it requires a perfect fiber alignment and must be cured quickly [8]. This delicate process makes turbine blades more expensive compared with glass fiber.

On the other hand, the Energy Department of CIDESI worked on a hybrid composite material, comprised of a combination of carbon fibers and glass fibers layers [9]. Definition and details of this material will be addressed later on this thesis.

As a result of the economical problems arising with the use of carbon fiber, it is worth to evaluate the behavior of the blade structural properties using the hybrid material in the spar caps because by combining both materials, higher mechanical properties are achieved thanks to the carbon fiber with just a reasonable price increasing.

## 1.3 Objectives

### 1.3.1 General objective

Implement the hybrid composite material in the spar caps and determine its feasibility in improving the structural behavior of a hydrokinetic turbine blade.

### 1.3.2 Specific objectives

- Define the hybrid composite material in the software ANSYS.
- Implement the hybrid composite material in the spar caps of the hydrokinetic turbine blade model.
- Reduce the mass of the blade using the hybrid composite material compared with the glass fiber blade model “version 1.0”.
- Lower the maximum composite failure indexes below a value of 0.9.
- Obtain a minimum safety factor of 2 for eigenvalue buckling analysis.
- Achieve a minimum margin of 10 between working conditions and the blade natural frequency.
- Thesis dissertation.

## 1.4 Hypothesis

Using the hybrid composite material in the spar caps of the hydrokinetic turbine blade, the mass can be decreased and the structural safety factors can be increased.

## 1.5 Methodology

The methodology has been divided in two parts. The first one is the general thesis development process and the second one is a detailed flowchart diagram explaining the steps to be followed on the simulation process.

Figure 1.5 depicts the steps needed for accomplishing the thesis project. A learning process is a crucial step because the author lacks of knowledge about composite materials as well as the simulation program ANSYS Composite PrepPost (ACP) and aero- and hydrodynamics. The next step is a state of the art and background review, where the prior blade versions (detailed on Section 1.1) are analyzed for a better understanding of the current problem.

Once the author has enough experience in all these fields, the definition of the hybrid composite material (Section 2.1) is performed in ACP, ensuring that both physical and simulation results match satisfactorily.

Figure 1.6 shows the sequence to be followed on the simulation process. Since all three mechanical elements of the blade are very likely to have different composite lay-up, a structural simulation is to be made each time one of these elements change. If there is no composite failure in the structure, an eigenvalue buckling analysis is realized. A minimum safety buckling factor of 2 is established for this application. Once the blade fulfills this requirement, a modal analysis is executed, the operation conditions of hydrokinetic blades is around 2 Hz, therefore, the first modal of the blade should be at least ten times greater.

After the blade has satisfied all these analyses, an optimization process is implemented aiming to reduce the total mass of the blade. If this step threatens the structural integrity of the blade, it will be omitted.

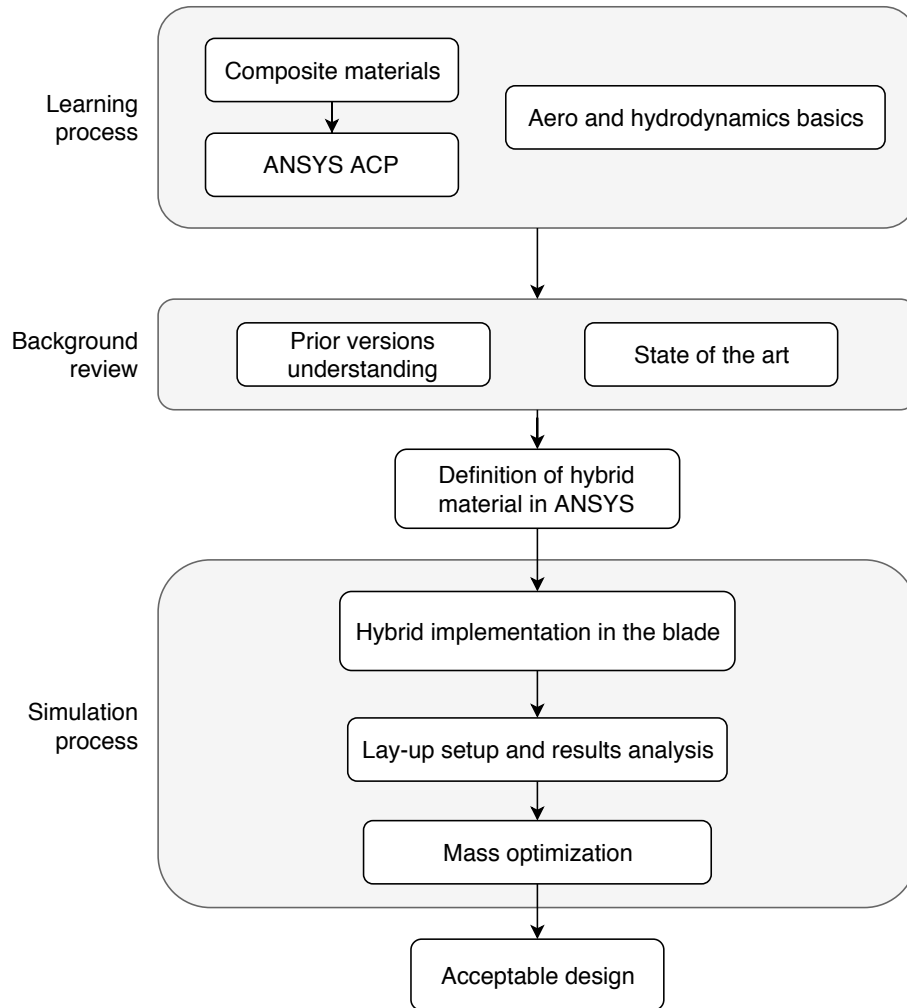


Figure 1.5: Thesis methodology diagram.

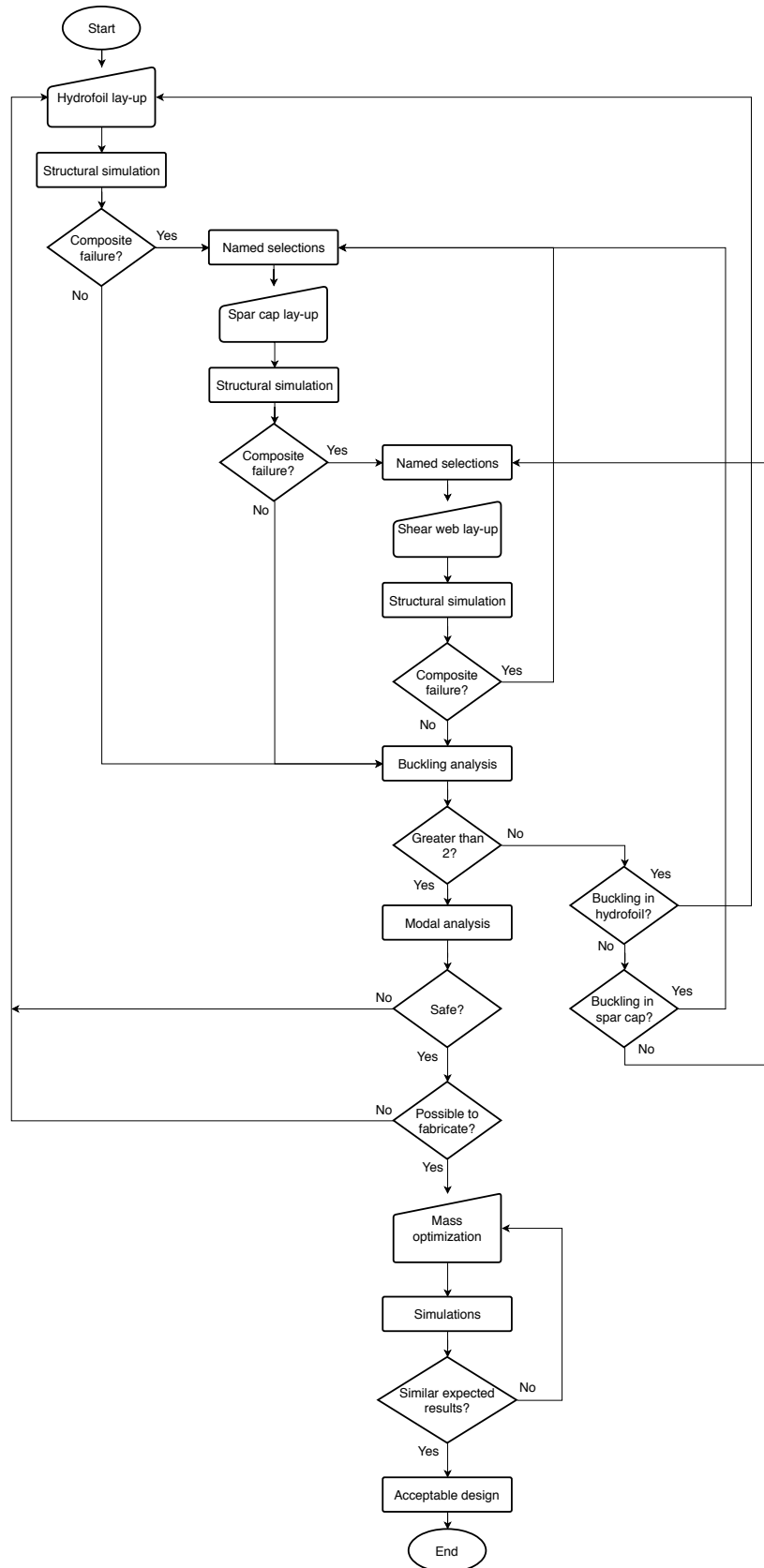


Figure 1.6: Flowchart of simulation process methodology.



# Chapter 2

## State of the art

### 2.1 Hybrid composite material

In the project report of Siu, Alfredo [9], the tests and results implemented on specimens of an hybrid composite material made of Carbon Fiber (CF) and Glass Fiber (GF) are presented for its evaluation in the use on the spar caps of turbine blades.

The hybrid material consists of five plies, two of CF and three of GF, as depicted in Figure 2.1, all of them oriented to  $0^\circ$ . The CF plies are located in the outer layers of the laminate since these layers are more likely to be subjected to higher stresses due to bending and also CF offers higher mechanical resistance compared to GF.

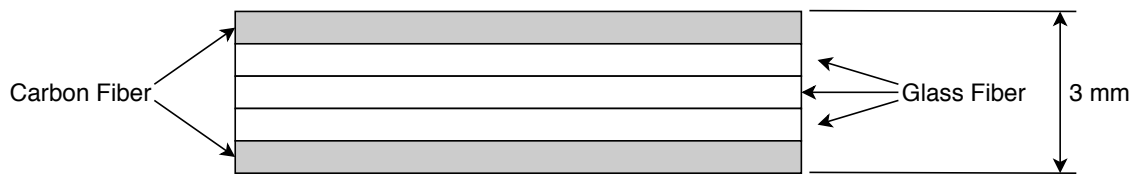


Figure 2.1: Cross-section scheme of the hybrid material laminate.

The summarized results for mechanical properties at  $0^\circ$  and  $90^\circ$  on the hybrid specimens can be observed in Table 2.1, and Table 2.2, respectively. Comparing both results, it becomes obvious that the hybrid material is almost useless under stresses and strains applied at  $90^\circ$ .

In order to perform structural simulations in ANSYS, more orthogonal material properties are required. These assumptions are listed in section 4.1.

Table 2.1: Mechanical properties of hybrid composite laminates at 0°. Adapted from [9]

Property	Value	Unit
Ultimate Tension Strength	1076.1	MPa
Tensile Elastic Modulus	56.13	GPa
Ultimate Compressive Strength	418.7	MPa
Compressive Elastic Modulus	4	GPa
Shear Strength	68.56	MPa
Shear Modulus	4.57	GPa
Poisson's Ratio	0.295	

Table 2.2: Mechanical properties of hybrid composite laminates at 90°. Adapted from [9]

Property	Value	Unit
Ultimate Tension Strength	46.83	MPa
Tensile Elastic Modulus	12.78	GPa
Ultimate Compressive Strength	111.53	MPa
Shear Strength	68.56	MPa
Shear Modulus	4.57	GPa
Poisson's Ratio	0.295	

## 2.2 Aero- and hydrodynamic blade research

Wind and hydrokinetic turbines blades are very similar. In simple words, their main goal is to create mechanical rotational movement due to the "Reaction force" caused by "lift and drag forces" generated by the hydro- or aerodynamic profiles around a rotor. This movement is delivered to the generator by a shaft and then converted into electrical energy (Figure 2.2).

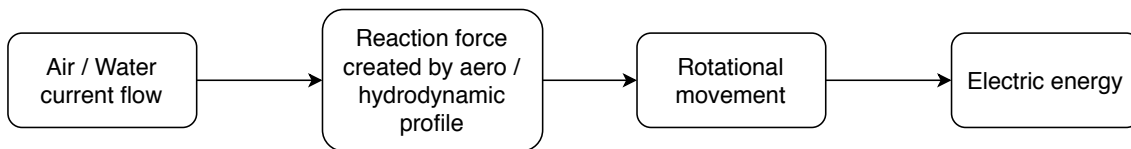


Figure 2.2: Diagram of power generation by wind/hydrokinetic turbine.

The main difference between these blades is that water is much denser than air and the forces experience along hydrokinetic blades are, therefore, much greater. Hence, the following review of the state of the art is focused on both kind of blades.

### 2.2.1 Aerodynamics of wind turbines

In the book by Hanse, M. [1], wind turbine blades are described as long and slender structures where the spanwise velocity component is much lower than the streamwise component. If wind is taken as a component,  $V_\infty$  (known as velocity at infinity), a reacting force  $F$  is created as a result of the velocity difference between the spanwise and the streamwise components. This force can be decomposed into "Lift force",  $L$ , (perpendicular to  $V_\infty$ ), and "Drag force",  $D$ , (parallel to  $V_\infty$ ) as depicted in Figure 2.3.

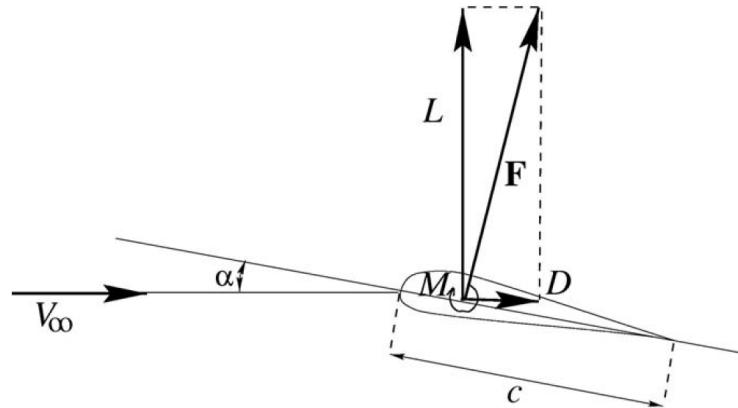


Figure 2.3: Lift and drag force forces in an aerodynamic profile. Taken from [1]

If the aerofoil is designed for an aircraft it is obvious that the  $L/D$  ratio should be maximized. The lift is the force used to overcome gravity and the higher the lift the higher the mass that can be lifted off the ground. This analogy can be applied to wind or hydrokinetic turbines, where Lift has to overcome the inertia of the shaft in the generator in order to start producing energy.

### 2.2.2 Sandwich Materials for Wind Turbine Blades

In the work of Thomsen [10] sandwich composite materials for wind turbines are reviewed. It is mentioned that turbine blades are designed with a load-carrying main spar that supports an outer hydrodynamic shell. Usually, blade's structural design consists of spar caps and shear web, as shown in Figure 2.4 . Globally the blade should be sufficiently stiff in order not to collide with the tower during operational and extreme loading. Locally the spar together with the stiffness of the outer shell ensures that the shape of the aerodynamic profile is maintained as stable as possible.

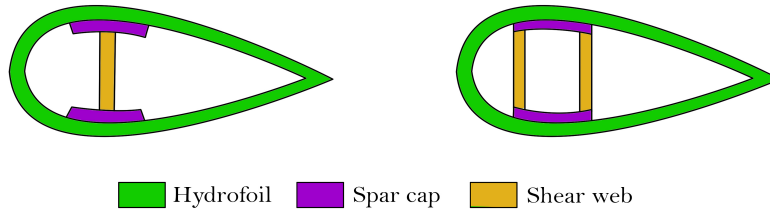


Figure 2.4: Traditional spar caps and shear webs configuration in aerofoils.

The main typically adopted design features in wind turbines is also commented (Figure 2.5):

- Main spar: usually extends from the root of the blade to a position close to the tip. The primary function of the main spar is to transfer the bladewise bending load, and thus it has to perform as a beam.
- Spar cap: The primary function of the spar cap section is to carry the flapwise bending moment.
- Shear webs/stiffener: The function of the webs is to carry the flapwise shear forces.

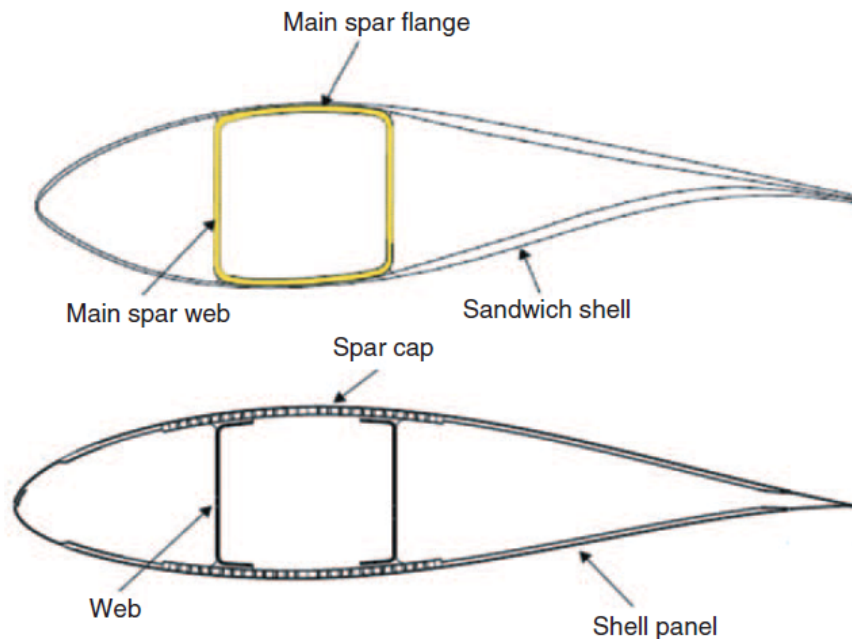


Figure 2.5: Blade design concepts: Above: Traditional design with internal main spar. Below: Design with internal shear webs. Taken from [10]

Furthermore, Thomsen listed that a number of criteria must be considered in the design of the main spar:

- Global stiffness (blade tip deflection, tower clearance).
- Buckling resistance (main flage or spar cap on suction of airfoil).
- Blade eigenfrequencies. The blade eigenfrequencies should not coincide with the tower passing frequencies.
- Material failure under static loading.
- Local face instability of sandwich parts.

### 2.2.3 Design of composite tidal turbine blades

Grogan et al. [11] published their results from designing a 12 m tidal turbine blade for the generation of 1.5 MW power output. They sought to develop a design methodology for tidal turbine blades based on a combined hydrodynamics-structural model with a view to exploring the suitability of using Glass Fiber Reinforced Polymer (GFRP) and Carbon Fiber Reinforced Polymer (CFRP) as blade construction materials.

The methodology used for the structural design, depicted in Figure 2.6, can be summarized as follows:

1. Calculation of the main blade loadings.
2. Material selection.
3. Blade thickness distribution and composite lay-up selection.
4. Strain concentration reduction.
5. Finite element analysis.

When talking of the structural part, it can be noted from point 3 to 5, Grogan et al. used the program PreComp for determining force distributions of the blade as well as to create an optimized blade shape before using a Finite Element Analysis (FEA) program for more detailed and accurate results in order to save computing power and time.

In their results, it was found that strains predicted by the program PreComp for GFRP caps are greater than the CFRP as was expected. Even when using laminates with a thickness of over 100 mm, the strains obtained are too close to the failure strain of the material and with the majority of the blade experiencing 1 % of failure over the lifetime of

the turbine is significant. Because of that, CFRP was used in the spar caps and it shown a great improvement in the stiffness of the blade with the maximum strain registered being approximately 4 times lower than for GFRP for a similar lay-up.

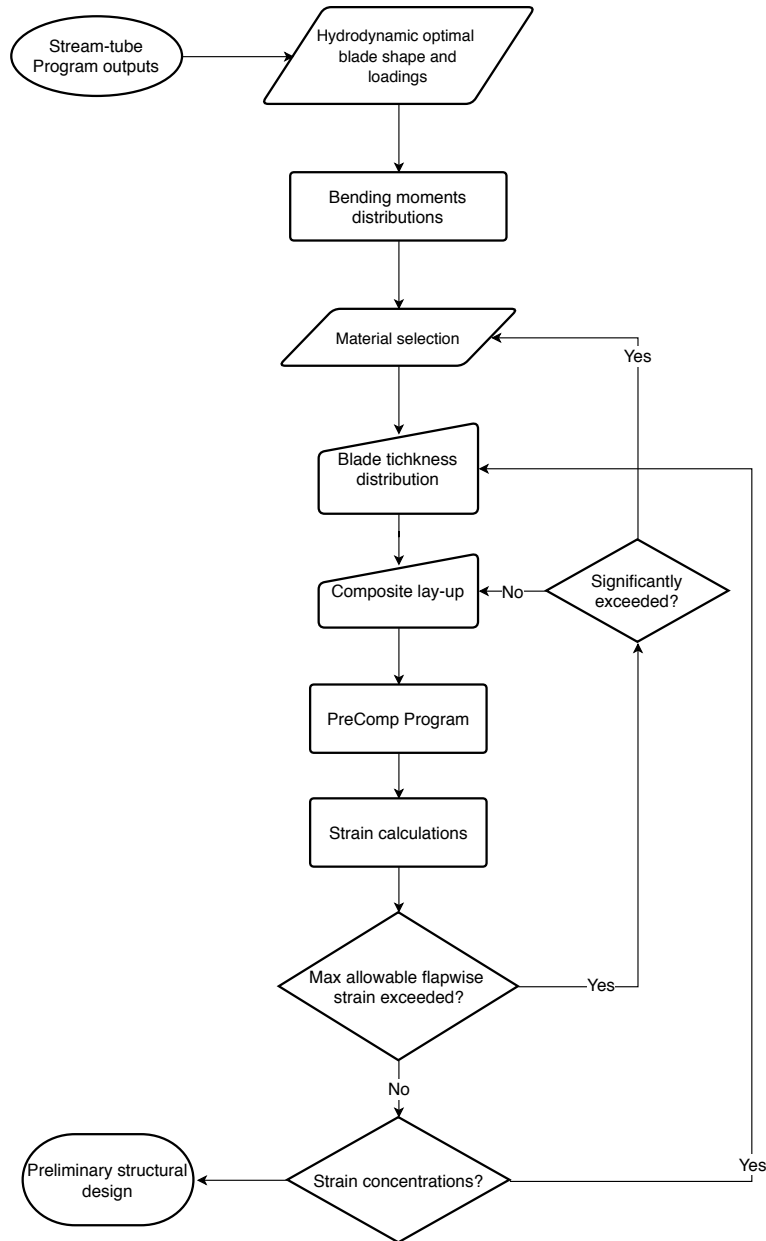


Figure 2.6: Flowchart of structural modelling process. Taken from [11]

## **2.2.4 Structural optimization study of composite wind turbine blade**

Chen, J. et al. [12] designed the initial layout of a 31 meter 2 MW composite wind turbine blade. They started using a layout with three main types of glass/epoxy composites which are: unidirectional laminate, bi-axial and tri-axial laminate.

A procedure combining FEA and particle swarm algorithm to optimize composite structures of the wind turbine blade is developed. The procedure proposed not only allows thickness variation, but also permits the spar cap location variation over the structure. Results obtained in the two optimal schemes reported in this paper show that this procedure leads to significant weight savings. Then the strain of the blade is analyzed, and the location of the main bending strain is pointed out. The next step could be the multi-objective optimization of the wind turbine blade.

The main contribution of this paper is that optimizing thicknesses of the structural part of the blade can lead to a significant reduction in the mass and this is translated into less stresses on the blade due to gravity.

## **2.2.5 Structural investigation of composite wind turbine blade considering structural collapse in full-scale static tests**

Yang, J. et al. [13] worked with an actual collapse testing under the flap-wise loading for a large full-scale composite wind turbine blade, and a discussion is conducted to assess and evaluate the structural response of the blade during loading and after collapse by correlating experimental findings with numerical model predictions.

In their paper, they commented that while designed appropriately, the wind turbine blade should be able to withstand the extreme load, the fatigue and other hostile environment over the whole lifetime. Therefore, designers must carefully consider the structural behavior of the blades in their structural design and must test the full-size structure.





# Chapter 3

## Theoretical background

### 3.1 Composite materials

Structural materials can be divided into four basic categories as metals, polymers, ceramics, and composites. Composites, which consist of two or more separate materials combined in a structural unit, are typically made from various combinations of the other three materials. Composites are generally used because they have desirable properties that cannot be achieved by any of the constituent materials acting alone [14].

#### 3.1.1 Lamina stress-strain relationships

Fibrous reinforcement is very effective because many materials are much stronger and stiffer in fiber form than they are in bulk form, such as glass and carbon. The basic building block of a composite structure is the lamina, which usually consists of one of the fiber/matrix configurations shown in Figure 3.1. However, for the the “unidirectionally reinforced” or “unidirectional” lamina with an arrangement of parallel, continuous fibers is the most convenient starting point.

An unidirectional composite lamina has three mutually orthogonal planes of material property symmetry (i.e., the 12, 23, and 13 planes) and is called an orthotropic material, depicted in Figure 3.2.

When a material is characterized experimentally, the so-called “engineering constants” such as Young’s modulus (or modulus of elasticity), shear modulus, and Poisson’s ratio are usually measured instead of the stiffness matrix,  $C_{ij}$  or compliance matrix,  $S_{ij}$  used for the stress-strain relationship. The engineering constants are also widely used in analysis and design because they are easily defined and interpreted in terms of simple states of stress and strain.

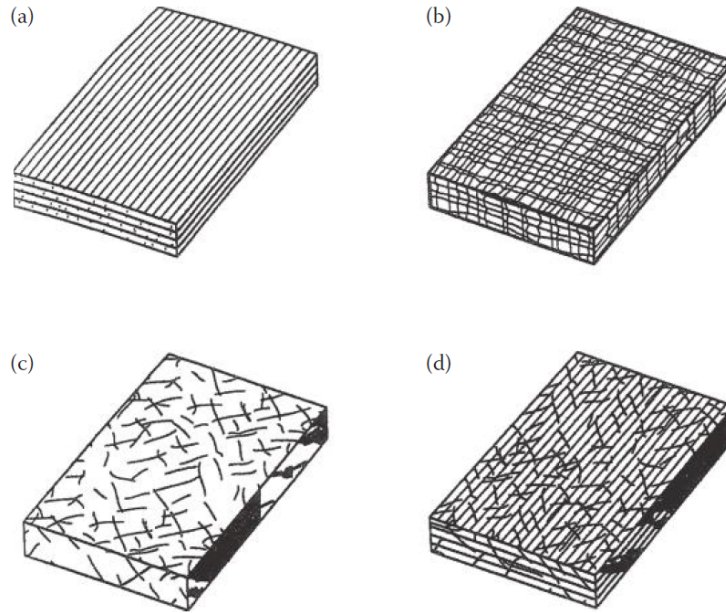


Figure 3.1: Types of fiber-reinforced composites. (a) Continuous fiber composite, (b) woven composite, (c) chopper fiber composite, and (d) hybrid composite. Taken from [14]

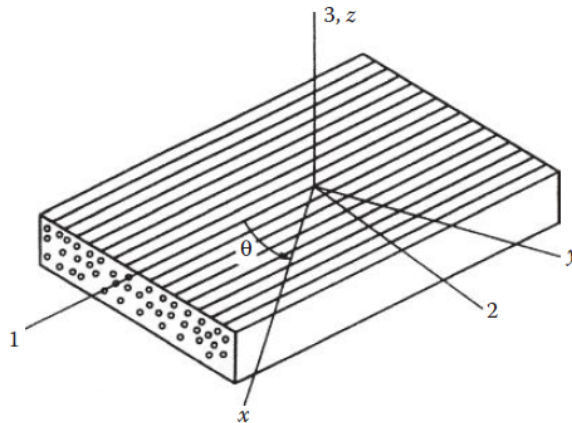


Figure 3.2: Orthotropic lamina with principal (123) and nonprincipal ( $xyz$ ) coordinate system. Taken from [14]

Consider a simple uniaxial tensile test consisting of an applied longitudinal normal stress,  $\sigma_1$ , along the reinforcement direction (i.e., the 1 direction) of a specimen from an orthotropic material, as shown in Figure 3.3a. It is assumed that all other stresses are equal to zero.

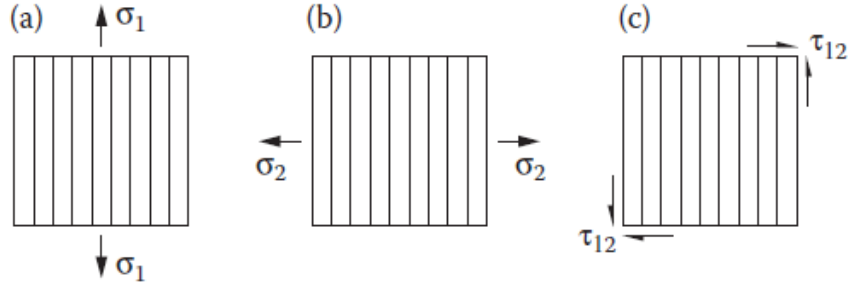


Figure 3.3: Simple states of stress used to define engineering constants. (a) applied longitudinal normal stress, (b) applied transverse normal stress, and (c) applied in-plane shear stress. Taken from [14]

Within the linear range the experimental observation is that the resulting strains associated with the 123 axes can be expressed empirically in terms of the "engineering constants" as

$$\varepsilon_1 = \frac{\sigma_1}{E_1} \quad (3.1a)$$

$$\varepsilon_2 = -\nu_{12}\varepsilon_1 = -\frac{\nu_{12}\sigma_1}{E_1} \quad (3.1b)$$

$$\varepsilon_3 = -\nu_{13}\varepsilon_1 = -\frac{\nu_{13}\sigma_1}{E_1} \quad (3.1c)$$

$$\gamma_{12} = \gamma_{23} = \gamma_{13} = 0 \quad (3.1d)$$

where  $E_1$  = longitudinal modulus of elasticity associated with the 1 direction, and  $\nu_{ij} = -\varepsilon_j/\varepsilon_i$  is the Poisson's ratio, the ratio of the strain in the  $j$  direction to the strain in the perpendicular  $i$  direction when the applied stress is in the  $i$  direction.

Recall from mechanics of materials that for isotropic materials, no subscripts are needed on properties such as the modulus of elasticity and Poisson's ratio because the properties are the same in all directions. This is not the case with orthotropic materials, however, and subscripts are needed on these properties because of their directional nature. For example,  $E_1 \neq E_2$  and  $\nu_{12} \neq \nu_{21}$ .

Now, consider a transverse normal stress,  $\sigma_2$ , is applied to the same material as shown in Figure 3.3b, with all other stress being equal to zero. Now the experimental observation is that the resulting strains can be expressed as in Equations 3.2.

$$\varepsilon_2 = \frac{\sigma_2}{E_2} \quad (3.2a)$$

$$\varepsilon_1 = -\nu_{21}\varepsilon_2 = -\frac{\nu_{21}\sigma_2}{E_2} \quad (3.2b)$$

$$\varepsilon_3 = -\nu_{23}\varepsilon_2 = -\frac{\nu_{23}\sigma_2}{E_2} \quad (3.2c)$$

$$\gamma_{12} = \gamma_{23} = \gamma_{13} = 0 \quad (3.2d)$$

where  $E_2$  is the transverse modulus of elasticity associated with the 2 direction. A similar result for an applied transverse normal stress,  $\sigma_3$ , can be obtained by changing the appropriate subscripts in Equation 3.2.

Next, consider a shear test where a pure shear stress,  $\sigma_{12} = \tau_{12}$ , is applied to the material in the 12 plane, as depicted in Figure 3.3c. Now, the experimental observation is that the resulting strains can be written as

$$\gamma_{12} = \frac{\tau_{12}}{G_{12}} \quad (3.3a)$$

$$\varepsilon_1 = \varepsilon_2 = \varepsilon_3 = \gamma_{13} = \gamma_{23} = 0 \quad (3.3b)$$

where  $G_{12}$  is the shear modulus associated with the 12 plane. Similar results can be obtained for pure shear in the 13 and 23 plane by changing the appropriated subscripts in Equation 3.3a and 3.3b.

### 3.1.2 Strength of a continuous fiber-reinforced lamina

Because of the variety of failure modes that can occur in composites, the analysis of composite strength is more difficult than the analysis of elastic behavior. The strength of a composite is derived from the strength of the fibers, but this strength is highly directional in nature.

The stress-strain curves in Figure 3.4 shows the graphical interpretation of three simple states of stress, the effective strengths  $S_L^{(+)}$ ,  $S_L^{(-)}$ ,  $S_T^{(+)}$ ,  $S_T^{(-)}$ , and  $S_{LT}$ , and the corresponding ultimate strains  $e_L^{(+)}$ ,  $e_L^{(-)}$ ,  $e_T^{(+)}$ ,  $e_T^{(-)}$  and  $e_{LT}$ .

Furthermore, it can be observed that the transverse tensile strength,  $S_T^{(+)}$ , is the lowest of all stresses. This is because, when the loading is perpendicular to the fibers as shown in Figure 3.5, stress and strain concentrations occur in the matrix around the fibers (i.e., the fibers create discontinuities in the matrix) and reduces the tensile strength of the material. If we assume linear elastic behavior up to failure, ultimate stresses are related ultimate strains by:

$$S_L^{(+)} = E_1 e_L^{(+)} \quad (3.4a)$$

$$S_L^{(-)} = E_1 e_L^{(-)} \quad (3.4b)$$

$$S_T^{(+)} = E_2 e_T^{(+)} \quad (3.4c)$$

$$S_T^{(-)} = E_2 e_T^{(-)} \quad (3.4d)$$

$$S_{LT} = G_{12} e_{LT} \quad (3.4e)$$

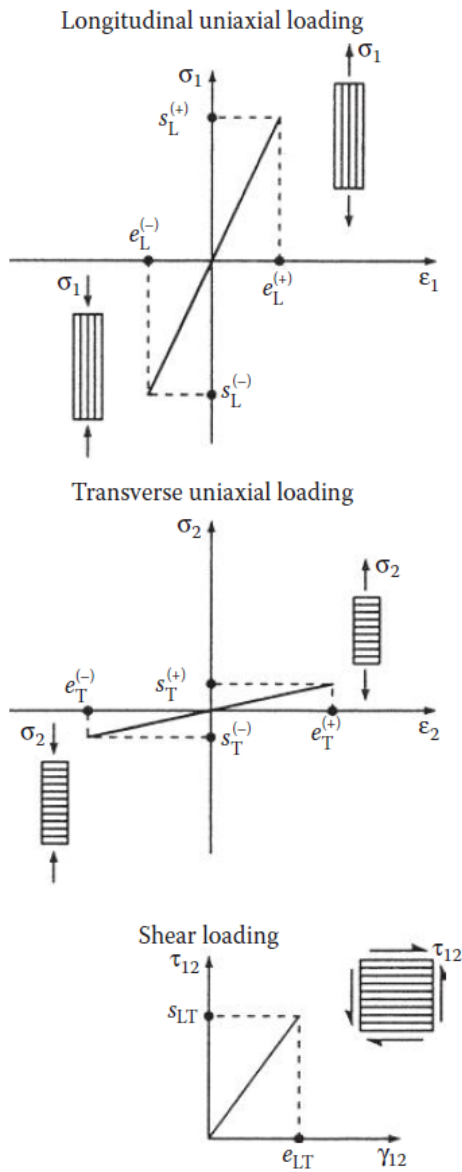


Figure 3.4: Stress–strain curves for uniaxial and shear loading showing lamina in-plane strengths and ultimate strains. Taken from [14]

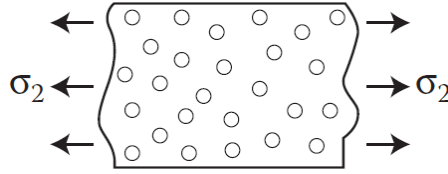


Figure 3.5: For composites under transverse loading, the fibers create discontinuities in the matrix that lead to stress and strain concentrations. Taken from [14]

### 3.1.3 Maximum Stress Criterion

The Maximum Stress Criterion predicts failure when any principal material axis stress component exceeds the corresponding strength. Thus, to avoid failure according to this criterion, the following set of inequalities must be satisfied:

$$-S_L^{(-)} < \sigma_1 < S_L^{(+)} \quad (3.5a)$$

$$-S_T^{(-)} < \sigma_2 < S_T^{(+)} \quad (3.5b)$$

$$|\tau_{12}| < S_{LT} \quad (3.5c)$$

where the numerical values of  $S_L^{(-)}$  and  $S_T^{(-)}$  are assumed to be positive. It is assumed that shear failure along the principal axis is independent of the sign of the shear stress  $\tau_{12}$ . Thus, only the magnitude of  $\tau_{12}$  is important in the Equation 3.5c.

The failure surface for the Maximum Stress Criterion in  $\sigma_1, \sigma_2$  space is a rectangle, as shown in Figure 3.6. Note that this failure surface is independent of the shear stress  $\tau_{12}$ , and that the criterion does not account for possible interaction between the stress components. That is, the predicted limiting value of a particular stress component is the same whether or not other stress components are presented.

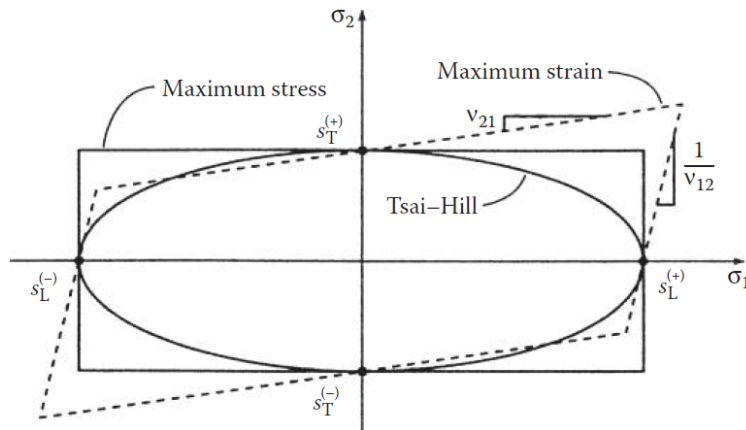


Figure 3.6: Maximum stress, maximum strain, and Tsai-Hill failure surfaces in  $\sigma_1, \sigma_2$  space. Taken from [14]

### 3.1.4 Maximum Strain Criterion

This criterion predicts failure when any principal material axis strain component exceeds the corresponding ultimate strain. In order to avoid failure according to this criterion, the following set of inequalities must be satisfied:

$$-e_L^{(-)} < \varepsilon_1 < e_L^{(+)} \quad (3.6a)$$

$$-e_T^{(-)} < \varepsilon_2 < e_T^{(+)} \quad (3.6b)$$

$$|\gamma_{12}| < e_{LT} \quad (3.6c)$$

where the numerical values of  $e_L^{(-)}$  and  $e_T^{(+)}$  are assumed to be positive and the ultimate strains are all engineering strains as defined by Equations 3.4. As with the Maximum Stress Criterion, it is assumed that shear failure along the principal material axes is independent of the sign of the shear strain  $\gamma_{12}$ .

### 3.1.5 Quadratic Interaction Criteria (Tsai-Hill Criterion)

The so-called quadratic interaction criteria also evolved from early failure theories for isotropic materials, but they differ from the Maximum Stress and Maximum Strain Criteria in that they include terms to account for interaction between the stress components, and the quadratic forms of the equations for plane stress lead to elliptical failure surfaces. In 1948, Sir Austin Bradford Hill suggested that the von Mises Criterion could be modified to include the effects of induced anisotropic behavior in initially isotropic metals during large plastic deformations.

For a general three-dimensional state of stress along the principal axes of anisotropy (the 123 axes) in such a material, the failure surface (or yield surface) for the Hill Criterion in  $\sigma_1, \sigma_2, \sigma_3$  space is described by the equation:

$$A(\sigma_2 - \sigma_3)^2 + B(\sigma_3 - \sigma_1)^2 + C(\sigma_1 - \sigma_2)^2 + 2D\tau_{23}^2 + 2E\tau_{31}^2 + 2F\tau_{12}^2 = 1 \quad (3.7)$$

where A, B, C, D, E, and F are determined from yield strengths in uniaxial or shear loading. In order to avoid failure, the left-hand side of Equation 3.7 must be  $<1$ , and failure is predicted if the left-hand side is  $\geq 1$ .

The extension of the Hill criterion to prediction of failure in an orthotropic, transversely isotropic lamina was suggested by Azzi and Tsai; the resulting equation is often referred as the Tsai-Hill Criterion. If the 123 directions are assumed to be the principal material axes of the orthotropic transversely isotropic lamina, with the 1 direction being along the reinforcement direction, if plane stress is assumed ( $\sigma_3 = \tau_{31} = \tau_{23} = 0$ ) and if Hill's anisotropic yield strengths are replaced by the corresponding effective lamina strengths, then  $\gamma_1 = S_L$ ,  $\gamma_2 = \gamma_3 = S_T$ , and  $\gamma_{12} = S_{LT}$ ,

and Equation 3.7 and its simplifications reduce to the equation for the Tsai-Hill failure surface:

$$\frac{\sigma_1^2}{S_L^2} - \frac{\sigma_1\sigma_2}{S_L^2} + \frac{\sigma_2^2}{S_T^2} + \frac{\tau_{12}^2}{S_{LT}^2} = 1 \quad (3.8)$$

As with the Hill equation, failure is avoided if the left-hand side of Equation 3.8 is  $<1$ , and failure is predicted if the left-hand side is  $\geq 1$ .

### 3.1.6 Laminates

While an understanding of lamina mechanical behavior is essential to the development of theories for the analysis of composite materials, the unidirectional lamina alone is generally not very useful as a structural element because of its poor transverse properties. Composite structures are more likely to be in the form of laminates consisting of multiple laminae or plies oriented in the desired directions and bonded together in a structural unit. The virtually limitless combinations of ply materials, ply orientations, and ply-stacking sequences offered by laminated construction considerably enhance the design flexibility inherent in composite structures.

The need for adequate description of many possible combinations of ply orientations and stacking sequences in laminates, a laminate orientation code has evolved in the composites literature. The basis of the code is that ply angles, separated by slashes, are listed in order from the top surface to the bottom surface and enclosed in square brackets, as shown by the examples in Figure 3.7. For hybrid laminates having plies of different materials, additional subscripts on the ply angles may be used to identify the ply material.



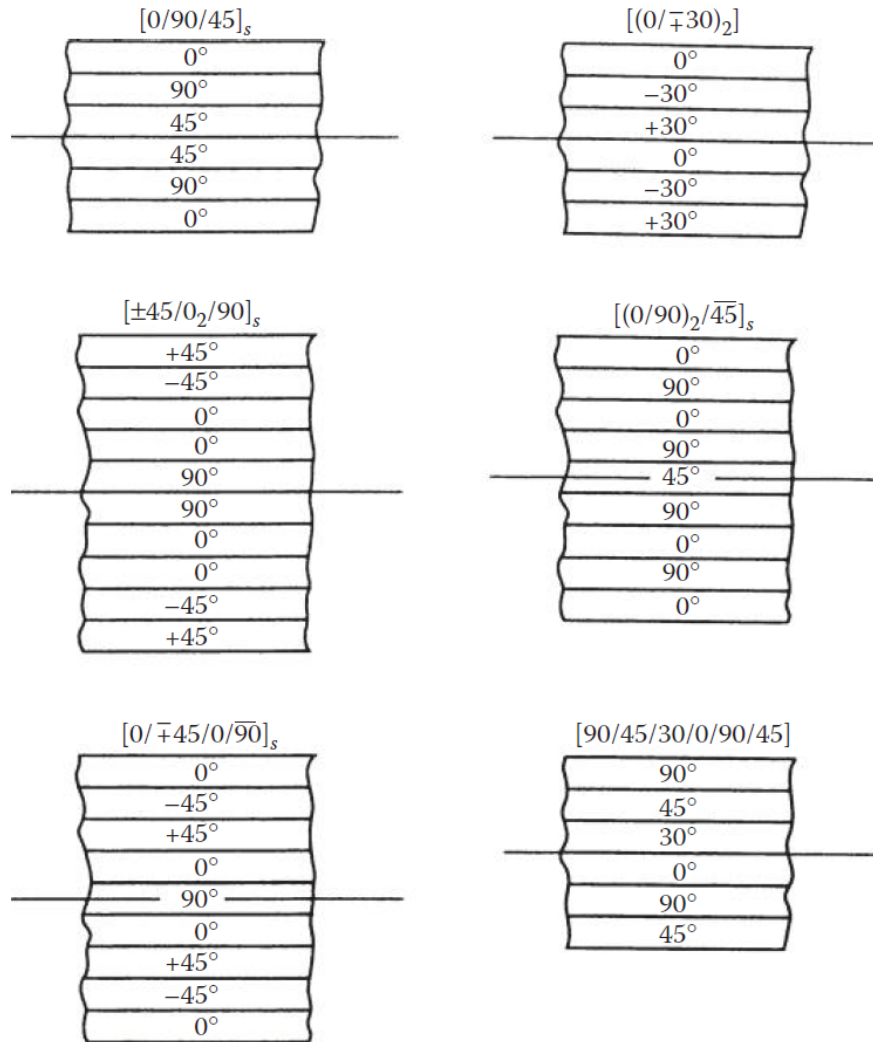


Figure 3.7: Examples of laminate stacking sequences and the corresponding laminate orientation codes. Taken from [14]

### 3.1.7 Theory of laminated beams

#### 3.1.7.1 Flexural Stresses and Deflections

For the purpose of analysis, the simplest laminated structure is a laminated beam that is subjected to pure bending. A theory of laminated beams in pure flexure can be developed from the Bernoulli–Euler theory of elementary mechanics of materials.

A section of a rectangular laminated beam of depth  $h$  and width  $b$  is shown in Figure 3.8 before and after the application of a bending moment  $M$ . The assumptions used in developing the analysis are as follows:

1. Plane sections that are initially normal to the longitudinal axis of the beam remain plane and normal during flexure.

2. The beam has both geometric and material property symmetry about the neutral surface (i.e., the plies are symmetrically arranged about the  $xy$  plane).
3. Each ply is linearly elastic with no shear coupling (i.e., ply orientations are either  $0^\circ$  or  $90^\circ$ ).
4. The plies are perfectly bonded together, so that no slip occurs at ply interfaces.
5. The only stress components present are  $\sigma_x$  and  $\tau_{xy}$ .

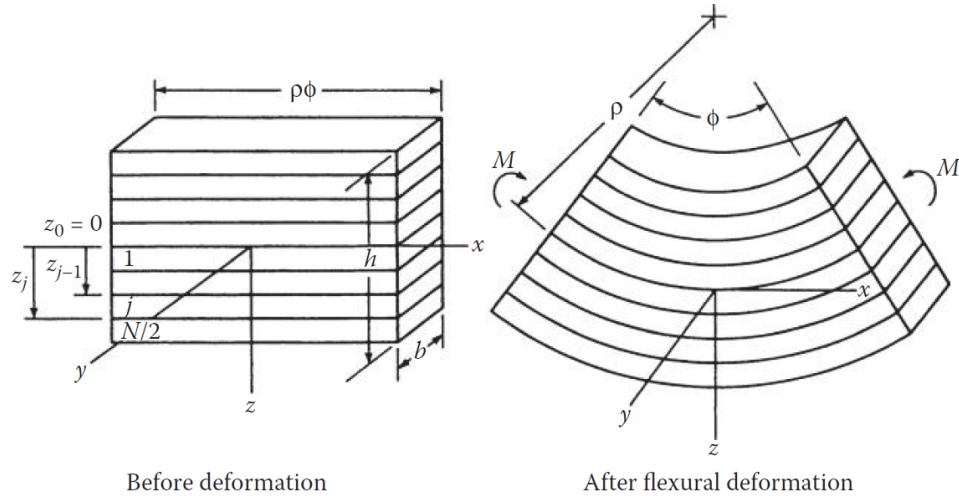


Figure 3.8: An element of a laminated beam before and after the application of a bending moment. Taken from [14]

The effective flexural modulus of a laminated beam can be expressed as Equation 3.9:

$$E_f = \frac{8}{h^3} \sum_{j=1}^{N/2} (E_x)_j (z_j^3 - z_{j-1}^3) \quad (3.9)$$

where  $E_f$  is the effective flexural modulus,  $N$  is the total number of plies,  $E_x$  is the Young's modulus of the  $j$ th ply along the  $x$  direction and  $z$  is the distance from the neutral surface.

Or for an even number of uniform thickness plies, Equation 3.9 changes to

$$E_f = \frac{8}{N^3} \sum_{j=1}^{N/2} (E_x)_j (3j^2 - 3j + 1) \quad (3.10)$$

The flexural deflections of laminated beams can be calculated by using the flexural modulus in place of the Young's modulus in the beam deflection equations from elementary mechanics of materials. For example, the maximum flexural deflection,  $w_{fmax}$ , at the tip of the laminated beam in Figure 3.9 would be given by Equation 3.11.

$$E_f I_{yy} \frac{d^2 w_f}{dx^2} = M \quad (3.11)$$

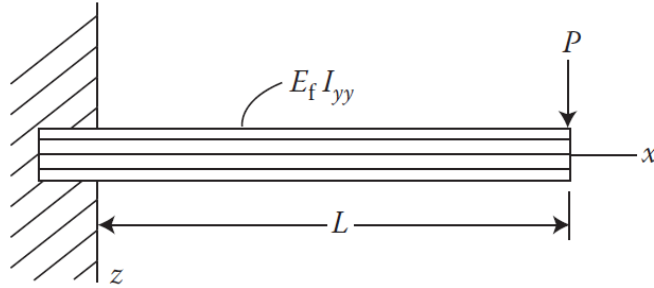


Figure 3.9: Cantilever beam under concentrated tip load. Taken from [14]

where  $P$  is the concentrated tip load and  $L$  is the beam length. An important observation is that the maximum stress in the laminated beam does not always occur on the outer surface as it does on homogeneous, isotropic beam. Figure 3.10 depicts a schematic comparison.

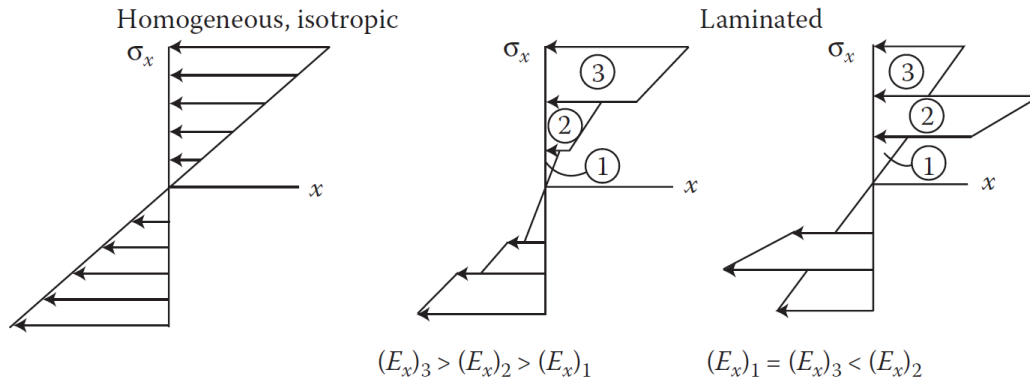


Figure 3.10: Stress distribution in homogeneous, isotropic beams and in laminated beams. Taken from [14]

One of the difficulties in laminates is that only failures on the outer surfaces can be observed with the naked eye. Interior ply failures can only be detected by methods such as ultrasonic or x-ray inspection.

### 3.1.8 Selection of laminate designs

When designing with conventional isotropic materials, the problem of material selection is usually solved by simply looking up the appropriate properties of candidate materials in a handbook. The selection of a composite laminate design can be a formidable task due to the large number of available fiber and matrix materials and the endless variety of laminate configurations.

A typical analysis problem would be given a composite laminate and allowable ply stresses, determine the loads that it will support, or given the laminate, loads, and properties, determine the resulting stresses and strains. Either way, the analysis problem has a unique solution. A typical design problem would be, given a set of loads and other design constraints, select the materials and laminate configuration to withstand the loads. As opposed to the analysis problem, the design problem may have an infinite number of solutions. A general flow chart showing the laminate design sequence is shown in Figure 3.11.

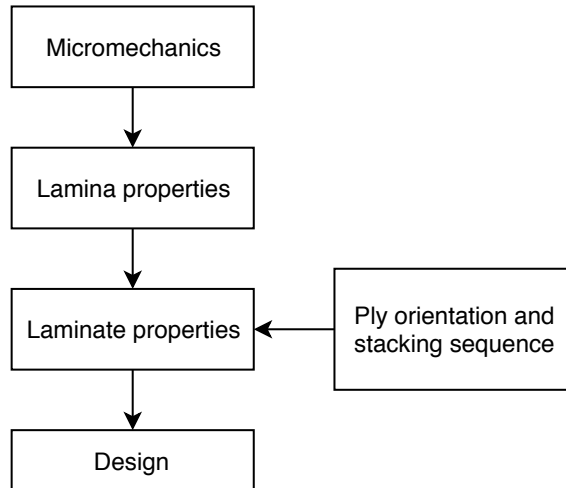


Figure 3.11: Flow chart for laminate analysis. Taken from [14]

An essential component of any design problem is the identification all of the possible failure modes. Whether intentional or not, if a particular failure mode is overlooked in the design process, that failure mode is the one that will most likely come back to haunt the designer. A list of the major design criteria for composite laminates and the associated failure modes are provided in Table 3.1.

Table 3.1: Design criteria for composite laminates and associated failure modes.  
Taken from [14]

Design criteria	Associated Failure Modes
Strength	Fracture (either partial or complete)
Stiffness	Excessive deformation
Stability	Buckling
Hygrothermal effects	Property degradation, expansion and contraction, residual stresses
Life or durability	Fatigue, creep
Weight	Heavier than conventional designs
Cost	Not affordable
Manufacturability	Impractical to build, wrapping due to residual stresses

In order to use the laminate analysis equations that were derived and discussed earlier, extensive matrix algebra is obviously required. In addition, proper evaluation of laminate designs requires numerous repetitive calculations resulting from changes in loading conditions, material properties, and laminate geometry. These computational requirements are ideally suited for solutions by digital computers, and a variety of software packages for laminate analysis now exist.

Such programs are indispensable in design and analysis because hand calculations are not only too time consuming, but the possibilities for errors in such hand calculations are endless. For composite structures having complex geometries the preferred analytical tool is the finite element method.

## 3.2 Loads and structural components of wind and hydrokinetic turbine blades

Wind and hydrokinetic turbine blades are exposed to a variety of load due to flow currents, gravity and rotational movement around the hub of the generator. The following load descriptions are based on the work of Schubel, Peter J. and Crossley, Richard J [15].

### 3.2.1 Aerodynamic loads

Aerodynamic load is generated by lift and drag forces of the blades aerofoil section (Figure 3.12), which is dependent on wind or water velocity, blade velocity, surface finish, angle of attack and yaw. The aerodynamic lift and drag produced are resolved into useful thrust in the direction of rotation absorbed by the generator and reaction forces. It can be seen that the reaction forces are substantial acting in the flatwise bending plane, and must be tolerated by the blade with limited deformation.

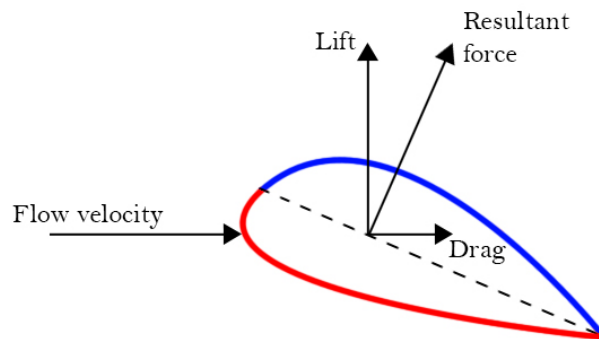


Figure 3.12: Forces interacting with an aero- or hydrofoil.

### 3.2.2 Gravitational and centrifugal loads

Gravitational centrifugal forces are mass dependant which are generally thought to increase cubically with increasing turbine diameter. Therefore, turbines under ten meters diameter have negligible inertial loads, which are marginal for 20 meters upward, and critical for 70 meter rotors and above.

### 3.2.3 Flapwise bending

The flap wise bending moment is a result of the aerodynamic loads, which can be calculated using Blade Element Momentum (BEM) theory. Once calculated, it is apparent that load case can be modeled as a cantilever beam with a uniformly distributed load (Figure 3.13).

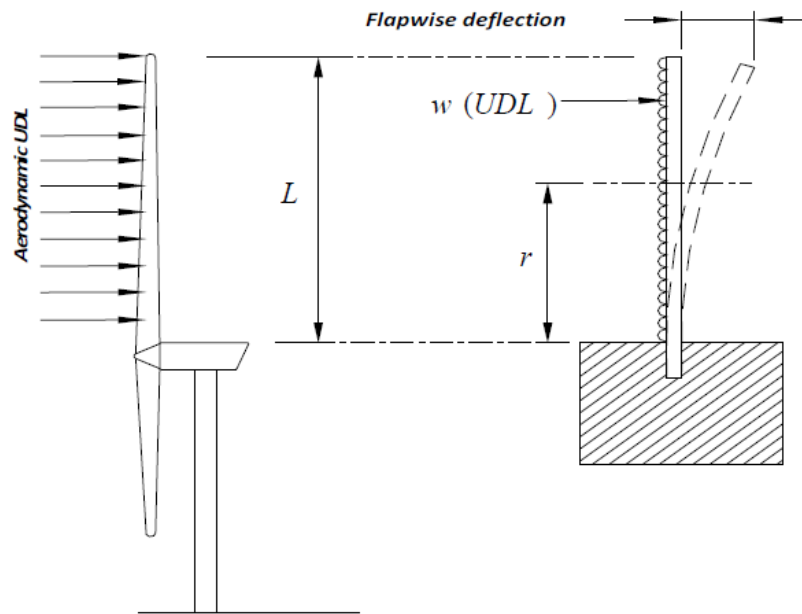


Figure 3.13: Blade modeled as a cantilever beam with uniformly distributed aerodynamic load. Taken from [15]

This analysis shows how bending occurs about the chord axis ( $xx$ ) creating compressive and tensile stresses in the blade cross section (Figure 3.14).

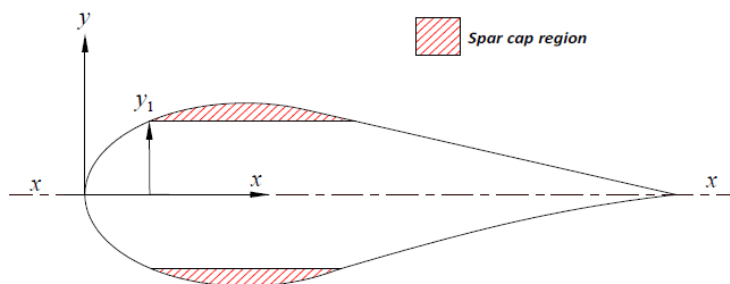


Figure 3.14: Spar cap region in blade cross section. Taken from [15]

### 3.2.4 Edgewise bending

The edgewise bending moment is a result of blade mass and gravity. Therefore this loading condition can be considered negligible for smaller blades with negligible blade mass. Simple scaling laws dictate a cubic rise in blade mass with increasing turbine size. Thus, for increasing turbine sizes in excess of 70 m diameter, this loading case is said to be increasingly critical.

The bending moment is at its maximum when the blade reaches the horizontal position. In this case the blade may once again be modeled as a cantilever beam (Figures 3.15 and 3.16).

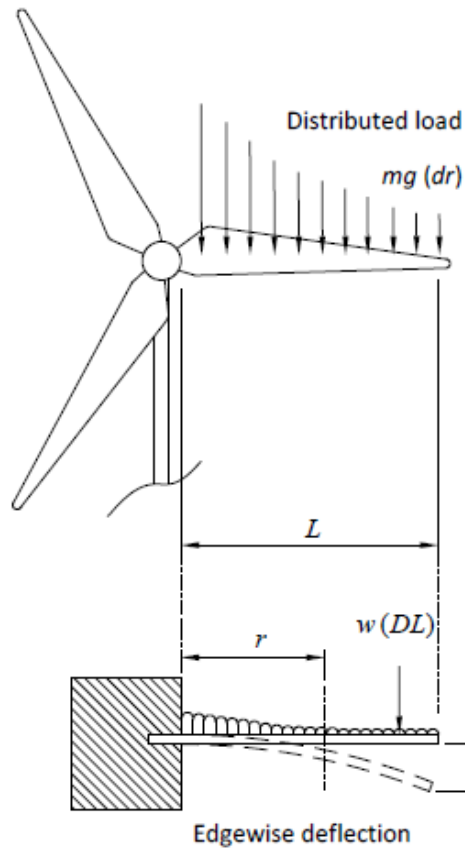


Figure 3.15: Gravitational load modeled as a cantilever beam. Taken from [15]

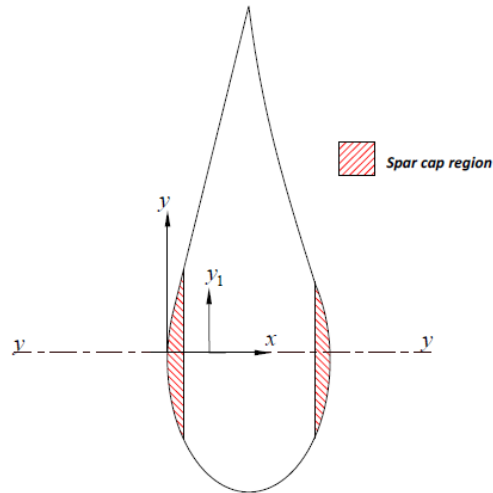


Figure 3.16: Edgewise bending around  $yy$ . Taken from [15]

### 3.3 ANSYS Composite PrepPost (ACP)

ANSYS Composite PrepPost (ANSYS ACP or just ACP) software provides all the necessary functionality for the analysis of layered composite structures. An intuitive interface efficiently defines materials, plies and stacking sequences. Materials can be accurately oriented on the structures using very flexible tools based on coordinate systems definitions [16].

The software offers a wide choice of state-of-the-art failure criteria, along with post-processing capabilities to allow an in-depth investigation of product behavior. The results for the structure can be looked at globally, or viewed in detail down to the layer level, which enables users to identify accurately reasons a structure could potentially fail. Design iterations can easily be performed to take into account geometric changes or material variations.

#### 3.3.1 ANSYS Workbench and ACP

ACP module is divided in Pre and Post blocks inside ANSYS Workbench. In ACP Pre, the user can include material properties, geometry model, mesh of the model and fix the composite lay-ups as well as defined ply orientations.

Depending on the desired analysis, this should be performed after configuring the model in ACP Pre. The result data is then transferred to ACP Post (Figure 3.17). Here, displacements, stresses, strains, failures etc. can be analyzed on the entire model, or each ply separately.



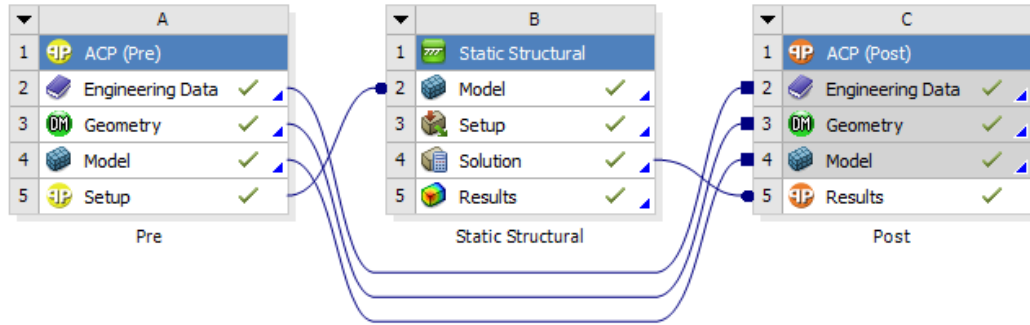


Figure 3.17: Block diagrams example of ANSYS ACP on Workbench.

### 3.3.2 Failure criterion nomenclature

As mentioned before, ACP includes some state of the art and commonly known failure criterion. When analyzing failures on a model, ACP displays failure criteria abbreviations on each element of the mesh as well as color code relating failure magnitudes [17]. An example can be appreciated on Figure 3.18 and failure criteria terms are described on Table 3.2.

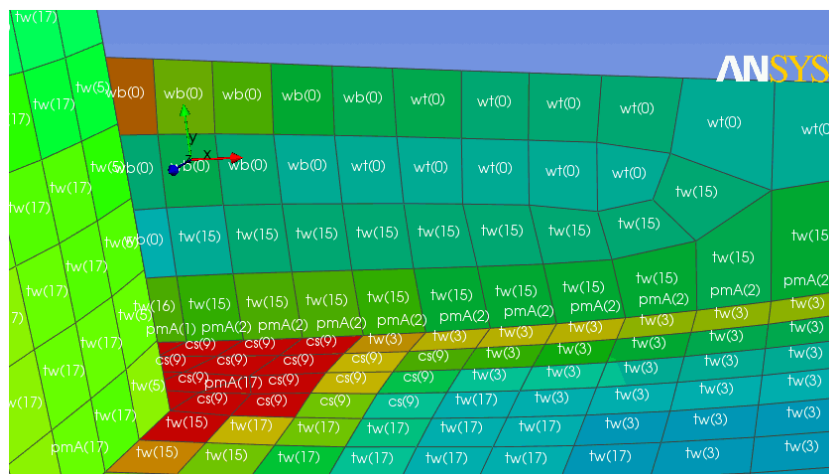


Figure 3.18: Failure criterion and color code example on ACP Post. Taken from [16]

Table 3.2: Failure criterion terms. Adapted from [17]

Term	Meaning
e	Strain
s	Stress
1	Material 1 direction
2	Material 2 direction
3	out-of-plane normal direction
12	in-plane shear
13 and 23	out-of-plane shear terms
I	Principal I direction
II	Principal II direction
III	Principal III direction
t	Tension
c	Compression

While the color code failure magnitude depends directly on the scale picked by ACP or the user, some examples of failure criteria abbreviations are the following:

- **Maximum Strain Failure Modes:** e1t, e1c, e2t, e2c, e12.
- **Maximum Stress:** s1t, s1c, s2t, s2c, s3t, s3c, s12, s23, s13.
- **Tsai-Wu 2D and 3D:** tw.
- **Tsai-Hill 2D and 3D:** th.
- **Hashin:** hf (fiber failure), hm (matrix failure) hd (delamination failure).
- **Puck (simplified, 2D and 3D):** pf (fiber failure), pmA (matrix tension failure), pmB (matrix compression failure), pmC (matrix shear failure), pd (delamination).

# Chapter 4

## Simulation process

### 4.1 Definition of hybrid material in ANSYS

In Section 2.1, characterization of the hybrid composite material was presented. These mechanical properties must be implemented on ANSYS in order to incorporate this new material in the hydrokinetic blade model and afterwards, perform the corresponding simulations.

As it was indicated before, ANSYS Workbench ask for some specific orthotropic material properties which were not included in the report of Siu, A. [9]. Therefore, a number of assumptions have to be made. The assumed material properties listed below are named after the ones required on the Engineering Data of ANSYS Workbench.

- General mechanical properties:
  - **Assumption 1:** The hybrid material is considered as a "single-layered" material with a thickness of 3 mm.
  - **Assumption 2:** The density of the hybrid blade is supposed using a relationship of both CF and GF densities.
- Orthotropic Elasticity:
  - **Assumption 3:** Young's Modulus Z direction is equal to Young's Modulus Y direction.
  - **Assumption 4:** Poisson's ratio is the same in all XY, YZ and XZ planes.
  - **Assumption 5:** Shear modulus is the same in all XY, YZ and XZ planes.
- Orthotropic Stress Limits:
  - **Assumption 6:** Tensile Z direction is equal to Tensile Y direction.

- **Assumption 7:** Compressive Z direction is equal to Compressive Y direction.
- **Assumption 8:** Shear XY, YZ and XZ are all identical.
- Orthotropic Strain Limits:
  - **Assumption 9:** All Orthotropic Strain Limits were calculated using Young’s Modulus equation (Equation 4.1). Where  $E$  is Young’s Modulus in Pa,  $\sigma$  is Tensile Stress in Pa and  $\varepsilon$  is the material strain.

$$E = \frac{\sigma}{\varepsilon} \tag{4.1}$$

**Assumption 1** refers that all five plies of the hybrid material are considered as a single ply, this is, a separation of the plies is no possible due to this acceptance and also thickness does not vary along the laminate. Meanwhile, **Assumption 2** takes into consideration that the hybrid material consists of two plies of CF and three of GF and using the densities of both materials, the density is guessed.

## 4.2 Model configuration description

The blade model was design in SolidWorks and exported as a shell model to be incorporated in ANSYS Workbench. The dimensions of the model are given in Table 4.1.

Table 4.1: Blade model dimensions.

Length	674.27	mm
Width	238.78	mm
Depth	85.65	mm

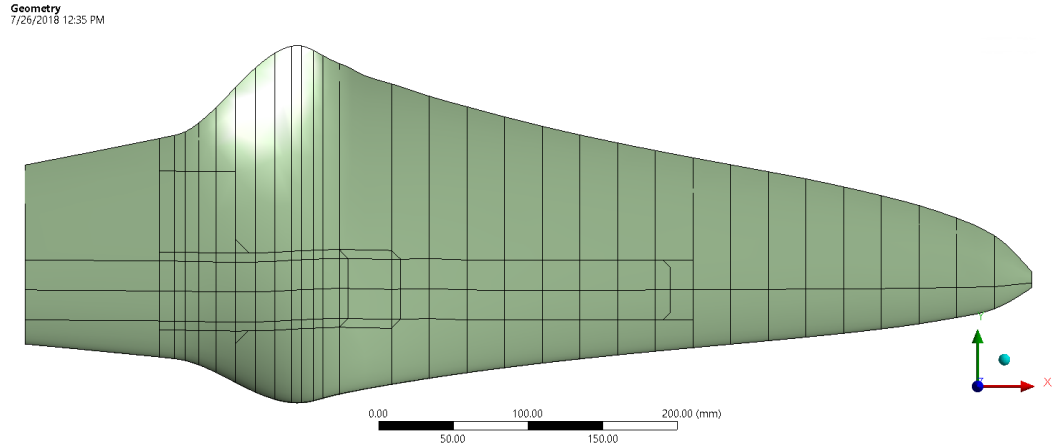


Figure 4.1: Shell blade model divided in 28 sections along its length.

In Figure 4.1 the shell model of the blade is shown and it can be noted that it is divided into 28 sections perpendicular to its length. These sections represent the chord lines of the different hydrofoil sizes and will be used later for the static structural analysis.

### 4.2.1 Meshing

As a first iteration, it was decided that each mesh element should be around 1% of the blade's length, this is, each element should be approximately 6.74 mm size maximum. Shell 181 and Surf 154 were the mesh elements used because they allow displacements and rotations around  $x$ ,  $y$  and  $z$  directions.

Due to the complex geometry of the blade, an edge sizing was applied on the blade's leading edge as shown in Figure 4.2. The element's size was set to 1 mm for this edge and the final mesh can be appreciated on Figure 4.3. A total of 13,297 nodes and 13,573 elements were used.

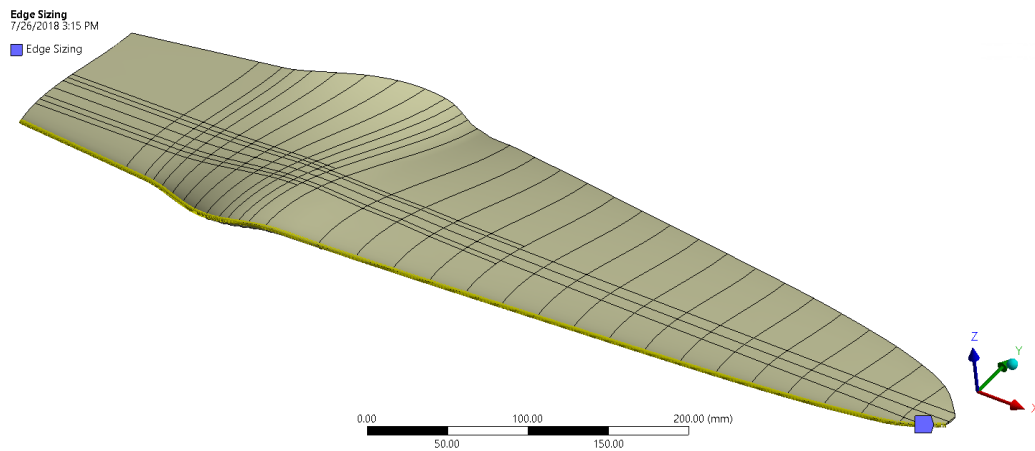


Figure 4.2: Edge meshing applied on the blade's leading edge.

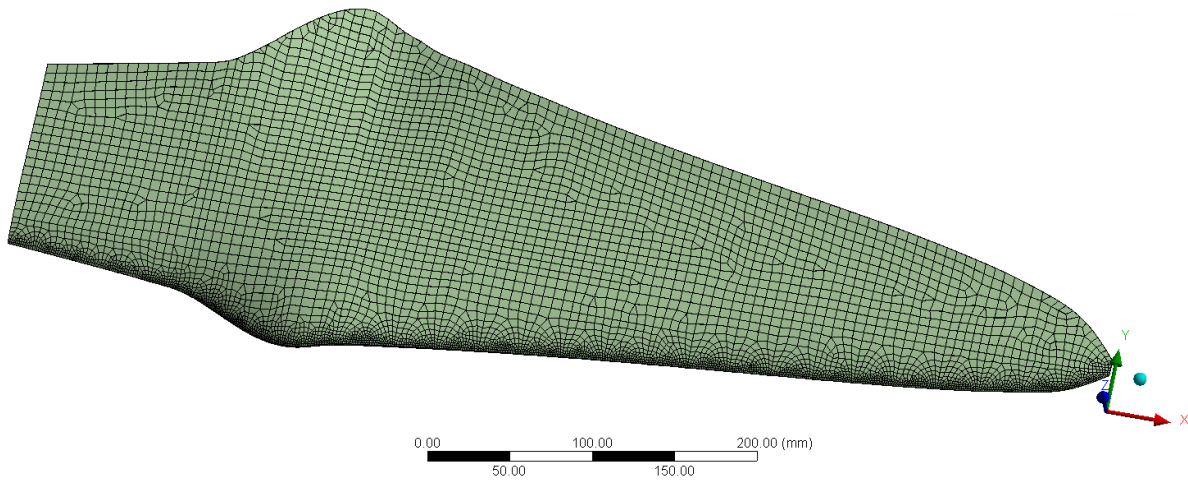


Figure 4.3: Blade model meshing.

## 4.2.2 Named selections

As can be seen in both Figure 4.1 and 4.2, the model is divided into sections that were previously set in SolidWorks. ANSYS Mechanical allows to select and modify user-defined named selections. These selections are needed later on ACP for indicating where to deposit the composite laminae. There are infinite possible combination of named selections but three of them are unlikely to change: the hydrofoil, spar caps and the shear web. The red zone in Figure 4.4 is an example of the named selection for a spar cap.

sparCap\_LP\_1(Blade using hybrid material)  
7/30/2018 8:15 AM  
■ sparCap\_LP\_1(Blade using hybrid material)

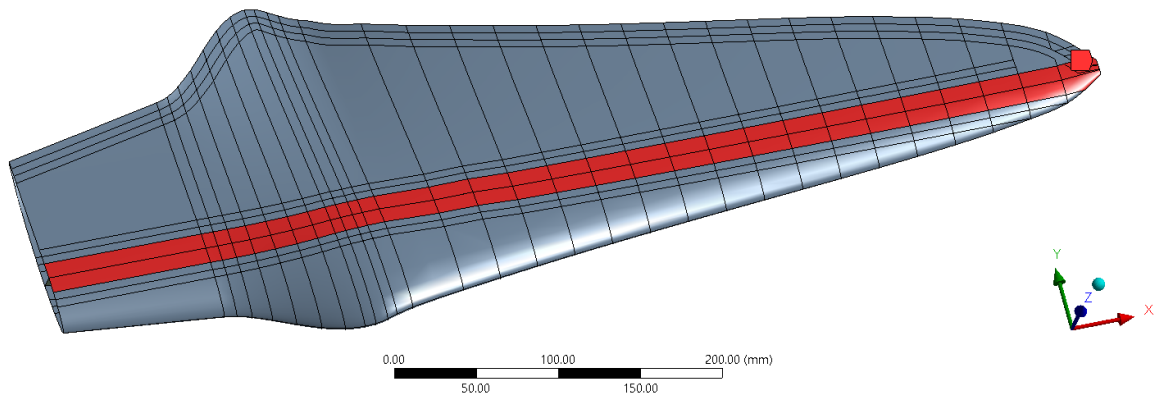


Figure 4.4: Spar cap's named selection example.

### 4.2.3 Model lay-up in ACP

Once meshing and named selections are set, the blade's laminate must be established in ACP. First of all, the materials in Engineering Data of Workbench appear on the field Material Data inside ACP Pre (Figure 4.5). Here, in a subsection named Fabric the user can create fabrics indicating material and thickness of this element. In this case, both GF and Hybrid material should be fixed as fabrics.

Afterwards, Rosettes are indicated (Figure 4.5). Rosettes are coordinate systems that used to set the Reference Direction of Oriented Selection Sets. Rosettes define the  $0^\circ$  direction for the composite lay-up [17].

Then, Oriented Selection Set is applied, which is an Element Set with additional information about the element orientations. The orientation direction of an Element Set is responsible for setting the stacking direction of the associated lay-up.

Finally, in Modeling Groups the stack-ups of composite materials are defined. The software let the user to choose which of the Fabrics defined before is going to use in each ply as well as its orientation. At the end, the model's composite configuration can be observed as the example in Figure 4.6. Material thickness is displayed in Toggle Legend at the left of the model.

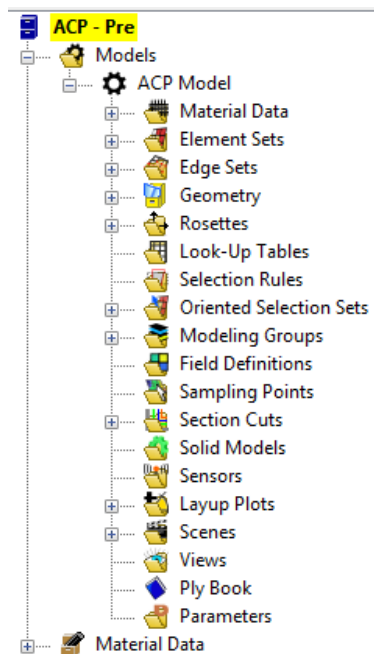


Figure 4.5: ACP Pre tools.

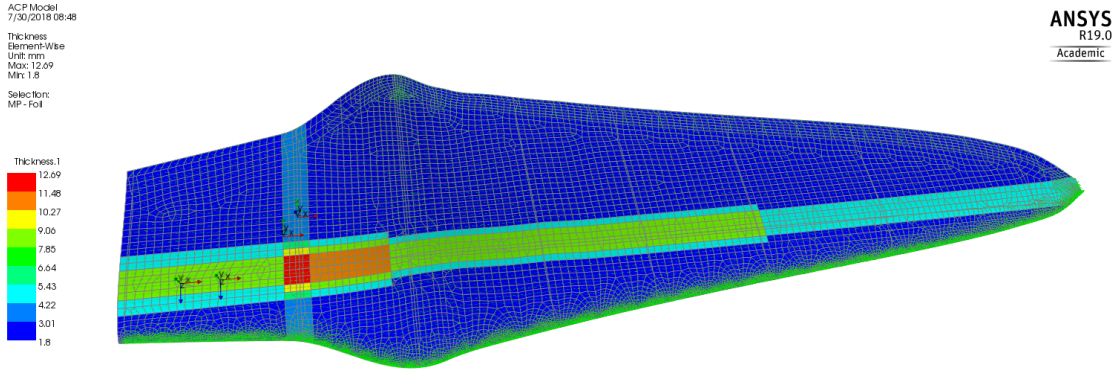


Figure 4.6: Model's lay-up configuration example in ACP.

#### 4.2.4 Boundary conditions

As mentioned in Section 4.2, the blade is divided into 28 sections perpendicular to the blade's length. Ledesma, S. [5] got the forces that are interacting with the blade using Computational Fluid Dynamics (CFD) simulation, a tangential and perpendicular force for each of the sections (see Appendix C). Hence, in total, there are 56 forces being applied on the pressure side of the blade. Furthermore, as in wind turbine blades, this blade is going to be fixed to the generator's shaft by a hub. Therefore, the root of the blade is assumed to have zero displacements and rotations in all directions. The boundary conditions are then configured as in Figure 4.7, the blue section is completely fixed in all directions and forces are applied on the red zones.

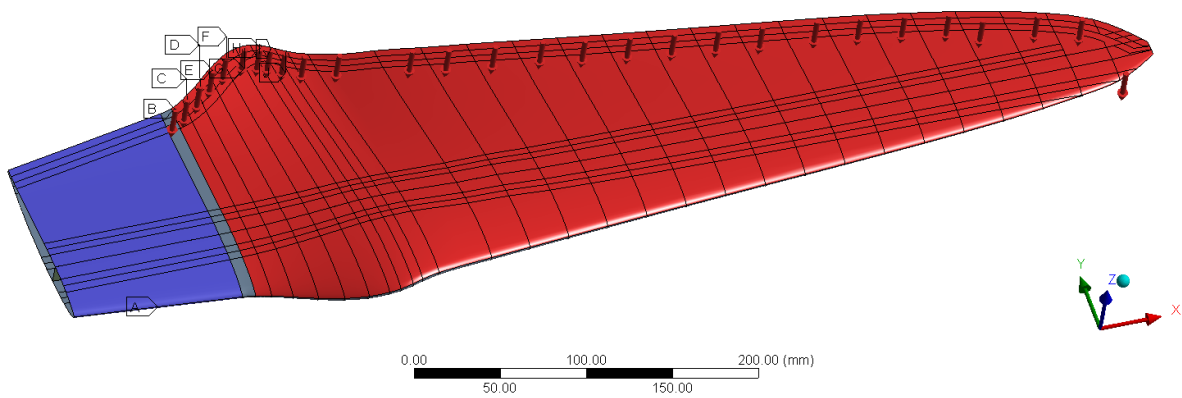


Figure 4.7: Blade's model boundary conditions.



### 4.2.5 Static structural analysis

Just as specified in Figure 1.6, first a static structural analysis is executed. This simulation is performed in the Static Structural block (Figure 3.17). The results are then analyzed in ACP Post and the following points are the ones to be evaluated in order to carry on to the next analysis.

- **Tip displacement:** For this case, it is not a critical design feature, but it is preferred that tip displacement be below 10 % of the blade's length, i.e., less than 67 mm.
- **Stresses:** Even though stresses are important when designing a mechanical structure, in composite materials, these values can not really tell whether there is failure or not. Nevertheless, stresses on the 2 direction should be looked after.
- **Strains:** Same as stresses, it is difficult to conclude that the material has failed just by taking a look at these values, however, strains in the 2 direction of the materials should not be as high as in 1 direction.
- **Failures:** ACP Post allows to define which failure criterion are going to be evaluated. Because of the lack of material data for considering other criterion, Max Stress, Max Strain and Tsai-Hill are the ones taken into account.
- **Mass:** Taking as reference the model made by Espinoza, J. [6], the mass should be reduced. Yet, this step is not very important at this moment until Section 4.2.9.

### 4.2.6 Eigenvalue buckling analysis

Unlike other materials, when a composite material element is under tensile stress, some of its plies might be as well under compressive stress, then, a buckling analysis is needed. Eigenvalue buckling analysis predicts the theoretical buckling strength of an ideal linear elastic structure [17].

Eigenvalue buckling depends on the Static Structural solution, then, it is configured afterwards (Figure 4.8). This simulation works by varying all the values of the boundary conditions until buckling is presented and the multiplier value is displayed. In Analysis Settings, the maximum number of modes to be found can be configured. A total of five buckling modes is chosen because not always is the first mode the lowest value, but one has to compare them all to find it.

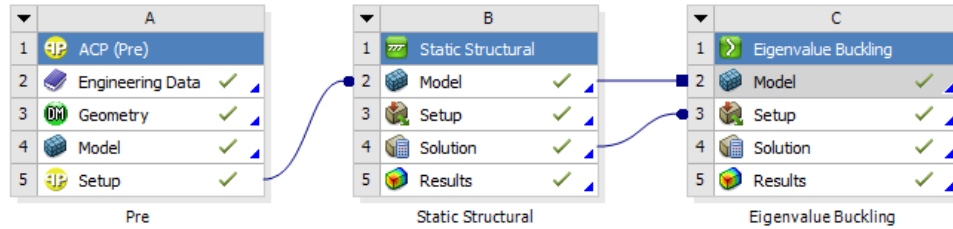


Figure 4.8: Eigenvalue block configuration in ANSYS Workbench.

### 4.2.7 Modal analysis

Like many other design processes, modal analysis is of importance because the structural integrity of the blade is at risk. Working conditions of hydrokinetic blades is approximately of 2 Hz, hence, the first mode shape must be higher than 20 Hz in order to discard failure of the blade.

### 4.2.8 Fabrication validation

In this phase, the composite lay-up is inspected for ensuring the model can be fabricated. For example, if there is an area in which the composite is too thin to make it impossible to built it without damaging the fabric.

### 4.2.9 Optimization process

Once a blade's lay-up has surpassed all the requirements, an optimization process is implemented in an attempt of reducing the mass. A design of experiments will be implemented in the statistical software Minitab. Its response optimizer identifies the combination of input variable settings that optimize a single response or a set of responses. Minitab calculates an optimal solution and draws an optimization plot by mean of regression equations. This interactive plot allows the user to change the input variable settings to perform sensitivity analyses and possibly improve upon the initial solution [18].

Inputs for the optimizer will be defined depending on the observations made as simulations are performed and results obtained.

# Chapter 5

## Results and discussions

### 5.1 Blade model “version 2.0”

In the previous Section 4.2, a general explanation about the different settings and analysis were described. Now the configuration established for a second version of the hydrokinetic blade is presented.

#### 5.1.1 Blade’s composite lay-up and Static Structural simulation

In this section, each of the named selections and its corresponding composite lay-up setup made in ACP is described.

##### 5.1.1.1 Hydrofoil

Figure 5.1 depicts that the whole hydrofoil was selected as a named selection. GF was chosen as proper material using a triaxial (or just TRIAX) setup, i.e., three plies of UD GF with a stack-up sequence of [0/45/-45] because this material is less thick than the hybrid.

Afterwards, the Static Structural simulation takes place using the boundary conditions described and shown in Section 4.2.4. The results for tip displacement, maximum stresses and strains, and failure criterion evaluations are depicted on Figures 5.2, 5.3 and 5.4, respectively.

Figure 5.2 shows the maximum displacement using the configuration mentioned before on this Section the tip displacement is 94.747 mm. This value is greater than 10 % of the blade’s length and it is enough for implementing spar caps as a next step. However, the results of stresses, strains and failure criterion give us information about where the blade needs reinforcements. Just by taking a look at Figures 5.3 and 5.4 it becomes obvious that there is a stress concentration at the root of the blade and thus, it is causing GF to fail. As a further comparison point, Table 5.1 summarized all these results.

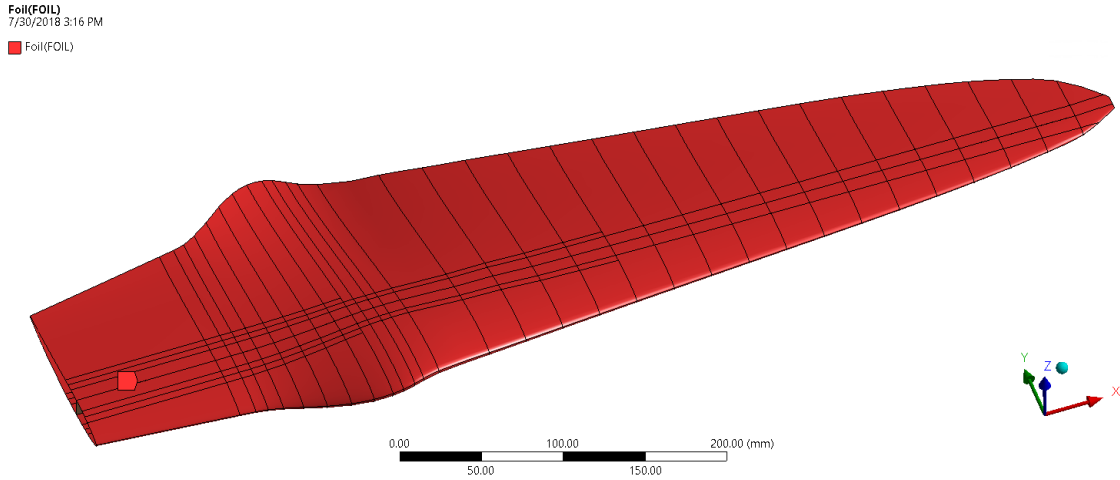


Figure 5.1: Hydrofoil named selection for blade “version 2.0”.

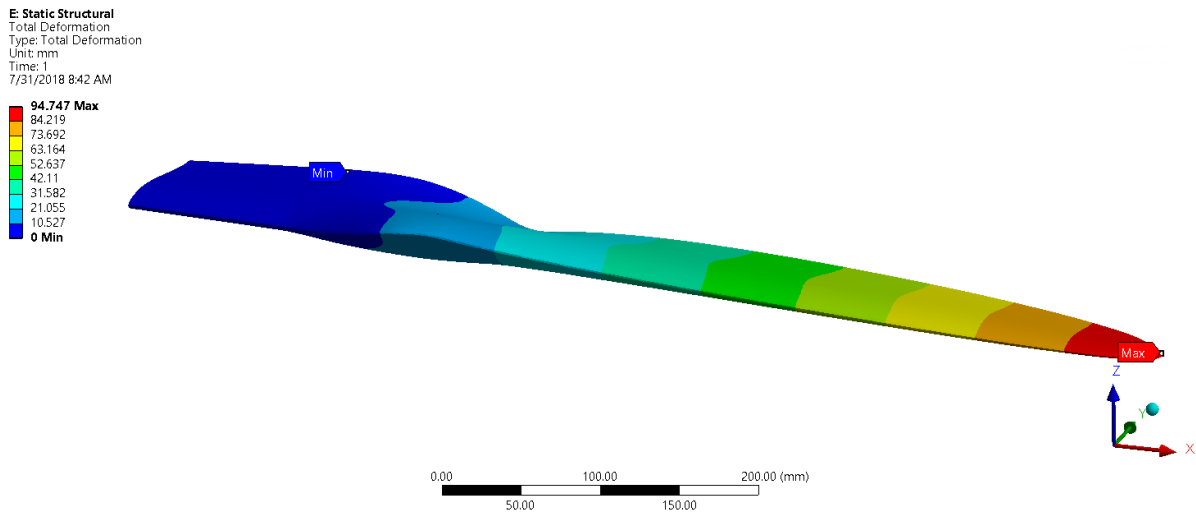


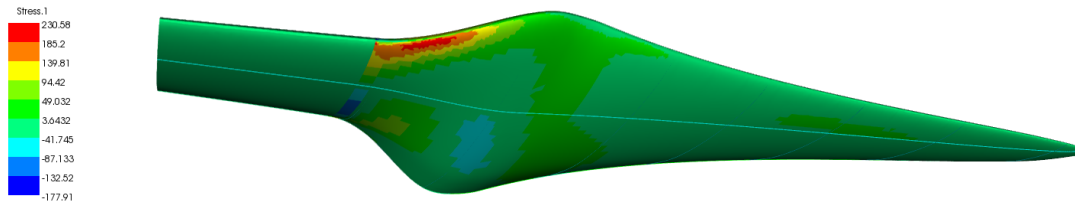
Figure 5.2: Total tip displacement result using only hydrofoil for blade “version 2.0”.

Table 5.1: Results of the Static Structural simulation using only hydrofoil.

Results	Value	Units/Criteria
Tip displacement	94.747	mm
Max. Stress (Tensile)	230.58	MPa
Max. Stress (Compressive)	177.91	MPa
Max: Strain	0.018665	mm/mm
Max. Failure index	8.0117	Max. Strain

ACP Model  
7/31/2018 08:43  
Stress - e2 - bo1  
Element: Wire  
Unit: MPa  
Set: 1 - Time/Freq: 1.0 (Last)  
Max: 230.58  
Min: -177.91

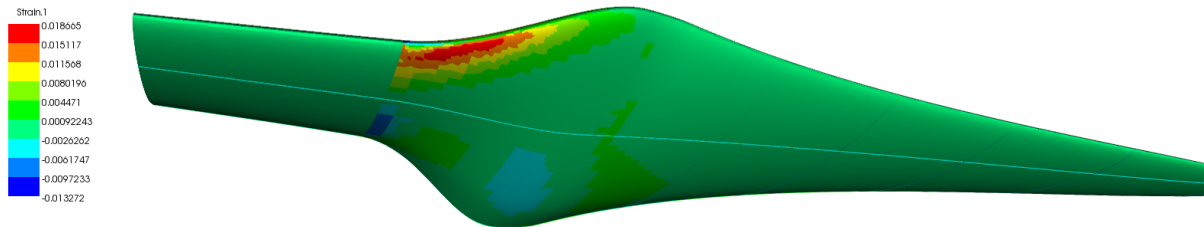
ANSYS  
R19.0  
Academic



(a) Stresses on the 2 direction material.

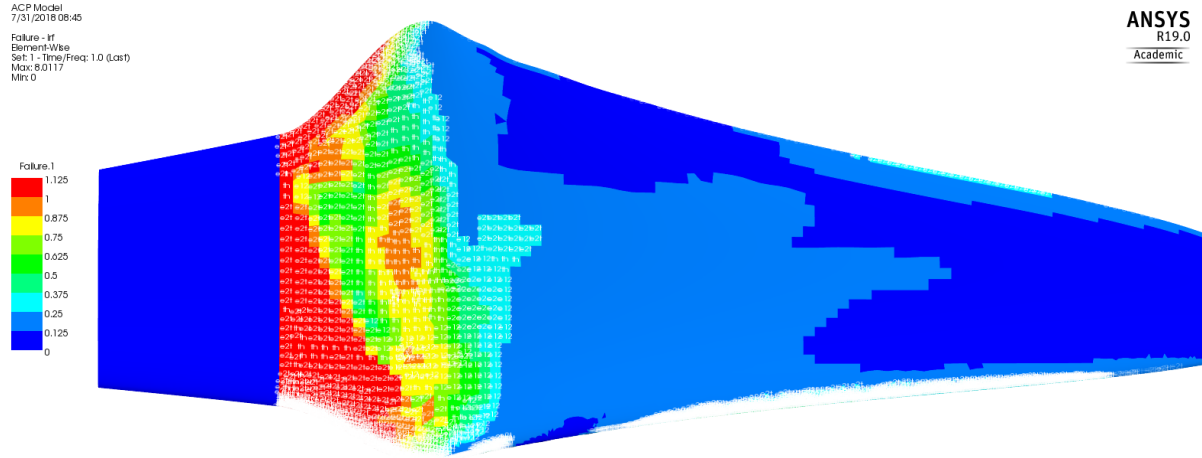
ACP Model  
7/31/2018 08:44  
Strain - e2 - bo1  
Element: Wire  
Set: 1 - Time/Freq: 1.0 (Last)  
Max: 0.018065  
Min: -0.013272

ANSYS  
R19.0  
Academic

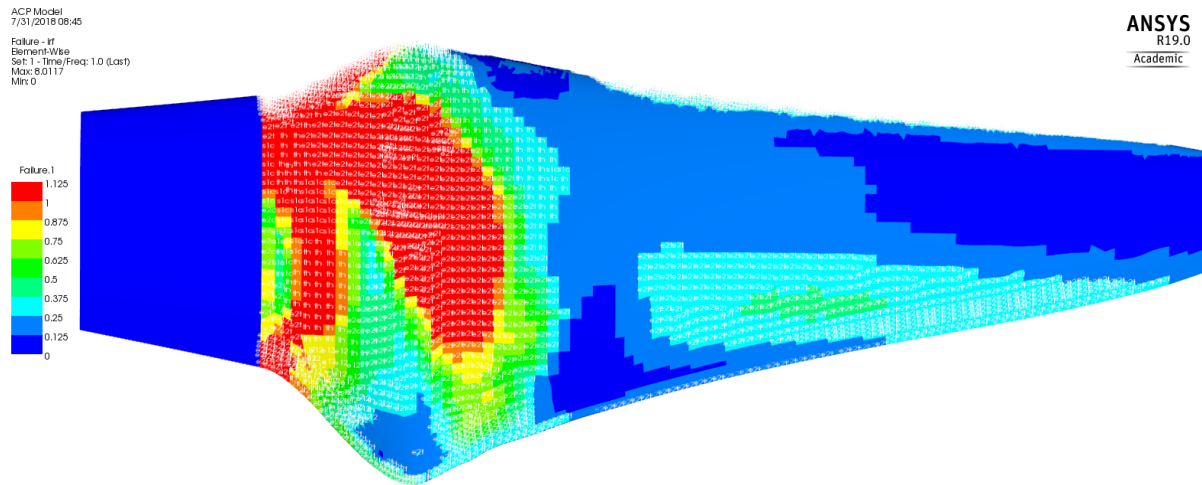


(b) Strains on the 2 direction material.

Figure 5.3: Stresses and strains on the 2 direction results using only hydrofoil for blade “version 2.0”.



(a) Failure criterion on the pressure side of the blade.



(b) Failure criterion on the suction side of the blade.

Figure 5.4: Failure criterion results for hydrofoil blade “version 2.0”.

### 5.1.1.2 Spar caps

Since using just hydrofoil did not work, the implementation of spar caps is necessary in both pressure and suction side of the blade. Hybrid material is now introduced into the model. It was chosen to employ it along the whole length of the blade using an orientation of  $0^\circ$ , with a width of 20 mm (Figure 5.5), the same as Espinoza, J. [6] for reference.

Results of the Static Structural simulation can be seen in Table 5.2. As it can be noted, generally all the values lowered around 40 % compared with results on Table 5.1. Tip displacement is already below 10 % of the blade’s length. Nonetheless, Maximum Strain Criteria value is greater than 1 by far. Figures 5.6 (a) and (b) depict that fiber failure still occurs on the blade’s root. Therefore, the next step is to incorporate a Shear Web for trying to eliminate fiber failure.

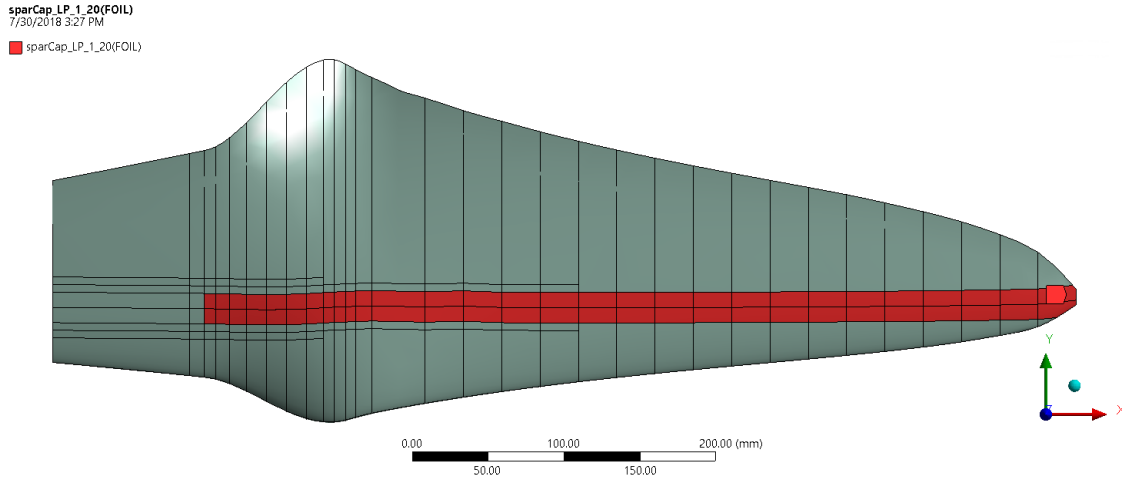
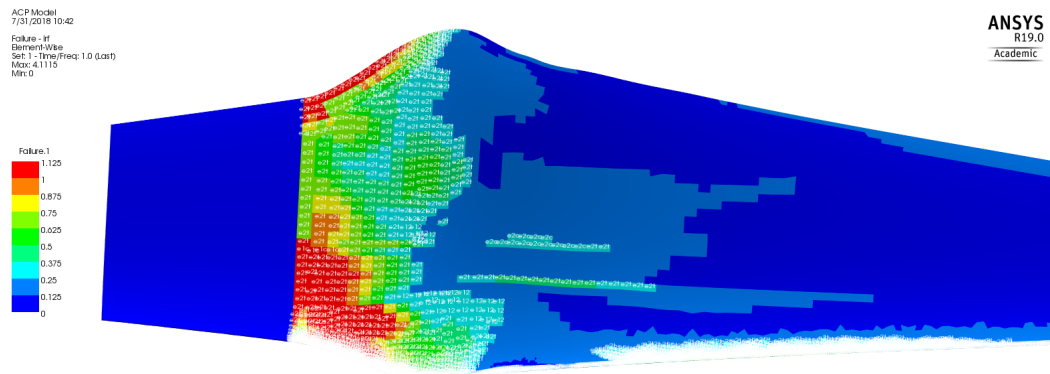
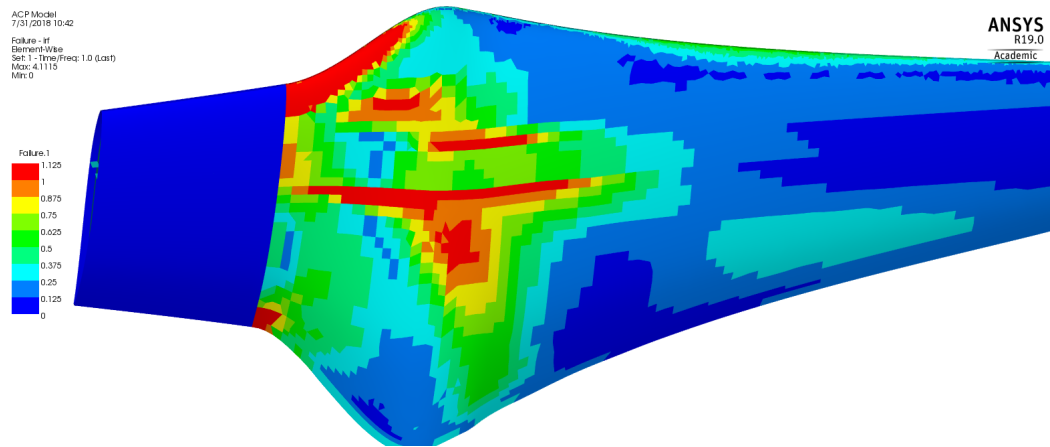


Figure 5.5: Spar caps along the whole length of the blade with a width of 20 mm in both pressure and suction sides.



(a) Failure criterion results in pressure side.



(b) Failure criterion results in suction side.

Figure 5.6: Failure criterion results for blade “version 2.0” using spar caps.

Table 5.2: Results of the Static Structural simulation using Spar Caps.

Results	Value	Units/Criteria
Tip displacement	53.061	mm
Max. Stress (Tensile)	160.66	MPa
Max. Stress (Compressive)	113	MPa
Max: Strain	0.010927	mm/mm
Max. Failure index	4.1115	Max. Strain

### 5.1.1.3 Shear Web

Shear web material selection is UD GF with an stack sequence of  $[(\pm 45)/0/(\pm 45)]_s$  and its named selection is displayed as a red zone in Figure 5.7. The location of the shear web along each of the hydrofoil chords is around 30 % of its length.

The simulations results for this configuration are listed on Table 5.3. It can be seen that the tip displacement, maximum stresses and strains decreased significantly but Max Strain criteria is still greater than 1. Hence, more modifications have to be made to the model in order to reduce this value.

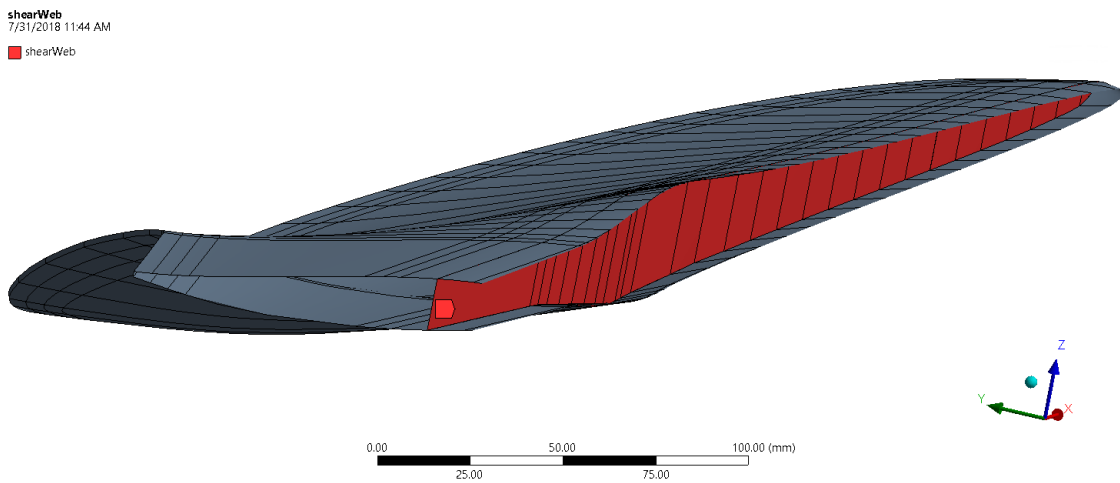


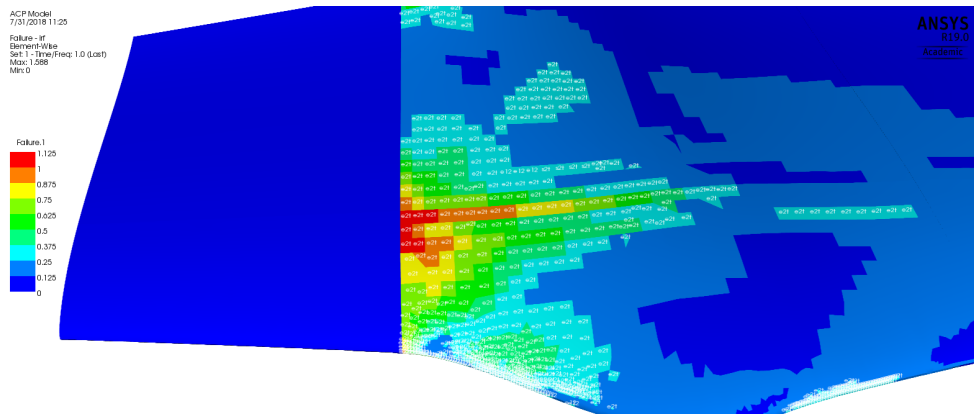
Figure 5.7: Shear web named selection.



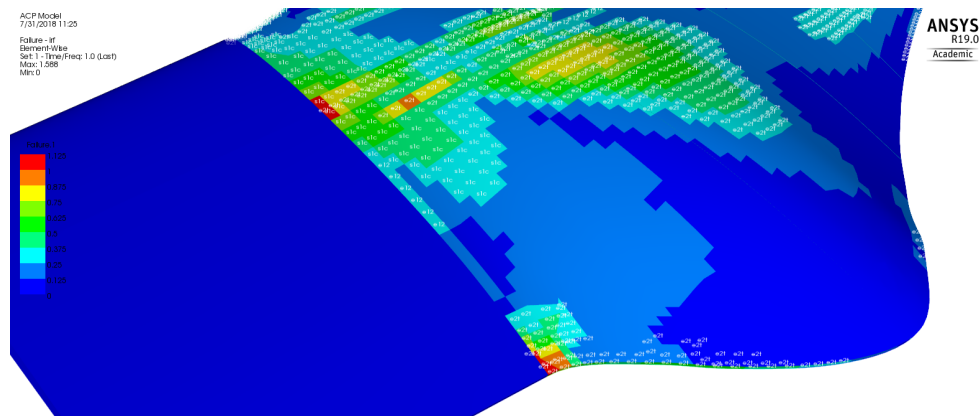
Table 5.3: Results of the Static Structural simulation using Shear Web.

Results	Value	Units/Criteria
Tip displacement	24.981	mm
Max. Stress (Tensile)	60.251	MPa
Max. Stress (Compressive)	37.815	MPa
Max: Strain	0.0046189	mm/mm
Max. Failure index	1.588	Max. Strain

Furthermore, Figure 5.9 shows that the maximum failure value is found in the shear web, specifically, on the same region where failures are located on the hydrofoil, shown in Figures 5.8 (a) and (b). Besides, geometrically speaking, there is a change of sizes on this zone resulting in a large stress and strain concentrations. Thus, new named selections and changes of composite lay-ups have to be made in order to fulfill structural requirements.



(a) Failure criterion results on pressure side of the blade.



(b) Failure criterion results on suction side of the blade.

Figure 5.8: Failure criterion simulation results for blade “version 2.0”.

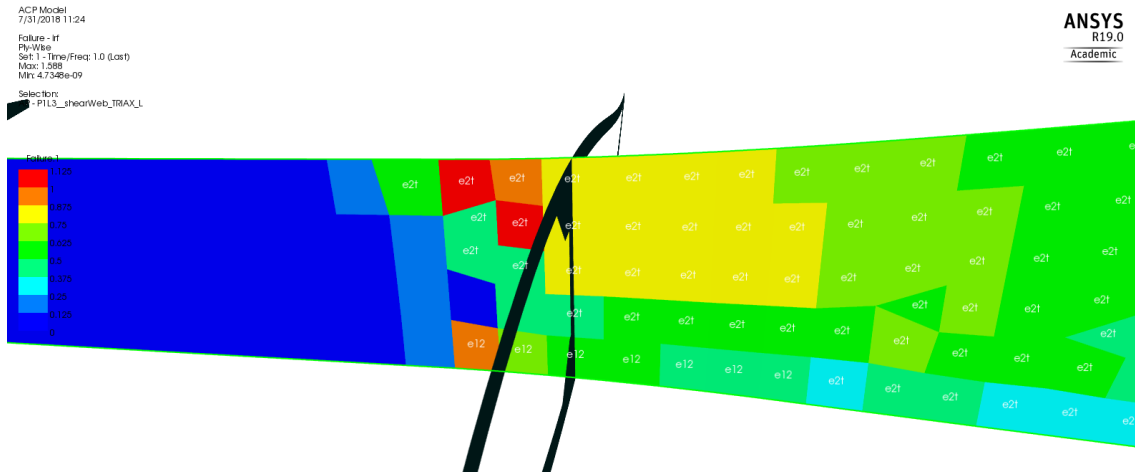


Figure 5.9: Failure on the 2 direction of the fiber located in the shear web.

## 5.2 Blade “version 2.1”

Some modifications in the mesh and named selections were made in order to prevent fiber failure as in the last configuration.

### 5.2.1 Meshing

The mesh made on Section 4.2.1 was completely refined because results were being affected. ANSYS Workbench was then configured to refine the mesh until results converged in a variation of less than 0.1 %. Afterwards, total of 70,606 nodes and 71,664 elements are used. This meshing will be used from now on, including for other types of analysis.

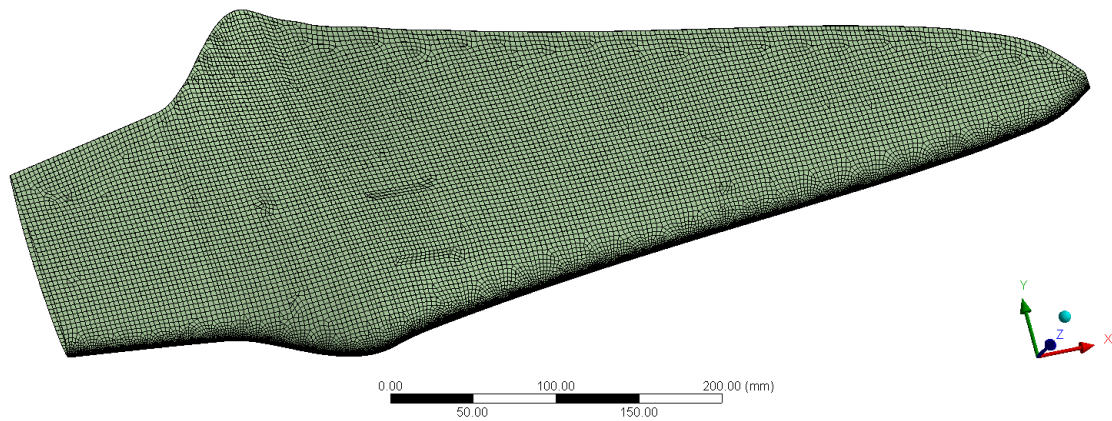
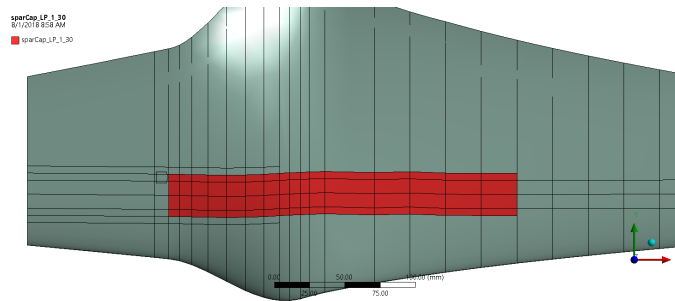


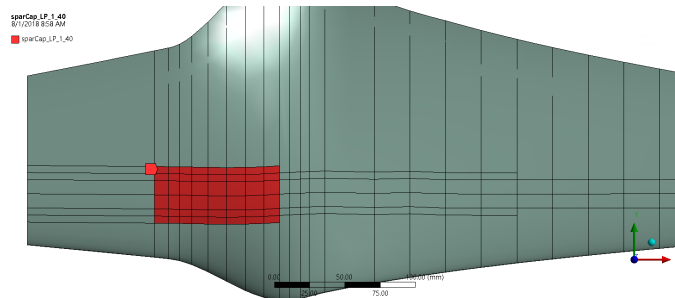
Figure 5.10: Refined blade’s meshing.

## 5.2.2 Named selections

New named selections had to be made in order to avoid fiber failure as mentioned before. Hydrofoil, spar cap, and shear web remained the same as in Figures 5.1, 5.5 and 5.7, respectively. First of all, two more reinforcements were made in the spar caps as shown in Figures 5.11 (a) and (b).



(a) Spar cap reinforcement with 212 mm length and 30 mm width.



(b) Spar cap reinforcement with 85 mm length and 40 mm width.

Figure 5.11: Spar caps reinforcement for blade “version 2.0”.

As in Section 5.1.1.2, these spar caps are placed in both pressure and suction sides of the blade using the Hybrid composite material with an orientation of  $0^\circ$  along the blade’s length.

Also, as it was seen in Figures 5.8 (a) and (b), the change of geometry in the root of the blade is causing stress and strain concentrations. Then, an extra support is added so failure could be avoided as depicted in Figure 5.12. The support is made of GF with a stack-up configuration of  $[0/45/-45]$ .

Moreover, since the shear web was only 6 mm thick, it was creating shear stresses on pressure side spar cap. Consequently, Polyvinyl Chloride (PVC) Foam is set at the symmetry axis of this element, as sketched on Figure 5.13, in order to increase its thickness without a great weight gain.

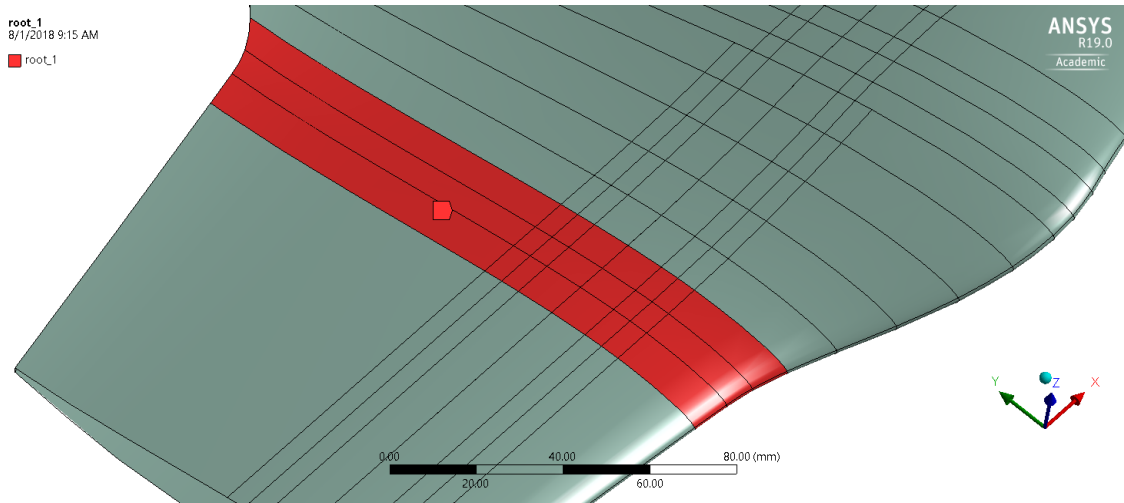


Figure 5.12: Root named selection reinforcement zone.

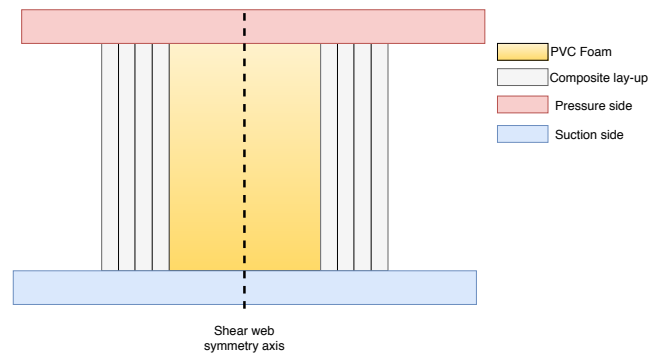


Figure 5.13: Shear web lay-up sketch.

### 5.2.3 Static Structural results and conclusions

The composite lay-up of blade “version 2.1” is illustrated on Figure 5.14 and the Static Structural simulation results are listed on Table 5.4. Maximum Strain criteria is already less than 1 and the values of tip displacement, maximum tensile, compressive and strain are the lowest. These results may be enough for concluding this work, however, the red zone on Figure 5.14 indicates a thickness of 12.69 mm on each side of the blade, i.e., 25.38 mm thick in total.

By measuring the model at this area, there is a space of 17.22 mm between the pressure and suction side of the blade. This means that ANSYS Mechanical has taken into account material that in reality cannot exist, besides, shear web is also considered in this space, which makes these results even more fictional. Therefore, this configuration is completely rejected without carrying out other analysis because the blade is physically impossible to manufacture.

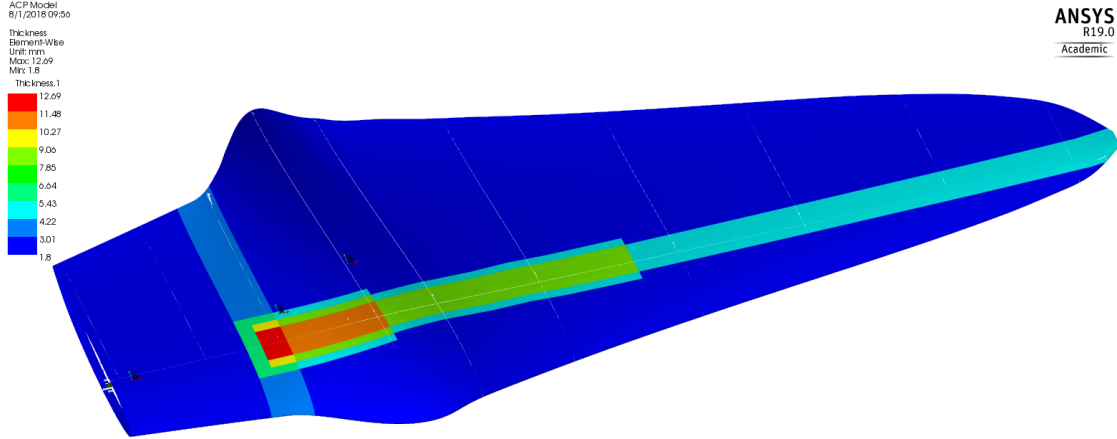


Figure 5.14: Blade lay-up “version 2.1”.

Table 5.4: Static Structural simulation results for blade “version 2.1”.

Results	Value	Units/Criteria
Tip displacement	18.761	mm
Max. Stress (Tensile)	32.921	MPa
Max. Stress (Compressive)	22.579	MPa
Max: Strain	0.0023419	mm/mm
Max. Failure index	0.87926	Max. Strain

### 5.3 Blade model “version 3.0”

A redesign of the blade “version 2.1” described on Section 5.1 has to be made. The high stress and strain concentrations led to exceed the physical space inside the blade and now is to be corrected.

#### 5.3.1 Blade’s lay-up and named selections

Being aware about the space problem, it is necessary to change the material distribution inside the blade without threatening its structural behavior, thus, the coming up changes are made. GF with a stack sequence of  $[0/45/-45]$  is still being used as hydrofoil material.

##### 5.3.1.1 Spar caps

In an attempt to keep fiber failure below 1, width of the spar caps is extended to 30 mm from the root of the blade to 390 mm length, afterwards, width is reduced again to 20 mm up to the tip (Figure 5.15) because much lower forces interact in that region compared to the root.

Furthermore, additional hybrid composite reinforcements are needed for the spar cap in Figure 5.15 at the root of the blade due to stress and strains concentrations found in previous sections. Figures 5.16 (a) and (b) depict these supplementary supports, the one on suction side is larger than the one on pressure side because of the blade's geometry, even higher stresses and strains concentrations occur on this face.

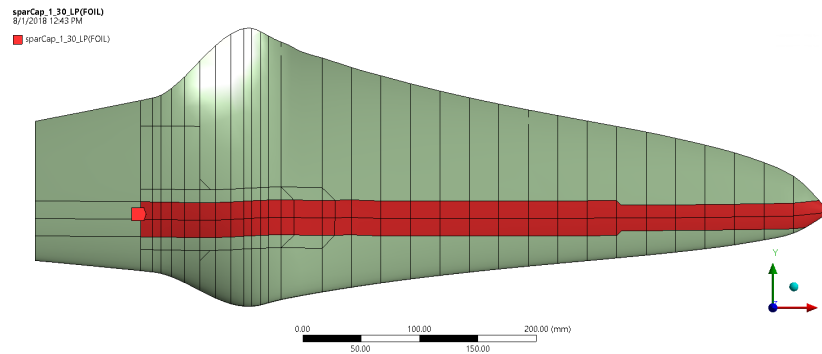
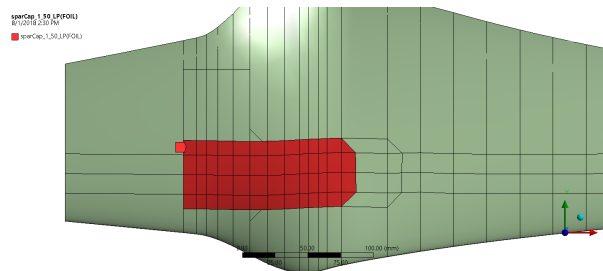
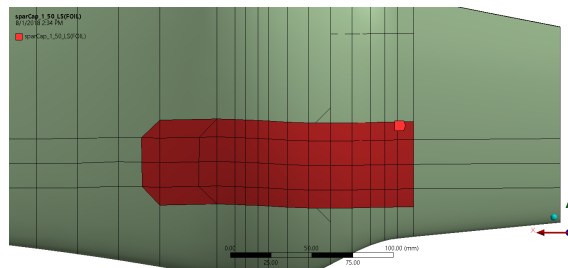


Figure 5.15: Hybrid material spar caps along the blade's length and 30 mm and 20 mm width reduction at the tip.



(a) Pressure side reinforcement with 127 mm length and 50 mm width.



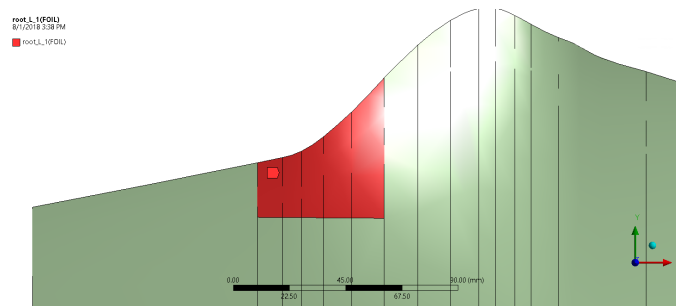
(b) Suction side reinforcement with 162 mm length and 50 mm width.

Figure 5.16: Hybrid material reinforcements in pressure and suction side of the blade.

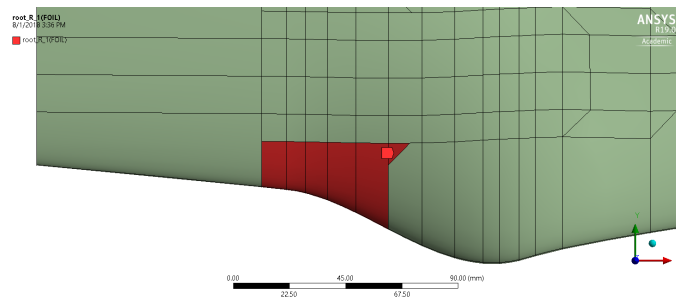
### 5.3.1.2 Root reinforcements

The main challenge due to blade's geometry is the stress concentrations at its root. It creates the need of additional supports as shown in Figure 5.12. The problem with this named selection is the additional material placed on the spar cap's zone. Thus, this reinforcement is split in left and right root as depicted in Figures 5.17 (a) and (b). GF is used for these two sections using a stack sequence of [30/0/30].

Additional to these side-reinforcements, one more support is added in each side of the blade as displayed in Figure 5.18. The goal of this support is to relief stress and strain concentrations on the spar caps next to it. One layer of hybrid material with an orientation of  $0^\circ$  was selected for this application.



(a) Left root reinforcement on both pressure and suction sides.



(b) Right root reinforcement on both pressure and suction sides.

Figure 5.17: GF side root reinforcements named selections.

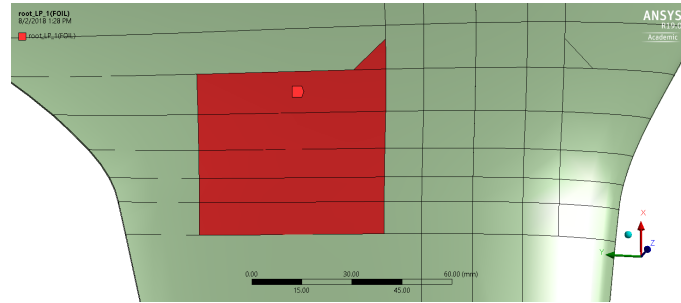


Figure 5.18: Additional hybrid material root support on each side of the blade with 72 mm length.

### 5.3.1.3 Shear web

Shear web's named selection was also modified. Its area has been reduced in order to avoid ANSYS Mechanical to consider fictional material as depicted in Figure 5.19. The chosen material is GF using a stacking sequence of  $[(\mp 45)_2/\text{Foam}/(\mp 45)_2]$  as illustrated before in Figure 5.13 with a total of 10.8 mm thickness.

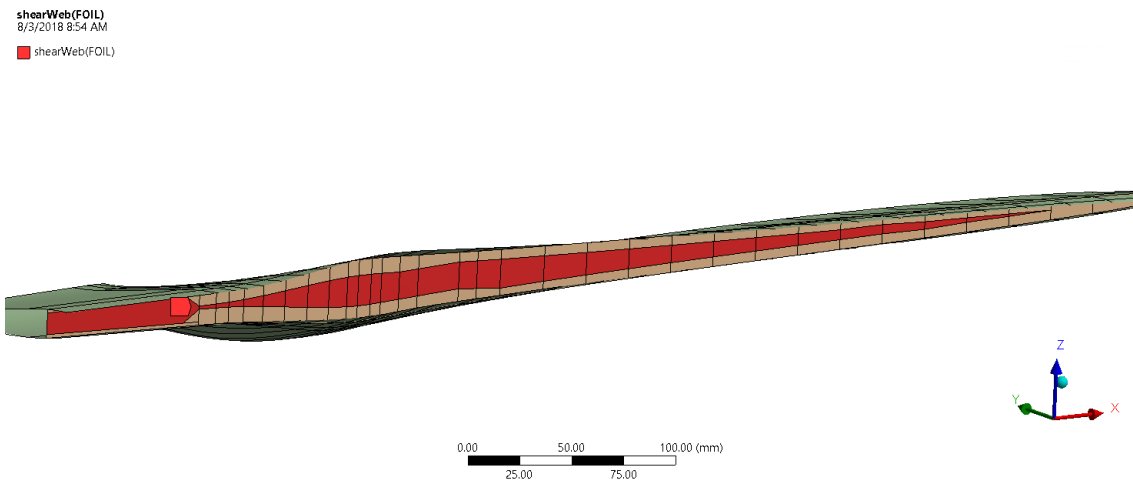


Figure 5.19: Shear web's named selection for blade "version 3.0".

### 5.3.1.4 Blade's "version 3.0" lay-up

Once all named selections have been described, the complete blade's lay-up can be appreciated in Figure 5.20. The yellow zone at the blade's root is 7.8 mm thick, and a total of 15.6 mm thick considering both pressure and suction side of the blade. As the internal space in that zone is 17.22 mm, there are still 1.62 mm left. It will be difficult to fabricate a shear web between both



spar caps in that space left, then, when fabricated, there will not be shear web at the root of the blade.

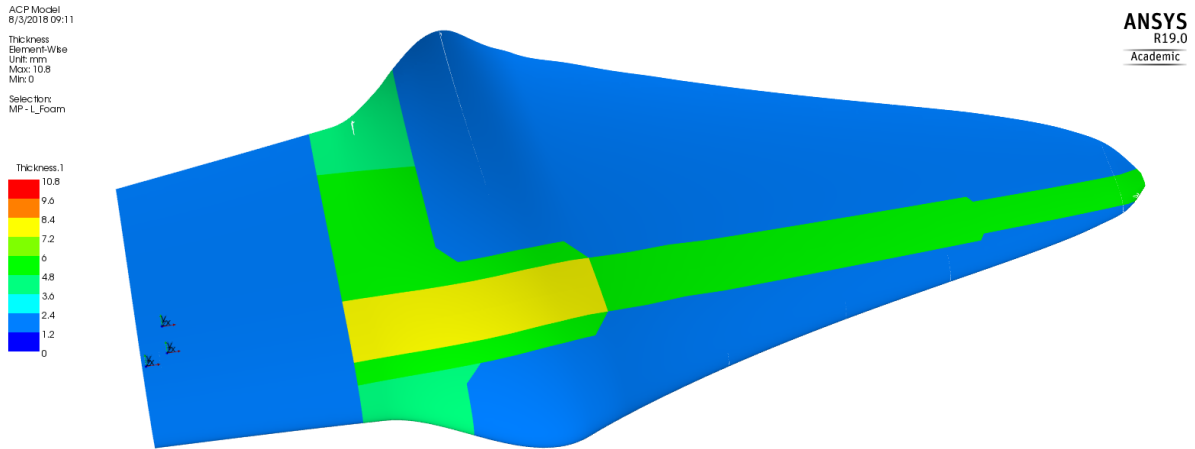


Figure 5.20: Blade “version 3.0” composite lay-up setup.

### 5.3.2 Static Structural simulation results

Boundary conditions remain unchanged as in Section 4.2.4. Table 5.5 shows the Static Structural simulations results. When compared with results in Table 5.4, tip displacement has increased around 25.83 %, still this value is below 10 % the blade’s length. Figure 5.21 details displacement results, the color code in this figure tell us that there is rotation of the blade causing an increase in compressive stress and strain in the 2 direction of the composite material in the suction side as depicted on Figures 5.22(b) and 5.23(b).

Table 5.5: Static Structural simulation results for blade “version 3.0”.

Results	Value	Units/Criteria
Tip displacement	25.295	mm
Max. Stress (Tensile)	29.83	MPa
Max. Stress (Compressive)	41.32	MPa
Max: Strain	0.0033354	mm/mm
Max. Failure index	0.87297	Max. Strain

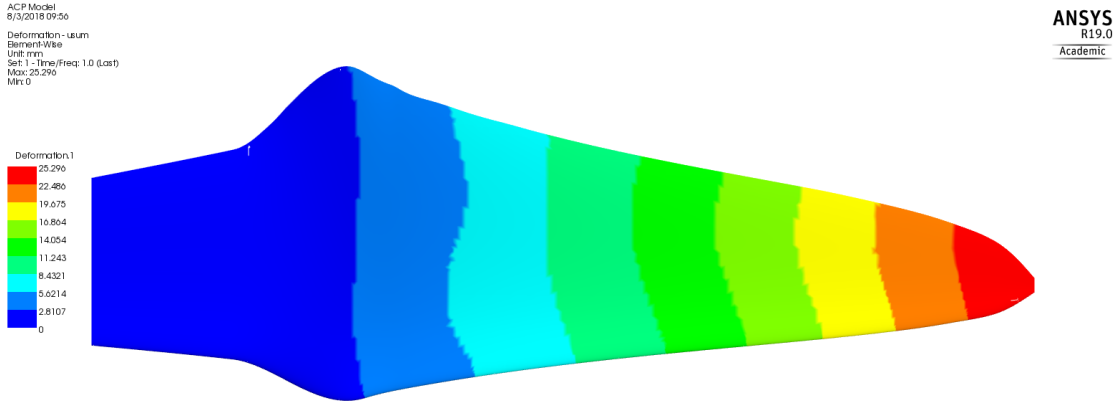
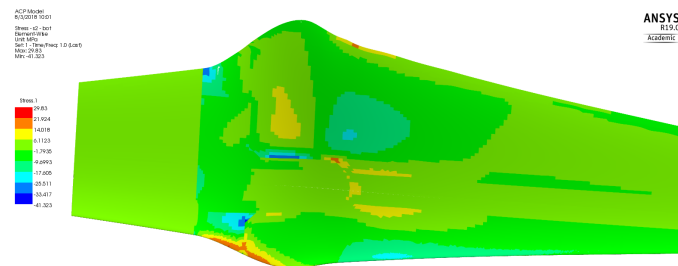


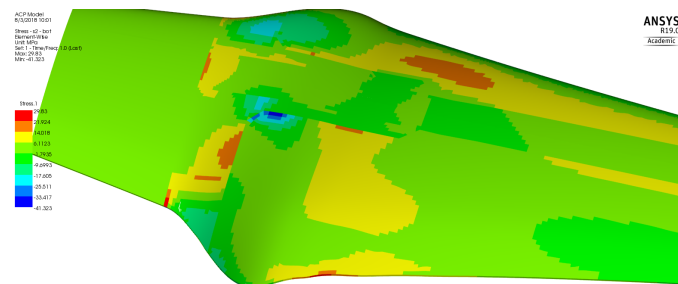
Figure 5.21: Displacement results of blade “version 3.0”.

On the other hand, Maximum Strain Criteria gives a value of 0.87297 on the pressure side of the blade (Figure 5.24), and there is around 0.7 % of difference between “version 2.0”, yet, it is less than 1 and represents no threat to fibers.

Since all static structural requirements have been surpass, the model will be test for buckling analysis.

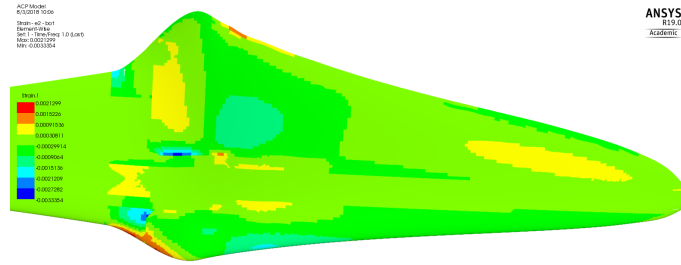


(a) Stresses on pressure side.

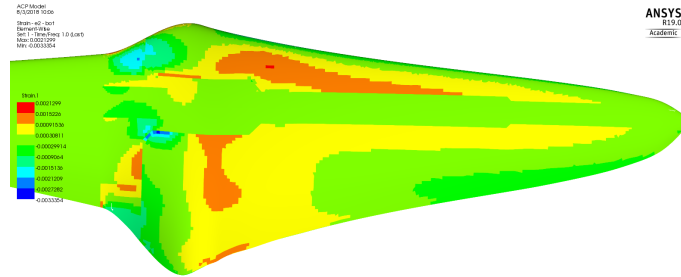


(b) Stresses on suction side.

Figure 5.22: Stress distribution results in the 2 direction in both sides of the blade “version 3.0”.



(a) Strains on pressure side.



(b) Strains on suction side.

Figure 5.23: Strain distribution results in the 2 direction in both sides of the blade “version 3.0”.

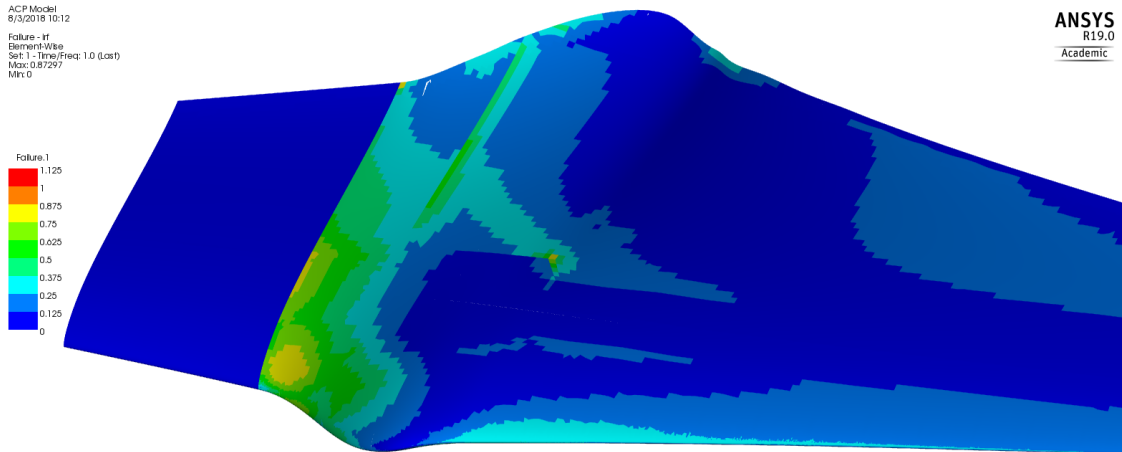


Figure 5.24: Maximum Strain Criteria value distribution on pressure side of the blade.

### 5.3.3 Eigenvalue buckling analysis

As mention before in Figure 4.8 on Section 4.2.6, eigenvalue buckling analysis simulations depends on the static structural simulation results. In this block, the number of modes to be found is selected. Since five modes were picked, Table 5.6 presents the load multipliers for each mode.

Table 5.6: Eigenvalue buckling simulation results for blade “version 3.0”.

Mode	Load multiplier	Total displacement (mm)
1	-3.407	1.0997
2	-2.6535	1.0561
3	-2.2192	1.084
4	3.1056	1.0289
5	3.2837	1.0493

ANSYS Help [17] declares that load multipliers are absolute magnitudes and if some have a negative sign, it just indicates the direction of the forces applied in the boundary conditions. Then, it can be noticed that Mode 3 is the lowest with a total displacement of 1.084 mm as can be seen in Figure 5.25. This means than the blade can withstand more than twice of the load before buckling is presented. Thus, modal analysis is the following step.

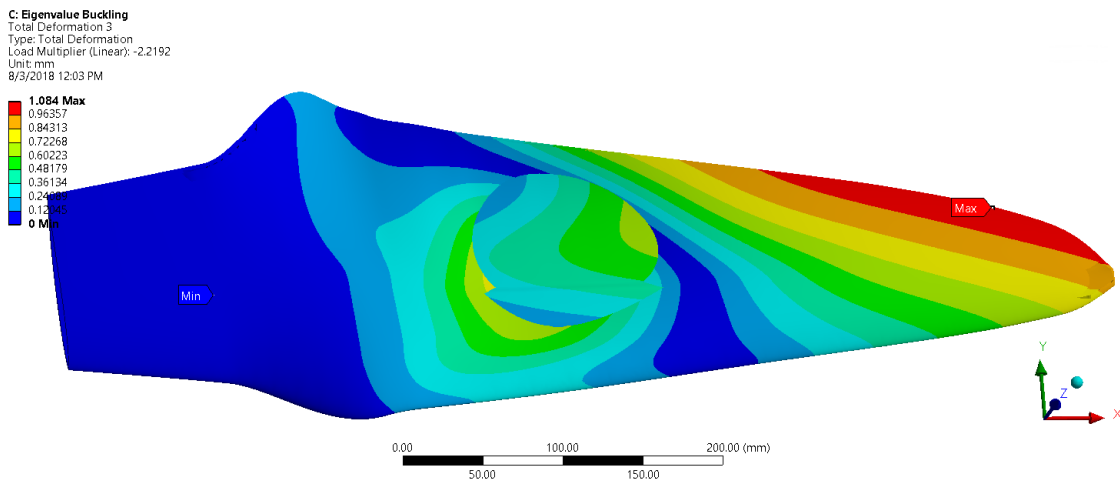


Figure 5.25: Eigenvalue buckling analysis results for mode 3.

### 5.3.4 Modal analysis simulation

Results for this analysis are shown in Table 5.7. The very first modal is of interest and as it can be viewed from this table, its value is 53.384 Hz which surpass the safety margin of the blade working conditions. Figure 5.26 shows the behavior of the blade at the first modal, in which the tip of the blade deflects 83.384 mm upwards and downwards.

Table 5.7: Modal simulation results for blade “version 3.0”.

Mode	Frequency (Hz)	Total displacement (mm)
1	53.384	83.394
2	78.636	741.86
3	146.08	1206.6
4	158.43	109.4
5	204.13	177.59

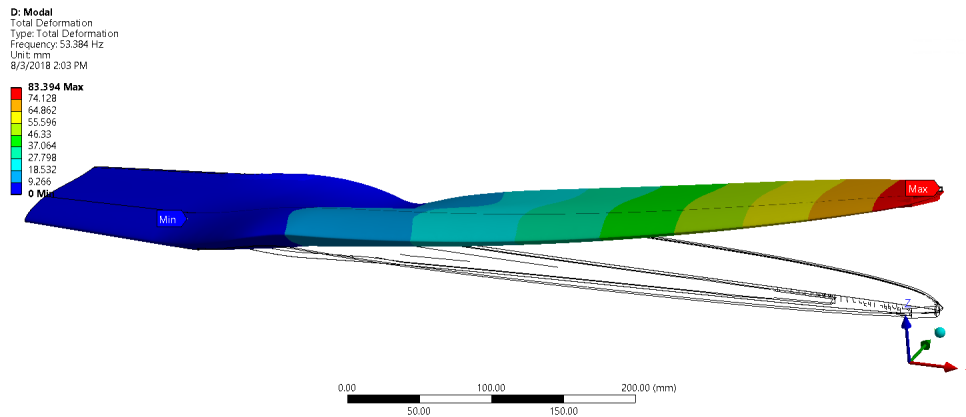


Figure 5.26: First mode of blade “version 3.0” with a frequency of 53.384 Hz.

### 5.3.5 Mass optimization

As seen so far, turbine blades consist of three main structural components: foil, spar caps, and shear web. In this case, the hydrofoil consist of GF in a TRIAX configuration in order to withstand external forces beyond operating conditions. For example, when being fabricated, transported or installed. Thus, this component cannot be taken into account for mass reduction.

On the other hand, when comparing the mass impact of both shear web and spar cap, it becomes clear that spar caps add much more weight due to density and volume of the hybrid material in the blade. Then, the components to be optimize are the spar caps.

#### 5.3.5.1 Design of experiments

Since optimized dimensions for the spar cap are desired, a Design of Experiments (DOE) is used. Seeing that thickness of the hybrid material cannot be changed due to **Assumption 1**, experiments with length and width are considered. A total of nine cases are proposed, a combination of three lengths and three widths as shown in Table 5.8. Length is taken from the root of the blade as shown in Figure 5.27.

Table 5.8: Experiment with dimensions of spar caps.

Length\Width	40 mm	50 mm	60 mm
185.55 mm	A1	A2	A3
429.775 mm	B1	B2	B3
674 mm	C1	C2	C3

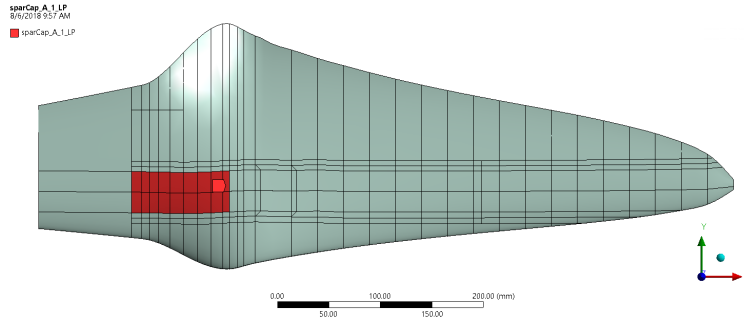


Figure 5.27: Spar cap of 185.55 mm length and 40 mm width.

The objective of these nine cases is to retrieve the values of maximum displacement, maximum failure factor and mass of each of them. Afterwards, the information is then fill in on Minitab. Results of all nine simulations can be seen in Table 5.9. Considering other results instead of just mass helps keeping the structural resistance obtained from blade “version 3.0” in Section 5.3. After introducing these results, response surfaces are created.

Table 5.9: Simulation results input for the DOE.

Element	Max. displacement (mm)	Max. Failure index	Mass (kg)
A1	34.121	1.3476	0.928
A2	33.578	1.3185	0.939
A3	33.24	1.3193	0.951
B1	25.31	0.77528	1.079
B2	24.025	0.7598	1.130
B3	23.065	0.75545	1.181
C1	23.161	0.80083	1.217
C2	21.498	0.76012	1.304
C3	20.312	0.75477	1.385

### 5.3.5.2 Response surface regression: Displacement versus length, width

As a first step, a surface response is made evaluating displacement versus length, width and its regression equation is the following:

$$d = 46.351 - 0.06604L - 0.0130W + 0.000060L^2 - 0.000201L * W \quad (5.1)$$

where  $d$  is displacement,  $L$  length and  $W$  width. Moreover, Figure 5.28 displays its contour plot. One can find that the minimum tip displacement will occur when the spar caps are the longest and widest. However, displacement is not a fundamental design priority in this work, then, failure and mass are also evaluated.

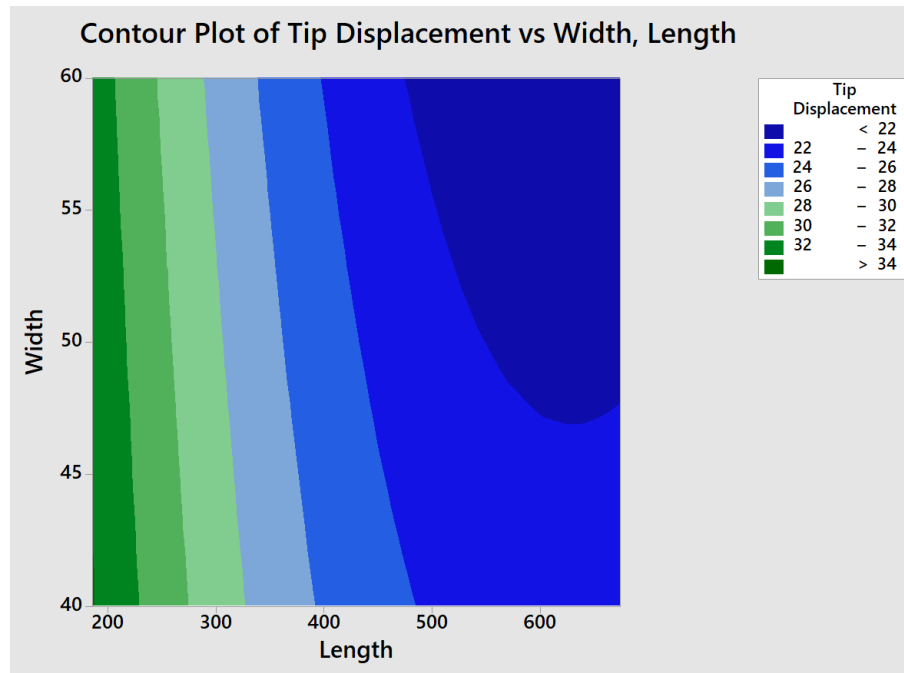


Figure 5.28: Minitab's contour plot of displacement versus length, width.

### 5.3.5.3 Response surface regression: Mass versus length, width

Once displacement have been considered, regression equation for mass is now obtained:

$$M = 0.85678 + 0.000135L - 0.001496W + 0.000015L * W \quad (5.2)$$

where  $M$  is mass. Figure 5.29 depicts the contour plot for this equation. As it can be supposed, the lowest mass is obtained using the shortest length and width. The last step is to examine failure values.

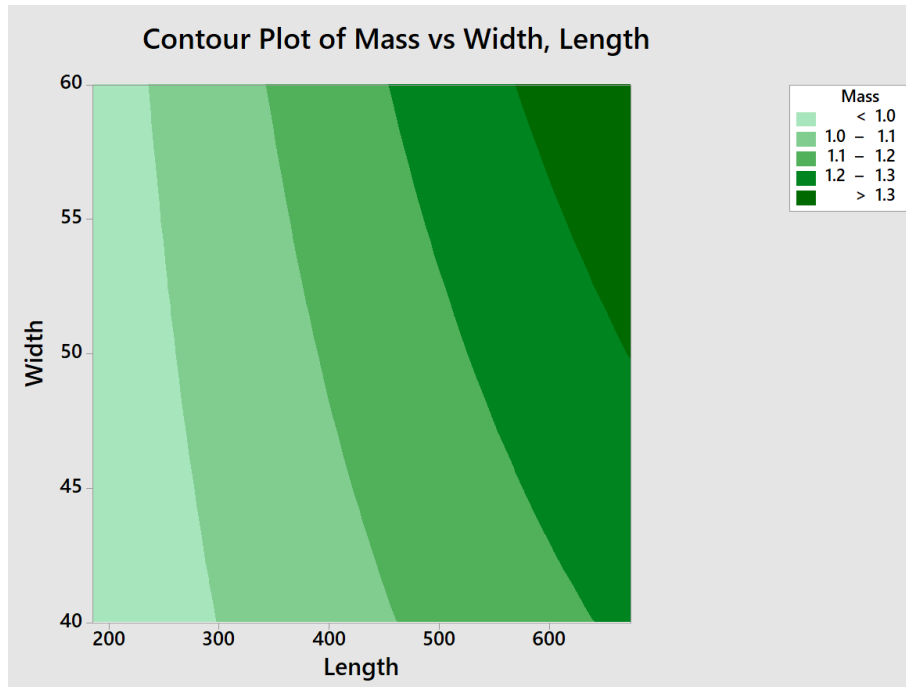


Figure 5.29: Minitab's contour plot of mass versus length, width.

#### 5.3.5.4 Response surface regression: Failure versus length, width

Response surface regression output for composite failure can be evaluated using Equation 5.3.

$$F = 2.1801 - 0.005185L - 0.000845W + 0.000005L^2 - 0.000002L * W \quad (5.3)$$

Figure 5.30 illustrate the contour plot for failure versus length, width. Here it can be concluded that not always adding more material results in less failure value. Taking for example a length of 650 mm and 60 mm width, the failure value will be among 0.7 and 0.8. But if 550 mm length and 60 mm width is now chosen, failure value will be below 0.7.



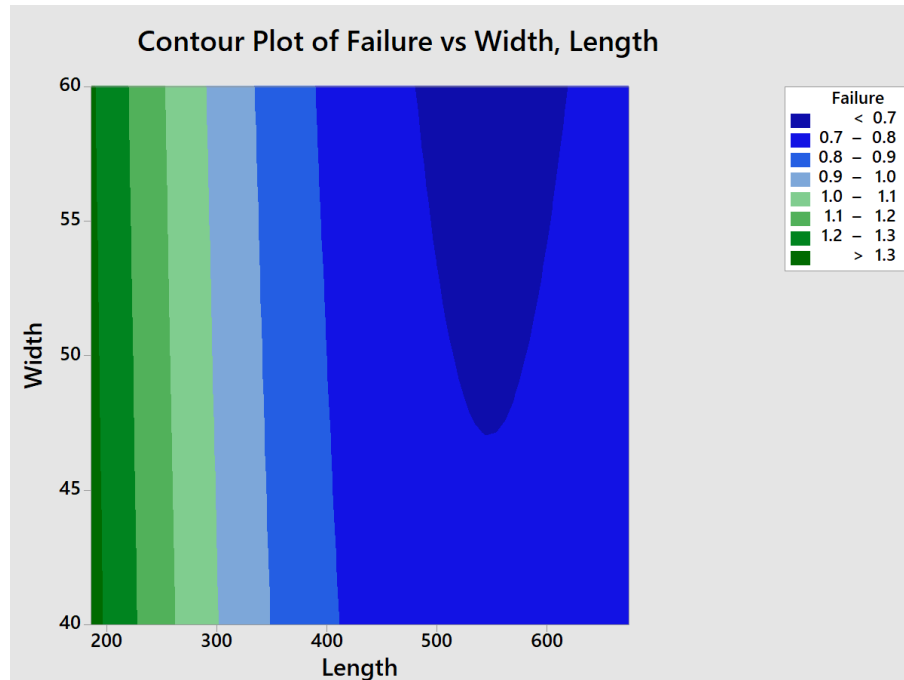


Figure 5.30: Minitab's contour plot of failure versus length, width.

### 5.3.5.5 Response optimizer

Once all three response surfaces were obtained, a response optimizer can be run. Minitab let the user to choose which variables is willing to optimize. In Table 5.10 response optimizer inputs are listed. Since all values for displacement in Table 5.9 are below 10 % of the blade's length, the option of "Do not optimized" is chosen. Thus, the program will just focused on minimize mass and failure value.

Table 5.10: Response optimizer inputs.

Response	Goal
Mass	Minimize
Displacement	Do not optimize
Failure	Minimize

Optimizer results are shown in Table 5.11. Minitab's optimizer algorithm expects a 95% accuracy for maximum failure value and mass using spar caps with 432.24 mm length and 40 mm width. Thus, a model using these dimensions will be simulated to verify the results.

Table 5.11: Optimizer results with 95 % accuracy expected.

	Element	Value
Inputs	Spar cap length	432.24 mm
	Spar cap width	40 mm
Outputs	Max. failure index	0.7746
	Mass	1.0826 kg

## 5.4 Blade model “version 3.1”

Optimization results were gotten from software Minitab and are listed on Table 5.11. The blade’s named selections are modified and the spar cap is set to 432 mm length and 40 mm width as is suggested (Figure 5.31). Other named selections and composite lay-ups stay the same as “version 3.0” in Section 5.3.

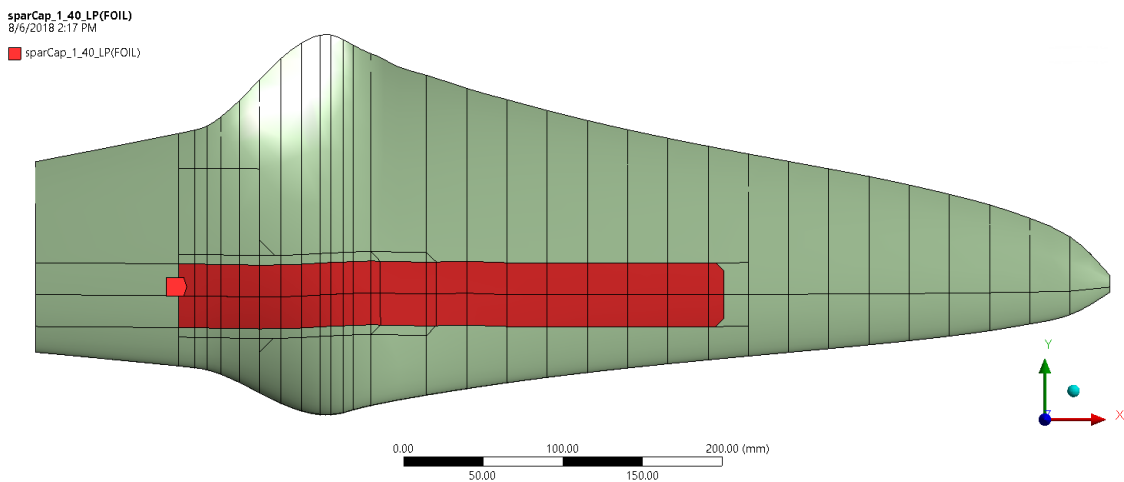


Figure 5.31: Spar cap with 432 mm length and 40 mm width for blade “version 3.1”.

### 5.4.1 Static Structural simulation

Just as previous sections, boundary conditions remained the same as Section 4.2.4. Results are shown in Table 5.12. It has to be noted that 25.445 mm is the largest tip displacement so far (Figure 5.32). This could be attributed to the fact that spar caps do not extend until the tip, making it more flexible. Yet, this value is less than 10 % of the blade’s length.

Figures 5.33 (a) and (b) depict the stress distribution on both pressure and suction side of the blade. Maximum tensile stress has been reduced around 4.29 % compared with the value on Table 5.5 and compressive stress approximately 14.98 %.

In the same way, the highest strain value has lowered about 14.23 % compared with its previous “version 3.0”. The strain distribution can be observed in Figures 5.34 (a) and (b).

Table 5.12: Static Structural simulation results for blade “version 3.1”.

Results	Value	Units/Criteria
Tip displacement	25.445	mm
Max. Stress (Tensile)	28.548	MPa
Max. Stress (Compressive)	35.13	MPa
Max: Strain	0.0028606	mm/mm
Mass	1.0836	kg
Max. Failure index	0.80036	Max. Strain

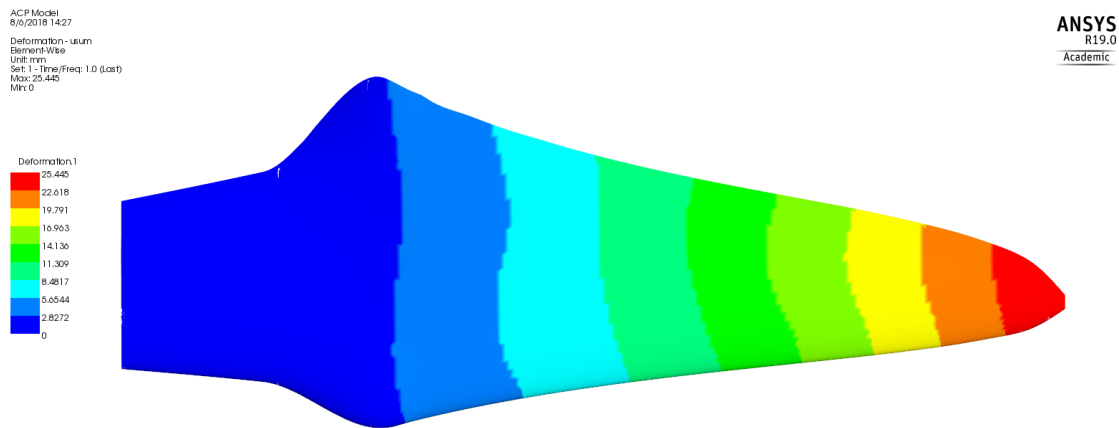


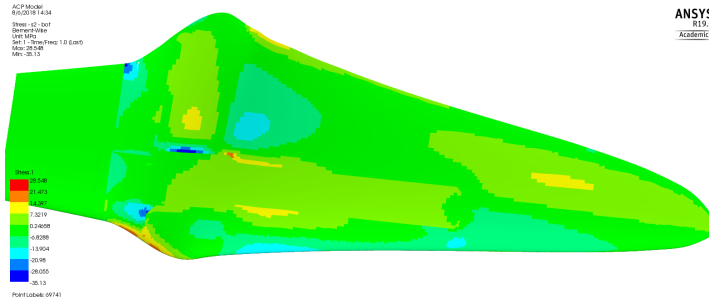
Figure 5.32: Displacement simulation results for blade “version 3.1”.

The highest strain values are located on the suction side of the blade due to its irregular geometry. Furthermore, Maximum Strain criteria is presented in Figures 5.35 (a) and (b) and its distribution looks very much alike as the ones in Figure 5.34.

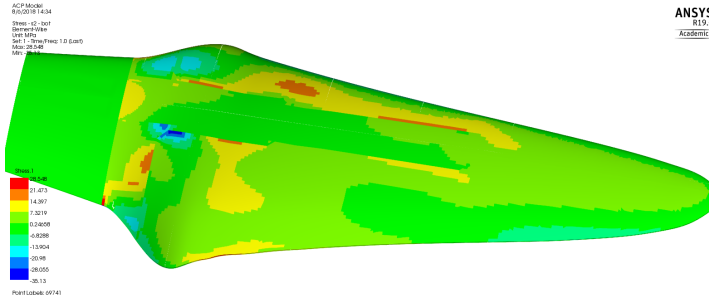
Table 5.13 presents a comparison between the input values and results that Minitab suggested versus the ones set in ANSYS as well as simulation results. First of all, spar cap lengths were changed to an even number because 0.22 mm is a very small portion of material and can be neglected and also, when fabricated, this length can be difficult to handle.

Mass results are very similar, their tiny variation might be connected to spar caps length change. On the other hand, failure deviation is the greatest, however, it is within the precision range Minitab estimated. An explanation can be that Minitab’s regression equation did not fit well with the nonlinearity of composite materials and the asymmetrical geometry of the blade.

As this model has surpassed static structural simulation requirements, it will be subjected to further analysis.

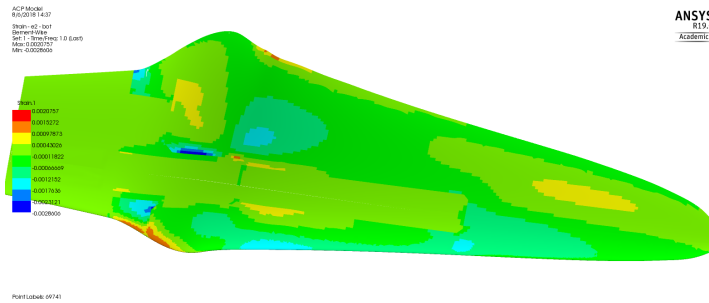


(a) Stresses on pressure side.

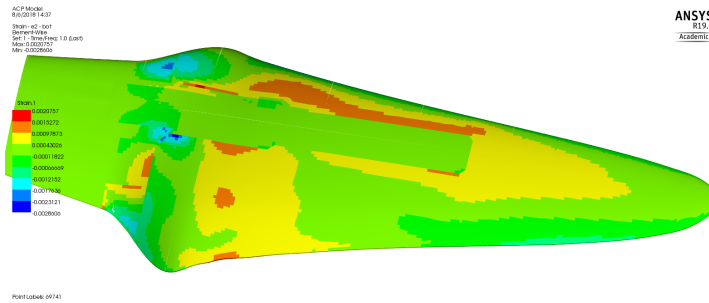


(b) Stresses on suction side.

Figure 5.33: Stress distribution results in the 2 direction in both sides of the blade “version 3.1”.

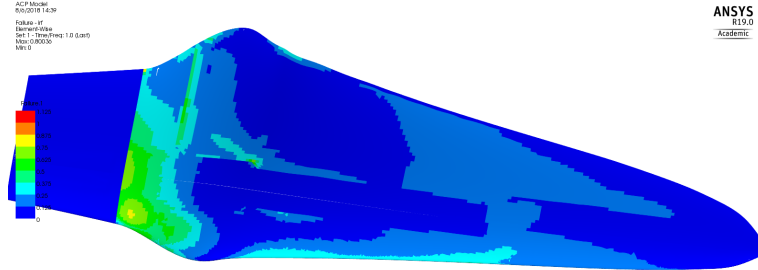


(a) Strains on pressure side.

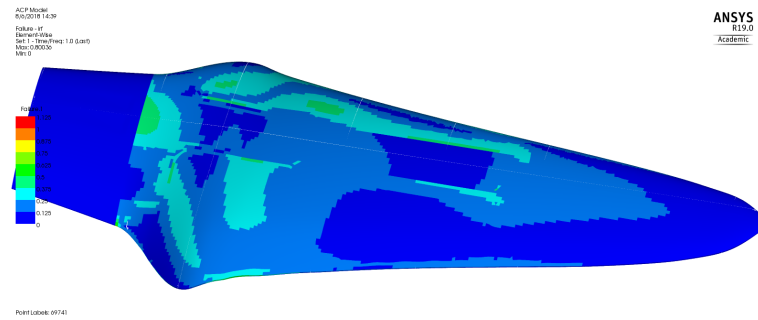


(b) Strains on suction side.

Figure 5.34: Strain distribution results in the 2 direction in both sides of the blade “version 3.1”.



(a) Maximum Strain Criteria distribution on pressure side.



(b) Maximum Strain Criteria distribution on suction side.

Figure 5.35: Maximum Strain Criteria value distribution on pressure side of the blade “version 3.1”.

Table 5.13: Comparison between response optimizer and Static Structural simulation results.

	Element	Minitab’s results	Simulation results	Variation (%)
Inputs	Spar cap length	432.24 mm	432 mm	-0.055
	Spar cap width	40 mm	40 mm	0
Outputs	Max. failure index	0.7746	0.80036	+3.21
	Mass	1.0826 kg	1.0836 kg	+0.09

### 5.4.2 Eigenvalue buckling simulation

For this analysis, same conditions as Section 5.3.3 are taken. Table 5.14 shows the buckling simulation results. Just as “version 3.0”, the lowest load multiplier is the third mode. Even though all other load multipliers has increased around 1.5 % compared with results in Table 5.6, mode 3 has lowered almost the same amount. This is because as illustrated in Figure 5.36, buckling is presented in the blade’s tip zone, where neither there is any reinforcement for the hydrofoil nor spar caps reach that region.

Despite all commented before, the lowest load multiplier is greater than 2 and therefore the next simulation can be evaluated.

Table 5.14: Eigenvalue buckling simulation results for blade “version 3.1”.

Mode	Load multiplier	Total displacement (mm)
1	-3.4636	1.1306
2	-2.7173	1.0545
3	-2.1779	1.0728
4	3.2713	1.0237
5	3.4224	1.0233

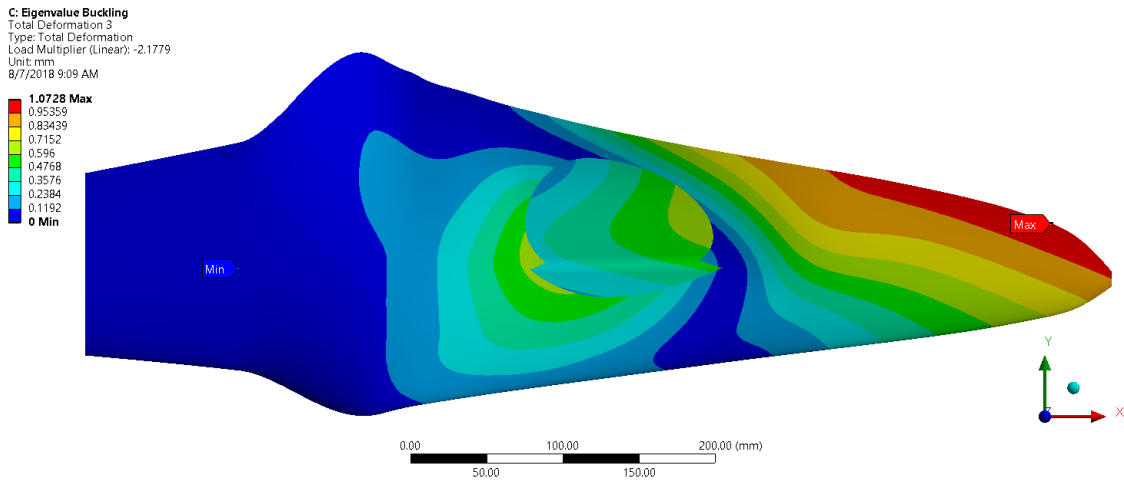


Figure 5.36: Eigenvalue buckling analysis results for mode 3 of blade “version 3.1”.

### 5.4.3 Modal analysis simulation

In Table 5.15 the first five modal modes of blade “version 3.1” can be observed. Compared with results in Table 5.7, the first mode has risen 16.71 % leading to a total tip displacement of 99.38 mm as can be seen in Figure 5.37. Still, all these modes far beyond blade’s working conditions.

Table 5.15: Modal simulation results for blade “version 3.1”.

Mode	Frequency (Hz)	Total displacement (mm)
1	64.097	99.38
2	149.53	787.75
3	168.06	150.6
4	217.25	1073.2
5	240.7	121.56

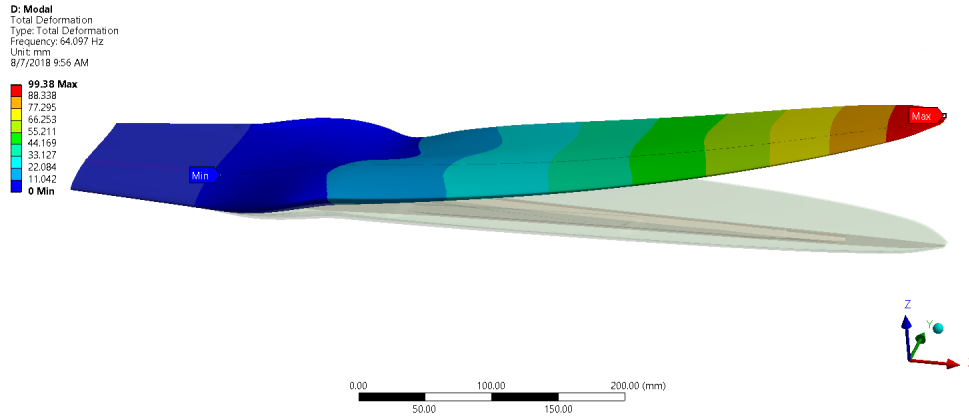


Figure 5.37: First mode of blade “version 3.1” with a frequency of 64.097 Hz.

## 5.5 Comparison of blade models

In this section, the structural characteristics of each blade version are compared on Tables 5.16 and 5.17. The first version of the blade is completely made of GF (Section 1.1) and the goal of this work is to improve the structural behavior of this blade.

Four versions were made as a result of an iterative design process described on Section 1.5 and Figure 1.6. Blade versions 2.0 and 2.1 were rejected because the first one did not fulfill safety factors and also this version was intended as starting point for the design process. Meanwhile, “version 2.1” did not present fiber failure, however, material thickness inside the blade was not considered making this version physically impossible to fabricate.

Blade version 3.0 used hybrid material reinforcements additional to spar caps and as a result, this version fulfilled structural requirements. Tip displacement increased compared with previous versions but maximum failure index was already below 0.9. Furthermore, this version accomplished both eigenvalue buckling and modal analysis. After having a successful composite configuration, spar caps were subjected to an optimization process since these elements have a great influence in the structural behavior as well as in the mass.

The program Minitab suggested the used of spar caps with 432 mm length and 40 mm width and ANSYS simulation results were satisfactory. Although tip displacement is the highest of all versions, maximum failure index is the lowest and also, mass was able to be reduced 25.27 % compared with version 1. Once the results of eigenvalue buckling and modal analysis were carry out, it was concluded that blade “version 3.1” (see Figure 5.38) has an acceptable composite lay-up configuration and can be taken to the next stage of fabrication process.

Table 5.16: Structural behavior comparison between different blade versions, part 1 of 2.

Blade version	Tip displacement (mm)	Max. stress (MPa)	Max. strain (mm/mm)
1.0	21.469	44.555	0.0036073
2.0	24.981	60.251	0.0046189
2.1	18.761	32.921	0.0023419
3.0	25.295	41.323	0.0033354
3.1	25.445	35.130	0.0028606

Table 5.17: Structural behavior comparison between different blade versions, part 2 of 2

Blade version	Max. failure index	Mass (kg)	Buckling factor	Freq. mode 1 (Hz)
1.0	0.97	1.45	–	–
2.0	1.588	0.8759	–	–
2.1	0.8792	1.0747	–	–
3.0	0.8729	1.1193	2.2192	53.384
3.1	0.8003	1.0836	2.1779	64.097

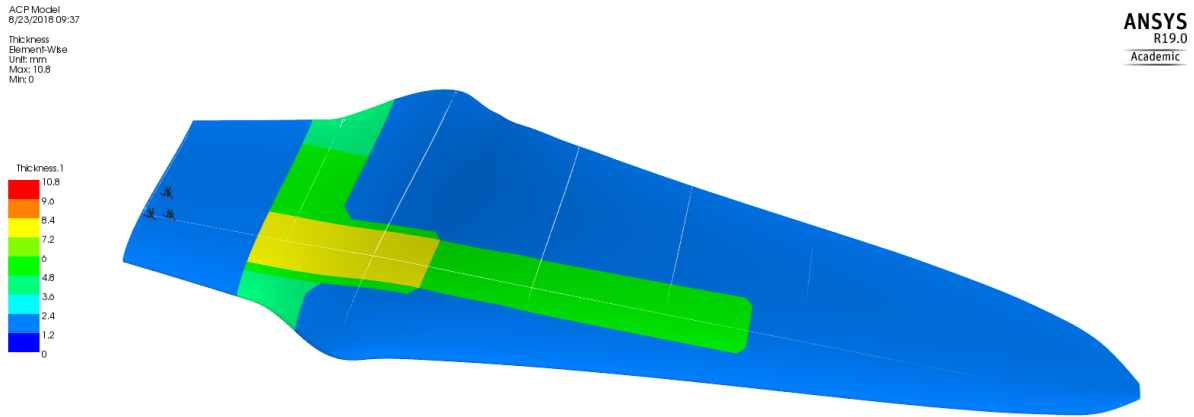


Figure 5.38: Blade “version 3.1” composite lay-up setup.



## Chapter 6

# Conclusions and further work

Composite materials have taken over applications where conventional materials do not suit well. Wind turbine blades are a great example, because the application calls for great mechanical resistance but at the same time, the lowest possible weight. This strength-to-weight ratio comes with the disadvantage of nonlinear relationships, which makes almost impossible handmade calculations. Because of that, the use of softwares such as ANSYS ACP is fundamental.

Moreover, due to the infinite ply combinations that can be made when using composites materials, limitless solutions can be obtained. Thus, the solution for the hydrokinetic turbine blade found in this work is not unique. Nevertheless, the combination of GF and hybrid material is satisfactory for this application.

Furthermore, it was demonstrated that when the optimization method was used, not only was the mass reduced, but also failure criterion values lowered as well as stresses and strains along the blade. Despite these achievements, very important limiting factors were detected. Both the geometry and internal space of the hydrodynamic foils are complicated. The irregular geometry of the blade facilitates stress concentrations and shear loads and, therefore, more reinforcements should be implemented besides spar caps and shear webs, however, there is few space for doing this.

As a final comment, in this work, the maximum fiber failure index reached was 0.8, meanwhile, in other works, for example, Grogan, D. [11] the highest permitted is 0.4. Therefore, in opinion of the author, a redesign of the hydrodynamic profiles and blade geometry may be needed as further work in order to reduced as much as possible failure indexes.



# Bibliography

- [1] Martin O. L. Hansen. *Aerodynamics of wind turbines*. Earthscan, London, second edition, 2008.
- [2] Manfred Stiebler. *Wind Energy Systems for Electric Power Generation*. Springer, Berlin, 2008.
- [3] Union of concern scientist. How hydrokinetic energy works. <https://www.ucsusa.org/clean-energy/renewable-energy/how-hydrokinetic-energy-works>{#}. W0Nm1J{ }0mUk, 2008.
- [4] CEMIE-Océano. Energy from current and tidals. <http://cemieoceano.mx/energia-corrientes-mareomotriz.html>, 2017.
- [5] Saul Ledesma. Diseño de un prototipo de hélice de hasta 70 cm de longitud de material compuesto. Research note, Centro de ingeniería desarrollo industria, CIDESI, 2017.
- [6] Jaime Espinoza Hernández. Diseño de un prototipo de hélice de hasta 70 cm de longitud de material compuesto. Report note, Centro de Ingeniería y Desarrollo Industrial, CIDESI, 2017.
- [7] Moulds Patterns and Models Limited. MPM. <https://www.mpbradford.co.uk/blog/article/grp-vs-carbon-fbre>, 2018.
- [8] Compositd World. CW. <https://www.compositesworld.com/articles/wind-turbine-blades-glass-vs-carbon-fiber>, 2012.
- [9] Alfredo Siu Calderón. Comportamiento a la fatiga de elementos de aspas de turbina eólica manufacturados con materiales compuestos híbridos. Master thesis, Centro de ingeniería desarrollo industria, CIDESI, 2017.
- [10] Ole Thybo Thomsen. Sandwich materials for wind turbine blades - Present and future. *Journal of Sandwich Structures and Materials*, 11(1):7–26, 2009.
- [11] D. M. Grogan, S. B. Leen, C. R. Kennedy, and C. M. Ó Brádaigh. Design of composite tidal turbine blades. *Renewable Energy*, 57:151–162, 2013.

- [12] Jin Chen, Quan Wang, Wen Zhong Shen, Xiaoping Pang, Songlin Li, and Xiaofeng Guo. Structural optimization study of composite wind turbine blade. *Materials and Design*, 46:247–255, 2013.
- [13] Jinshui Yang, Chaoyi Peng, Jiayu Xiao, Jingcheng Zeng, Suli Xing, Jiaotong Jin, and Hang Deng. Structural investigation of composite wind turbine blade considering structural collapse in full-scale static tests. *Composite Structures*, 97:15–29, 2013.
- [14] Ronald F Gibson. *Principles of Composite Material Mechanics*. Taylor and Francis Group, Ohio, 2012.
- [15] Peter J. Schubel and Richard J. Crossley. Wind turbine blade design. *Energies*, 5(9):3425–3449, 2012.
- [16] ANSYS Inc. ANSYS Composite PrepPost. <https://www.ansys.com/products/structures/ansys-composite-preppost>, 2008.
- [17] ANSYS Inc. ANSYS Help. <https://ansyshelp.ansys.com/>, 2018.
- [18] Minitab Inc. Minitab support. <https://support.minitab.com/en-us/minitab/18/help-and-how-to/modeling-statistics/using-fitted-models/how-to/response-optimizer/>, 2017.

---

# Appendices



# Appendix A

## Hybrid material properties

In this appendix, the defined material properties used in ANSYS Workbench of the hybrid composite material are listed on Tables A.1, A.2 and A.3. The properties are named after the ones registered in Engineering Data. It should be kept in mind that some of these values were gotten from assumption made on Section 4.1.

Table A.1: Hybrid composite material density and orthotropic elasticity properties.

Property	Value	Unit
Density	2453	$kg/m^3$
Orthotropic Elasticity		
Young's Modulus X direction	56.13E+9	Pa
Young's Modulus Y direction	12.78E+9	Pa
Young's Modulus Z direction	12.78E+9	Pa
Poisson's Ratio XY	0.295	
Poisson's Ratio YZ	0.295	
Poisson's Ratio ZX	0.295	
Shear Modulus XY	4.57E+9	Pa
Shear Modulus YZ	4.57E+9	Pa
Shear Modulus YZ	4.57E+9	Pa

Table A.2: Hybrid composite material orthotropic stress limits properties.

Property	Value	Unit
Tensile X direction	1.0761E+9	Pa
Tensile Y direction	46.86E+6	Pa
Tensile Z direction	46.86E+6	Pa
Compressive X direction	-418.7E+6	Pa
Compressive Y direction	-111.53E+6	Pa
Compressive Z direction	-111.53E+6	Pa
Shear XY	68.56E+6	Pa
Shear YZ	68.56E+6	Pa
Shear YZ	68.56E+6	Pa

Table A.3: Hybrid composite material orthotropic strain limits properties.

Property	Value
Tensile X direction	0.0192
Tensile Y direction	0.00366
Tensile Z direction	0.00366
Compressive X direction	-0.00873
Compressive Y direction	-0.00873
Compressive Z direction	-0.00873
Shear XY	0.015
Shear YZ	0.015
Shear YZ	0.015



# Appendix B

## Chronogram of activities

Figure B.1 depicts the chronogram of activities followed for this work.

# APPENDIX B. CHRONOGRAM OF ACTIVITIES

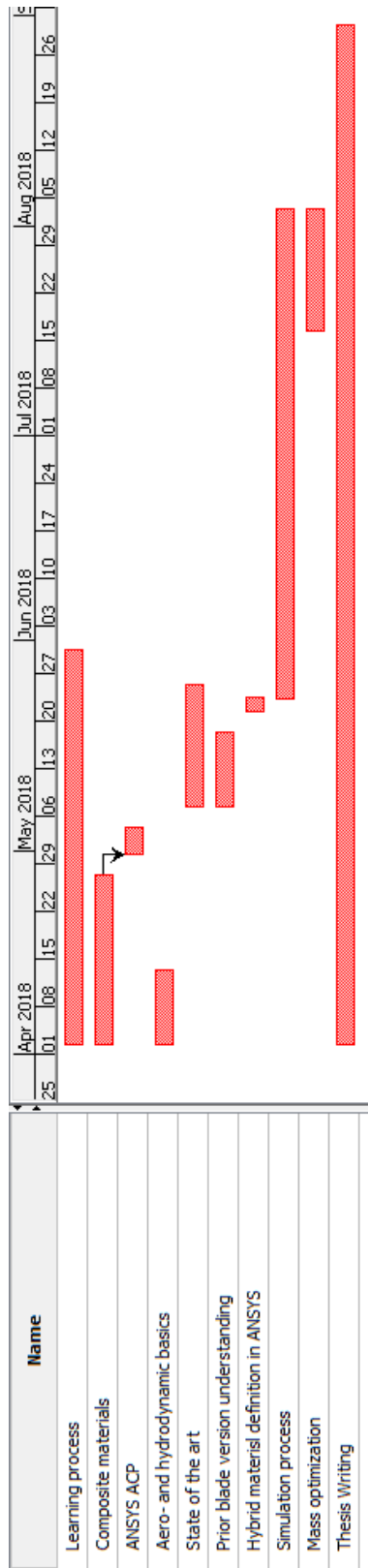


Figure B.1: Chronogram of activities.

# Appendix C

## Computational fluid dynamics forces

Table C.1 lists the forces that are interacting with the hydrokinetic turbine blade obtained from a CFD simulation [6]. The element number refers to the perpendicular sections which the blade is divided into. The distance from hub indicates the distance at which every element is located from the hub axis and not from the root of the blade as it has been handled along this work.

Table C.1: Forces interacting with the hydrokinetic turbine blade.

Element	Distance from hub (m)	Axial force (N)	Tangential force (N)
1	0.162540457	22.0994491	4.029845455
2	0.171394115	30.31558993	6.240974909
3	0.182767787	37.6009091	9.259504022
4	0.195740045	42.60674038	12.77128772
5	0.209259955	43.6809869	15.61248214
6	0.222232213	39.92761235	16.32810802
7	0.233605885	23.93219358	10.61681835
8	0.240306122	27.76034457	12.94739249
9	0.248075916	22.6919228	10.9817511
10	0.254477598	38.25714201	18.92279176
11	0.265410472	119.6500434	56.33679947
12	0.300449473	83.49403171	35.26831016
13	0.325674211	81.06170899	31.2597805
14	0.350898948	78.42068718	27.75383669
15	0.376123685	75.58227152	24.65727615
16	0.401348421	72.69345605	21.94473938
17	0.426573158	69.78643999	19.56066229
18	0.451797895	66.87061534	17.45488861
19	0.477022632	63.93616699	15.58264059
20	0.502247369	60.95540397	13.90389492
21	0.527472105	57.88189396	12.38243083
22	0.552696842	54.64703554	10.98463428
23	0.577921579	51.08257855	9.665080979
24	0.603146316	47.0573744	8.393308264
25	0.628371053	42.44268918	7.146920612
26	0.65359579	36.78619066	5.857277013
27	0.678820526	29.19052178	4.404022316
28	0.704045263	14.86626277	2.152862665